Infrasound cooling of a steel plate

by Emrik Strandh

LUND
UNIVERSITY

Thesis for the degree of Master of Science
Thesis advisors: Lei Wang, LTH, Anders Carlestam, SSAB

To be presented, with the permission of the Faculty of Engineering of Lund University, for public criticism on the online meeting at the Department of Energy Sciences on Monday, the 10th of June 2024 at 12:00.

This degree project for the degree of Master of Science in Engineering has been conducted at the Division of Thermal Power Engineering, Department of Energy Sciences, Faculty of Engineering, Lund University.

Supervisor at the Division of Thermal Power Engineering was Docent Lei Wang. Supervisor at SSAB was Anders Carlestam.

Examiner at Lund University was Professor Christer Fureby.

The project was carried out in cooperation with SSAB Oxelösund and Infrasonik AB.

Department of Energy Sciences
Faculty of Engineering
Lund University

ISSN: <0282-1990>
LUTMDN/TMHP-24/5599-SE

Typeset in LaTeX
Lund 2024

Sammanfattning

Inom stålindustrin är naturlig konvektion en konventionell kylningsmetod. Genom att öka kylhastigheten jämfört med naturlig konvektion kan produktiviteten öka då kylbäddarna kan kortas och stålplåtarna tillbringar mindre tid under kylning. Detta frigör plats och sparar tid. Då möjligheten att använda infraljud till kylning redan har bekräftats genom experiment, ska denna masteruppsats försöka besvara ifall det finns en optimal frekvens och ett optimalt ljudtryck för att maximera värmeövergångstalet. För att besvara denna fråga utfördes experiment där en stålplåt med måtten $120 \times 120 \times 6\ mm$ upphettades till $600\ °C$ för att sedan kylas i en infraljudskylkammare. Kylkammaren var kopplad med resonanstuber till en pulsator som genererar infraljud. Genom att variera resonanstub-slängderna och slaglängden på pistongerna som genererar infraljudet kunde olika fall med varierande ljudtryck och frekvens testas. Plåtens temperatur loggades varje sekund och genom användning av klumpkroppsanalys kunde värmeövergångstalet beräknas. En ickelinjär yta anpassades till datan med hänseende till partikelhastighetsamplituden och frekvensen. För att maximera värmeövergångstalet bör partikelhastighetsamplituden vara så hög som möjligt medan frekvensen bör vara så låg som möjligt. Dock upptäcktes det även att partikelhastighetsamplituden var starkt beroende av både frekvensen och slaglängden.

Abstract

In the steel industry, a conventional cooling method is natural convection. By increasing the cooling rate compared to natural convection, the productivity can be increased as cooling beds can be shortened, and the steel plates spend less time in cooling. This frees up space and saves time. As the ability to use infrasound for cooling had already been verified through experiments, this master thesis set out to answer if there exists an optimal frequency and an optimal sound pressure to maximize the heat transfer coefficient. To answer this question, experiments were conducted where a $120 \times 120 \times 6$ mm steel plate was heated to 600 $^{\circ}C$ and then cooled in an infrasound cooling chamber. The cooling chamber was connected by resonance tubes to the infrasound generating pulsator. By varying the resonance tube length and the stroke length of the pistons generating the infrasound, different cases with varying frequency and sound pressure were tested. The plate temperature was logged each second and by using lumped body analysis, the heat transfer coefficient could be calculated. A non-linear surface was fitted to the data with respect to the calculated particle velocity amplitude and the frequency. To maximize the heat transfer coefficient, the particle velocity amplitude should be as high as possible while the frequency should be as low as possible. However, it was also found the particle velocity amplitude depends heavily on frequency and stroke length.

Acknowledgment

First and foremost, I would like to thank my supervisor at LTH, Lei Wang. Not only have you been a constant and unfaltering support in the lab and through discussions, but also a great friend and teacher. Without your support this master thesis would not have been possible. I direct big gratitude towards Professor Christer Fureby for introducing me to this master thesis and for your relevant new perspectives on the topic through our discussions.

I am very grateful for Anders Carlestam at SSAB and Mats Olsson at Infrasonik AB for believing in me an allowing me to write this thesis. Your ideas throughout the project have been a source of guidance and inspiration to me. Thank you.

I would like to thank all employees at Infrasonik AB for your kindness and openness towards me. I give thanks to Johan Åhling especially for the very thorough guidance of the operation of the pulsator and the many support calls.

Without some help from people at other departments I could not have completed the experiments. Thank you Anders Olsson at the Energy Sciences for all the practical help in big and small things. Thank you Getachew Darge of Industrial Electrical Engineering for your expertise in all things electrical. Thank you Wei Qiu of Biomedical Engineering for helping me convert signals to visuals.

A big thank you to my family and friends for all the support and the belief shown. It meant a lot to me.

Contents

List of Figures

List of Tables

Nomenclature

Roman Letters

A	Area	$[m^2]$
b	Time constant	$[1/s]$
Bi	Biot number	[-]
c	Speed of sound	$[m/s]$
c_p	Isobaric specific heat capacity	$[J/(kgK)]$
f	Frequency	$[Hz]$
h	Heat transfer coefficient	$[W/(m^2K)]$
$\langle h \rangle$	Mean heat transfer coefficient across all temperatures	$[W/(m^2K)]$
k	Thermal conductivity	$[W/(mK)]$
L	Plate width	$[m]$
L_c	Characteristic length	$[m]$
L_R	Total length of resonance tubes	$[m]$
$L_{Correction}$	Calculated length of the pulsator and pipes	$[m]$
L_{long}	Length of the long resonance tube	$[m]$
L_{short}	Length of the short resonance tube	$[m]$
m	Mass	$[kg]$
Nu	Nusselt number	[-]
P	Consumed power	[kW]

p	Sound pressure	[Pa]
$\hat{p}$	Sound pressure amplitude	[Pa]
Pr	Prandtl number	[-]
Q	Heat transfer	$[J]$
$\dot{Q}$	Heat transfer rate	$[W]$
$\dot{q}$	Heat flux	$[W/m^2]$
R_I	Acoustic intensity reflection coefficient	[-]
R_Π	Acoustic power reflection coefficient	[-]
r	Radius of pipe	$[m]$
Re	Reynolds number	[-]
S	Cross sectional area	$[m^2]$
SE	Standard error	$[Unit\ as\ investigated\ property]$
SL	Stroke length	$[mm]$
T_I	Acoustic intensity transmission coefficient	[-]
T_Π	Acoustic power transmission coefficient	[-]
T	Temperature	$[°C\ or\ K]$
t	Elapsed time	$[s]$
U	Volume velocity	$[m^3/s]$
u	Particle velocity	$[m/s]$
$\hat{u}$	Particle velocity amplitude	$[m/s]$
$\langle u \rangle$	Mean velocity	$[m/s]$
V	Volume	$[m^3/s]$
$\hat{V}$	Voltage amplitude	$[V]$

V_{pk-pk}	Peak to peak voltage	$[V]$
Z	Acoustic impedance	$[Pa \cdot s/m^3]$
z	Specific acoustic impedance	$[Pa \cdot s/m]$

Greek Letters

α	Thermal diffusivity	$[m^2/s]$
ε	Emissivity of radiation	[-]
λ	Wavelength	$[m]$
μ	Mean value	$[Unit\ as\ investigated\ property]$
η_{th}	Thermal efficiency	[-]
ν	Kinematic viscosity	$[m^2/s]$
ω	Angular frequency	$[rad/s]$
ρ	Density	$[kg/m^3]$
σ	Stefan-Boltzmann constant	$[W/(m^2K^4)]$
Θ	Temperature difference	$[°C\ or\ K]$

Subscripts

a	Air
B	Blackbody
b	Bulk
ch	Cooling chamber
$Conv$	Convective
$Conv, C$	Convective corrected
$Conv, 300$	Convective at 350 - 300 $°C$
end	At end of interval

i	Initial
Rad	Radiative
s	Steel plate
Tot	Total
w	Water

Chapter 1.

Introduction

The ability to efficiently cool materials is important. There are constant efforts to improve the heat transfer rate in different applications through innovation and research. A novel technique involves infrasound to increase the heat transfer from a steel plate. There are many different benefits to this. Compared to the time consuming cooling on cooling beds commonly used in the steel industry today, the infrasound cooling technology offers a more time efficient cooling. Thus the production speed could be increased as well as the cooling beds shortened. This could lead to a potential increase of production speed and volume. In steel production, different heat treatments are important to achieve different material properties of the steel. With infrasound cooling, the heat transfer rate can be accurately controlled. By extension, the material properties of the steel as well. Lastly, infrasound cooling offers a uniform cooling across the whole width of the plate. A benefit compared to forced convection from a fan blowing in one direction across the plate.

To harness the full potential of the infrasound cooling technology, research on the behavior and characteristics of the technique is needed. This study is purely experimental. However, it could be seen as a stepping stone towards more generalizable results and predictions in the field of infrasound cooling.

1.1. Previous studies

Although being a relatively unexplored field of research, some papers on the subject of infrasound cooling exists. Previously, a study on the enhancement of heat transfer using infrasound was made by Woods [10]. In the paper, a setup with an air compressor and two 4.7 m resonance tubes with the diameter of 76 mm each was used. The resonance tubes were quarter wavelength resonators and corresponded to a frequency of 18 Hz. Cooling was performed of a wooden sensor-clad wooden dowel with the diameter of 32 mm. A steady air flow from a blower was directed at the dowel perpendicular to the infrasound cooling system. By varying the sound pressure, the particle velocity of the infrasound could be altered.

From the experiments conducted, Woods drew several conclusions. The most important conclusions in the perspective of this thesis are: Infrasound increases the heat transfer from a cylinder significantly. By combining infrasound cooling and forced convection, the required power could be decreased between 12 and 75 %. The use of infrasound cooling made the cooling more uniform.

A study done by Preston and Johnson [8] used two speakers in a speaker box connected to a heat transfer channel, with variable width, ending in a Helmholtz resonator. In the bottom of the channel, there was an inlet and an outlet for air flowing with constant velocity. The roof of the channel had cooling with copper tubes and plate. The Helmholtz resonator was designed to accommodate a 20 Hz standing wave. However, peak resonance for the system was found at 36.5 or 36.75 Hz (depending on channel width), indicating that first harmonic resonance produced more power compared to the fundamental frequency resonance.

Preston and Johnson concluded infrasound cooling increases the heat transfer over a flat plate. Compared to natural convection, infrasound cooling can increase the heat transfer tenfold. When comparing against forced convection, the highest increase in heat transfer was found at low Re_D ($\leq$ 2300) suggesting the acoustic effect gets overpowered at higher mean flows.

1.2. Purpose/Aim

The aim of this master thesis is to provide new insight and validation of previous results in the relatively unexplored field of infrasound cooling. Primarily, the heat transfer coefficient at different standing wave frequencies and particle velocity amplitudes will be investigated. For comparability, the power required to perform the infrasound cooling at the different frequencies and particle velocity amplitudes will also be measured. This thesis aims to answer the question: is there an optimal frequency and particle velocity amplitude for infrasound cooling?

Chapter 2.

Theory

2.1. Cooling

When steel is processed, an important step is cooling. The cooling serves many purposes, although the primary purpose is to affect the properties of the steel. By manipulating the cooling rate, many different phases of steel can be achieved. At 900 $°C$ most iron based alloys are purely austenitic and by applying different cooling rates, the microstructures of steel; martensite, bainite, pearlite, and ferrite (as well as residual austenite) can be formed. For the hardest microstructure, martensite, to form, a fast cooling is required as this traps the coal atoms in the iron matrix. The dissolved coal acts as a hardener as it prevents the planar slip of the atom layers. Martensite typically requires some form of quenching and thus contains high residual stresses making it prone to surface cracking and other defects [4].

One solution to this problem could be a lower cooling rate. However, natural convection is not rapid enough to produce the martensite.

2.1.1. Conduction

The most simple mode of heat transfer is known as conduction. Conduction is the diffusion of heat, occurring through solids and stationary fluids. Fouriers law of conduction [9] gives the heat flux through a solid or stationary fluid as

$$\dot{q} = -k\nabla T \tag{2.1}$$

where $\dot{q}$ is the conductive power per unit area with unit W/m^2, k is the thermal conductivity with unit $W/(mK)$ and ∇T is the temperature gradient with unit K/m.

2.1.2. Convection

Convection involves fluid motion and it increases the heat transfer compared to conduction. There are different types of convection. They are distinguished by the different ways the fluid is set in motion. If a hot flat plate in cool still air is considered, then the convection will be natural. This is because the fluid motion originates from heated air rising and new cool air will take its place, thus the convection occurs naturally . On the other hand, if the fluid motion would originate from a fan blowing across the plate, the convection would be forced. Forced convection has a higher heat transfer rate compared to natural convection and they both have a higher heat transfer rate compared to pure conduction [2].

Despite being a complex phenomenon depending on many different parameters, convective heat transfer was characterized in Newton's law of cooling as

$$\dot{Q} = hA_s(T_s - T_\infty) \tag{2.2}$$

Where $\dot{Q}$ is the convective heat transfer rate with unit W, h is the heat transfer coefficient with unit $W/(m^2K)$, A_s is the heat transfer area with unit m^2, T_s is the temperature of the surface with unit K and T_∞ is the temperature of the fluid far away from the heat transfer region with unit K.

However, the determination of h is not trivial. Some relations based on empirical studies exist. The relations often involve the Nusselt number, the Reynolds number and the Prandtl number representing the non-dimensionalized heat transfer coefficient, the non-dimensionalized flow parameter and the ratio between the velocity boundary layer thickness and the thermal boundary layer thickness, defined as

$$Nu = \frac{hL_c}{\lambda} \tag{2.3}$$

$$Re = \frac{uL_c}{\nu} \tag{2.4}$$

$$Pr = \frac{\nu}{\alpha} \tag{2.5}$$

Where L_c is the characteristic length with unit m, for a flat plate L_c is equal to the thickness of the plate divided by two, λ is the thermal conductivity with unit $W/(mK)$, u is the mean velocity of the flow with unit m/s, ν is the viscosity of the fluid with unit m^2/s and α is the diffusivity of heat with unit m^2/s.

Convective heat transfer can generally be described as [9]

$$Nu = CRe_L^m Pr^n \tag{2.6}$$

where C is an empirically determined coefficient and m and n are empiracally determined exponents.

2.1.3. Radiation

Another mode of heat transfer is radiation. Radiative heat transfer is the emission of electromagnetic radiation from a surface caused by the temperature of said surface. For a blackbody surface, the distribution of emission of radiation is equal across the whole emitting spectrum. The amount of emissive power is also at the maximum level for all wavelengths. Needless to say, most surfaces are not blackbody surfaces. Instead they are more commonly grey bodies, having an emissivity of less than one. For a blackbody surface, emitted radiative power can be written as [9]

$$\dot{Q}_B = A_s \sigma T_s^4 \tag{2.7}$$

where A_s is the surface area with unit m^2, $\sigma = 5.67 \cdot 10^{-8}\ W/(m^2K^4)$ is the Stefan Boltzmann constant and T_s is the absolute temperature with unit K. For a grey surface, the emitted radiative power is written as [9]

$$\dot{Q} = A_s \varepsilon \sigma T_s^4 \tag{2.8}$$

where ε is a unit-less coefficient called emissivity. Emissivity must be less than one for grey bodies.

2.1.4. Biot number

Biot number is a measure to describe the ratio between convective cooling at the surface of a solid and conduction within the solid. If the Biot number is very low ($Bi < 0.1$), the temperature distribution of the solid can be seen as uniform and the lumped body assumption can be used. The Biot number Bi is calculated as [2]

$$Bi = \frac{hL_c}{k} \tag{2.9}$$

where h is the heat transfer coefficient with unit $W/(m^2K)$, L_c is the characteristic length with unit m and k is the conductivity of the solid with unit $W/(mK)$.

2.2. Acoustics

The science of sound waves and their propagation is called acoustics. When a sound wave propagates through some medium it causes the air to oscillate. If the frequency is low enough, the displacement can become several meters.

This section features a short introduction to the acoustics involved in the thesis.

2.2.1. What is Sound?

Sound is a disturbance propagating through an elastic material causing pressure differences (or variations in density depending on the perspective of the reader) audible to a person or detectable by an instrument. The disturbance can be the result of a surface vibrating in contact with air or any elastic material such as water. The pressure differences are displacing particles in the medium it propagates through. The easiest way to demonstrate the phenomenon is to look at a horizontal wall oscillating sinusoidally in air. The forward motion of the wall will give rise to a front of increased pressure as the particles are compressed and the particles will gain momentum in the forward direction. The particles now having a forward motion and momentum will collide with the nearest particles and transfer the momentum to them and so on. This is how the wave front propagates. When the wall then reverses its direction, the particles adjacent to it experience a pressure loss and acceleration in the backwards direction. These motions will result in a longitudinal wave and depending on the frequency of the oscillating wall and the sound pressure generated, the wave could be heard as sound [1].

Although the frequency of sound is now known, what about wavelength? Wavelength λ is the distance one particle travels per cycle, meaning it can be calculated as wave propagation speed c divided by number of cycles per second, or frequency f. The relation between the three quantities is described as [1]

$$\lambda = \frac{c}{f} \tag{2.10}$$

where λ is the wavelength with unit m, c is the speed of sound with unit m/s and f is the frequency with unit Hz.

In air, the speed of sound c with unit m/s can be determined as [1]

$$c = 331.4\sqrt{\frac{T}{273}} \tag{2.11}$$

Where T is the ambient temperature with unit K.

2.2.2. Sound Pressure

As previously mentioned, the driving force of sound is pressure fluctuations. In acoustics, pressure can mean many different things. The static pressure p_0 is the baseline pressure at the surface of the earth, usually around 1 $bar = 10^5\ Pa$. The instantaneous sound pressure $p(t)$ is the deviation from the static pressure due to a sound wave being present. As the instantaneous sound pressure will have very short peaks, a more appropriate measure is sometimes the effective sound pressure p, defined as the root mean square of the instantaneous sound pressure across some integer of wavelengths [1]. In this study, the most important measure is the the pressure amplitude or peak pressure, denoted $\hat{p}$.

2.2.3. Particle velocity

Like the sound pressure, particle velocity can be measured in instantaneous particle velocity $u(t)$ or effective particle velocity u. The instantaneous particle velocity is in the traditional acoustics the velocity of an imagined particle caused by the sound wave and has the unit m/s. The relation between particle velocity and sound pressure is [3]

$$u = \frac{p}{z} \tag{2.12}$$

where p is the sound pressure with unit Pa and z is the specific acoustic impedance with unit $Pa \cdot s/m$.

2.2.4. Impedance

There are three main acoustic impedances available and they all serve different purposes. Impedance can be seen as how much motion a sound wave creates on the medium. The specific acoustic impedance z is most useful when a sound wave travels transmits from one medium to another and is, for a plane wave, defined as [3]

$$z = \frac{p}{u} = \pm\rho_a c \tag{2.13}$$

where z has the unit of $Pa \cdot s/m$, p is the acoustic pressure with unit Pa, u is the particle velocity with unit m/s, ρ_a is the density of air with unit kg/m^3 and c is the speed of sound with unit m/s.

The acoustic impedance Z uses the volume velocity instead of the particle speed and is most useful when the sound waves propagate in pipes as they are radiated from a vibrating surface. It is defined in the relation [3]

$$Z = \frac{p}{U} \tag{2.14}$$

where Z has the unit $Pa \cdot s/m^3$ and U is the volume velocity with unit m^3/s.

The acoustic impedance is related to the specific acoustic impedance at a surface interface through the relation [3]

$$Z = z/S \tag{2.15}$$

where S is the cross sectional area of the tube or pipe with unit m^2.

2.2.5. Lumped acoustic systems

If the dimensions of the pipe are sufficiently small compared to the wavelength, the pipe can be viewed as lumped acoustic element as only plane waves will propagate through it. For air, the lowest frequency with non-planar wave propagation in a circular rigid wall pipe is described by [3]

$$\omega = 1.84 \frac{c}{r} \Leftrightarrow f = \frac{100}{r} \tag{2.16}$$

where ω is the angular frequency with unit rad/s, c is the speed of sound with unit m/s, r is the radius of the pipe with unit m and f is the frequency with unit Hz.

2.2.6. Intensity and power transmission coefficients

When a sound wave moves between different medias or if, for example, the cross sectional area of the pipe changes, some of the power will be reflected and some will be transmitted. Transmittance and reflection can be characterized by the intensity and power transfer coefficients T_I and T_Π and the intensity and power reflection coefficients R_I and R_Π. The sum of transmission and reflection must always be unity, giving [3]

$$T_I + R_I = 1 \tag{2.17}$$

$$T_\Pi + R_\Pi = 1 \tag{2.18}$$

The power transmission coefficient for a sound wave in a single fluid across a section with changing cross sectional is give by [3]

$$T_{\Pi} = \frac{4S_1S_2}{(S_1 + S_2)^2} \tag{2.19}$$

where S_1 is the cross-sectional area of the first part of the pipe and S_2 is the area in the second part of the pipe, both with unit m^2.

2.2.7. Infrasound

A common definition of infrasound is inaudible sound with a frequency below the lower limit of hearing. This is often referenced as being around 16 Hz. The definition is partly wrong as the lower level of hearing is not solely based of the frequency of the sound even though the frequency plays a big role in the audibility of a sound. What is correct, is the range of audible sound pressure levels gets more narrow at frequencies below 20 Hz compared to at 1000 Hz. At 16 Hz the range is about 50 dB wide and shifted toward higher sound pressure levels compared to at 1000 Hz where the range is about 100 dB [5]. This means infrasound is audible if the sound pressure is high enough. Since the report does not mainly focus on human hearing, the definition of infrasound will be sound below 20 Hz at all sound pressures.

Chapter 3.

Method

The experiments performed featured infrasound cooling, forced convection or natural convection of the steel plate in the cooling chamber. The temperature of the steel plate, the sound pressure, the frequency and the consumed power were measured.

3.1. The experiments

3.1.1. The experimental setup

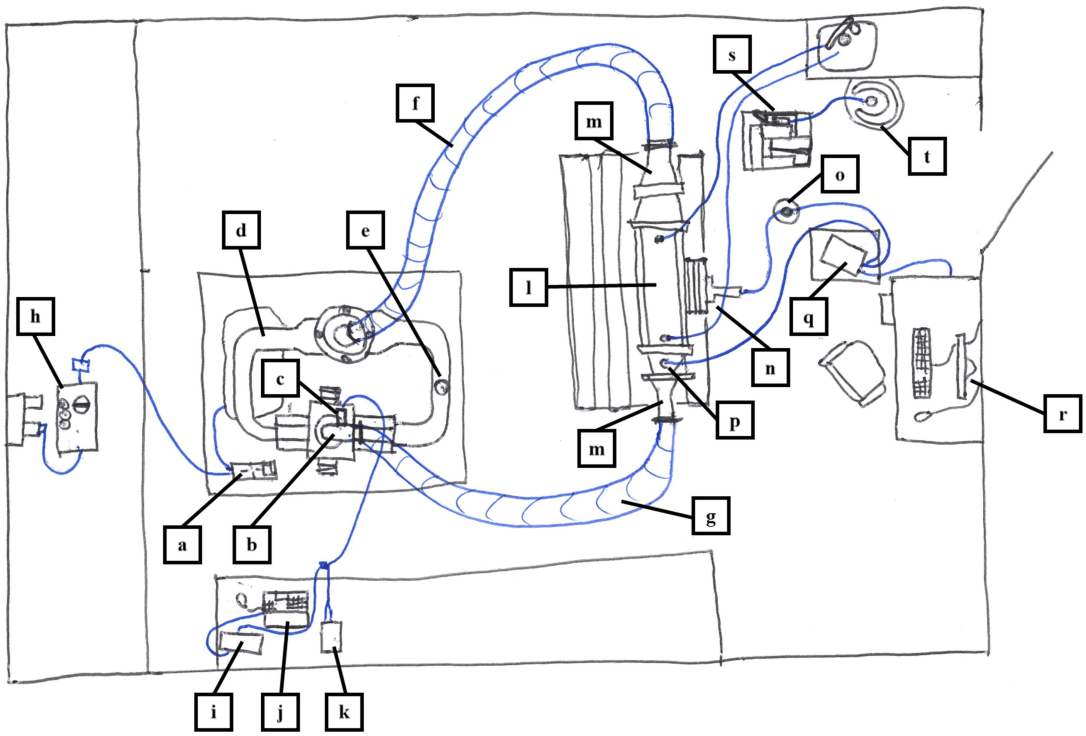

Figure 3.1.: Explanatory sketch of the layout of the experimental setup

The experimental setup consisted of:

- The pulsator constructed by Infrasonik AB, including:
  - Danfoss VLT Midi Drive frequency converter for controlling the frequency of the pulsator, [**a**] in Fig. 3.1
  - Two crankshafts with the four stroke length increments: 12 mm, 15 mm, 18 mm and 30 mm
  - Two crankshafts with the four stroke length increments: 42 mm, 46 mm, 50 mm and 54 mm
  - One short connecting pipe mounted to the bottom dead center side of the pulsator for connection of the longer resonance tube, [**b**] in Fig. 3.1
  - A STS 111737 pressure sensor with the range -0.5 bar to 0.5 bar gauge pressure and output 0 V to 10 V connected to the short pipe, [**c**] in Fig. 3.1
  - One long connecting pipe with two inlets and one outlet mounted to the top dead center side of the pulsator for connection of the shorter resonance tube, [**d**] in Fig. 3.1
  - A STS 133101 pressure sensor with input 0 bar to 10 bar gauge pressure and output 0 V to 10 V connected to the longer pipe (Unused), [**e**] in Fig. 3.1
- One shorter PVC hose with inner diameter of 75 mm and starting length 6.5 m used as resonance tube, [**f**] in Fig. 3.1. The actual length of the short pipe is denoted L_{short}.
- One longer PVC hose with inner diameter of 75 mm and starting length 7.4 m used as resonance tube, [**g**] in Fig. 3.1. The actual length of the long pipe is denoted L_{long}.
- A connection box bypassing the ground fault circuit breaker, [**h**] in Fig. 3.1
- A Tektronix TDS 2002C oscilloscope for measuring the signal of the pressure sensor, [**i**] in Fig. 3.1
- A laptop for loging the oscilloscope data using the software Tektronix OpenChoice Desktop, [**j**] in Fig. 3.1
- An Eventek KPS305D DC power supply providing the pressure sensor with the needed voltage, [**k**] in Fig. 3.1
- The cooling chamber constructed by Infrasonik AB, [**l**] in Fig. 3.1
- Two diffusers connecting the resonance tubes and the cooling chamber constructed by Infransonik AB, [**m**] in Fig. 3.1

- Two hoses for water cooling the cooling chamber where one was connected to a tap and the other drained in the sink
- The test plate with three 1.6 m long K-elements soldered to the middle of the heated portion, [**n**] in Fig. 3.1
- 6 coated copper wires of length 1.5 m for extension of the three K-elements
- A screw terminal block for connecting the three K-elements to the 6 extension wires
- Two condoms for water-proofing the cold junction
- A thermos for keeping ice water for the cold junction, [**o**] in Fig. 3.1
- A K-element for measuring the ambient temperature in the cooling chamber connected to a 5 m extension cable, [**p**] in Fig. 3.1
- An Agilent 34972A data logger for collecting the temperature measurements of the four K-elements, [**q**] in Fig. 3.1
- A stationary PC for logging the temperature data using the software Agilent BenchLink data logger 3, [**r**] in Fig. 3.1
- A PT-100 thermometer with the range 15 to 50 $°C$
- A Sievert Pro 86 propane torch with heating power 7.7 kW, [**s**] in Fig. 3.1
- A pressurized tank of propane, [**t**] in Fig. 3.1
- A spark lighter
- A heating station made of 7 bricks stacked on a 10 mm thick piece of inocel alloy
- A Leybold Didactic blower with modified nozzle with power 260 W
- A Pitot-tube connected to a Furness Controls Limited FC014 manometer
- A Testo 416 anemometer with a resolution of 0.1 m/s

A selection of important dimensions can be found in Tab. (3.1).

Table 3.1.: Important dimensions

Name	Symbol	Value	Unit
Heated steel plate width	L	120	mm
Total plate width including the two unheated fixed plates inside the cooling chamber and the heated plate	-	390	mm
Plate thickness	-	6	mm
Heated area of steel plate	A_s	14 400	mm^2
Length of the cooling chamber including diffusors	-	1.5	m
Inner diameter of the resonance tubes	-	75	mm
Cross sectional area of the resonance tubes	S_1	4418	mm^2
Cross sectional area of the cooling chamber without steel plate	-	8066	mm^2
Cross sectional area of the cooling chamber with steel plate	S_2	8966	mm^2
Height of cooling fins inside the cooling chamber	-	25	mm
Fin pitch	-	10	mm
Distance between the top of the fins of the two cooling elements	-	31	mm
Distance from the top of the cooling fins to the steel plate inside the cooling chamber	-	12.5	mm

3.1.2. The test plate

The test plate was constructed by Infrasonik AB. A 6 mm thick steel plate was cut into the shape shown in Fig. (3.2a). The heated area of the steel plate was 120 $mm \times 120$ mm. On the top side of the test plate, a 2 mm deep indentation with the radius 2 mm was drilled and a groove with the same depth was machined from the hole to the end of the handle. Three k-elements were held into place in the indentation with silicone without allowing them to touch, see Fig. (3.2b). The cables were fastened in the groove by pieces of steel welded across the groove. Permanently fixed inside the cooling chamber were two unheated 6 mm thick steel plates. With the heated steel plate inserted, the total length

of the unheated plates and the heated plate was 390 mm. The purpose of the unheated plates was to extend the obstruction of the flow further to better mimic a wide plate.

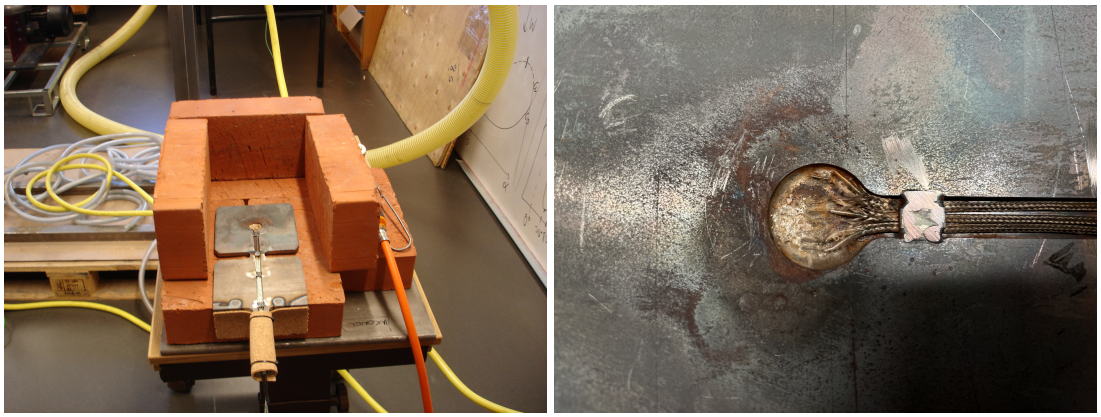

(a) **(b)**

Figure 3.2.: **(a)** The steel plate with heated area 120 $mm \times 120$ mm and thickness 6 mm, lying in the brick heating station with top side facing up.
(b) Close up of the three K-elements soldered in the 2 mm deep recess of the steel plate.

3.1.3. Measuring temperature

Four K-elements were used to measure the temperature. Three of them were soldered to the test plate, see Fig. (3.2b), and one of them was positioned inside one of the diffusors of the cooling chamber, see Fig. (3.4). The three K-elements soldered to the plate had wires too short to perform the experiments and had to be extended by connecting them to copper wires via a screw terminal block. The ends of the copper wires were sandpapered beforehand to remove the oxide layer, allowing connection. The copper wires were fastened in the cartridge of the Agilent 34972A data logger. The wires from the fourth K-element were also fastened in the cartridge of the data logger. From the beginning the three extended K-elements showed some discrepancy to the fourth when using internal reference for the temperature measurements. The fourth channel had been verified using a PT-100 thermometer. However, when the screw terminal block was kept in an ice bath, water proofed by two condoms and the reference was set to 0.00 $°C$, all four K-elements showed the same temperature and thus the ice bath was kept throughout the measurements. The K-elements required 10 minutes of ice bath cooling to show the correct temperature. The temperature measurement frequency was 1 measurement per second and was chosen as it was considered to give decent resolution in the time- and temperature span of the experiments.

3.1.4. Heating of the test plate

Welding gloves were put on before turning on the gas. The test plate was heated using a propane torch with its underside facing up . The gas was turned on and the torch was ignited using a spark lighter. The test plate was heated holding the propane torch approximately 5 - 10 cm above the plate, see Fig. (3.3a). The propane torch was moved in a zigzag pattern from left to right, towards and away from the person holding the propane torch. In all the experiments, the test plate was heated to at least 600 $°C$. Approximately, this process took 3 - 4 min. Before inserting the plate into the cooling chamber, the gas was turned off. Then the plate was flipped and inserted into the cooling chamber with the top side up, see Fig. (3.3b). The temperature of the plate when reaching the cooling chamber was around 570 $°C$.

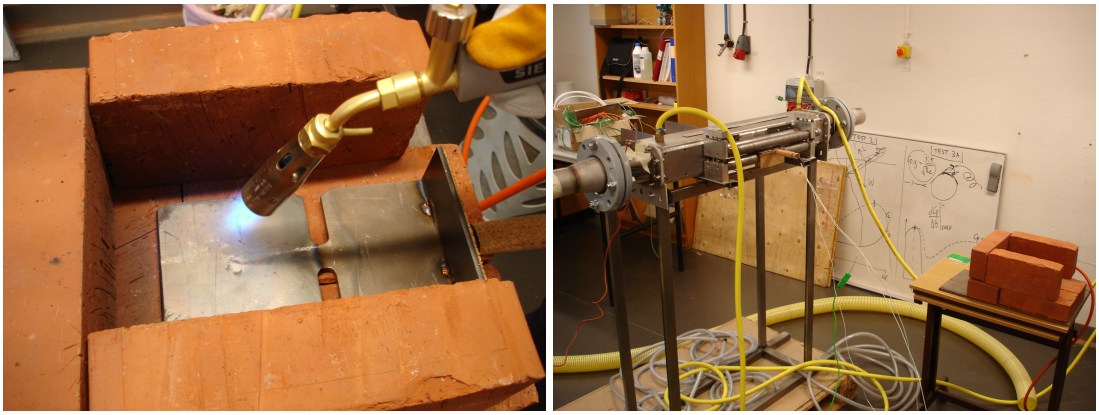

(a) **(b)**

Figure 3.3.: **(a)** Close up of the heating of the plate using the propane torch. The plate is positioned with underside up during heating.
(b) The heated plate inserted into the cooling chamber. In this case, the resonance tubes were disconnected from both sides to run an early idea of a forced convection trial.

3.1.5. Water cooling of the cooling chamber

A rubber hose was connected to a water tap in one end and to the inlet of the upper cooling element of the cooling chamber in the other end. Another rubber hose was connected from the outlet of the cooling element in one end, with the other end placed in the sink. The bottom cooling element was unused due to lack of hoses and connection possibilities. See Fig. (3.4) for a view inside the cooling chamber with both cooling elements visible. While cooling the chamber, the maximum flow at the coldest setting was always used for repeatability although no measurements were taken from the water temperature to verify this. This decision was made after a calculation of the potential

temperature increase of the water at normal flow from the tap. The calculation used the following assumptions:

1. $\dot{m}_w = 0.2\ kg/s$ (a low assumption)
2. $c_{p,w} = 4180\ J/(kgK)$
3. $A_s = 2 \cdot 0.12^2\ m^2$ heated area of the test plate neglecting sides and handle
4. $h_{max} = 200\ W/(m^2K)$ maximum total heat transfer coefficient including radiation
5. $\Delta T_{s,max} = T_i - T_b = 525\ °C$
6. All heat transfer from the plate will be absorbed by the cooling water

This gave

$$\dot{Q}_s = h_{max} A_s \Delta T_{max} = 200 \cdot 2 \cdot 0.12^2 \cdot 525 = 3024\ W$$

$$\dot{Q}_s = \dot{Q}_w = \dot{m}_w c_{p,w} \Delta T_w \Rightarrow \Delta T_w = \frac{\dot{Q}_s}{\dot{m}_w c_{p,w}} = \frac{3024}{0.2 \cdot 4180} = 3.6\ °C$$

where $\dot{Q}_s$ is the maximum heat transfer rate from the steel plate and $\dot{Q}_w$ is the heat transfer rate to the cooling water.

The calculation showed the highest possible increase in temperature of the cooling water and with more modest assumptions, the maximum temperature increase would be even lower. Therefore, the measurements were omitted as they were deemed to provide only little and unreliable information.

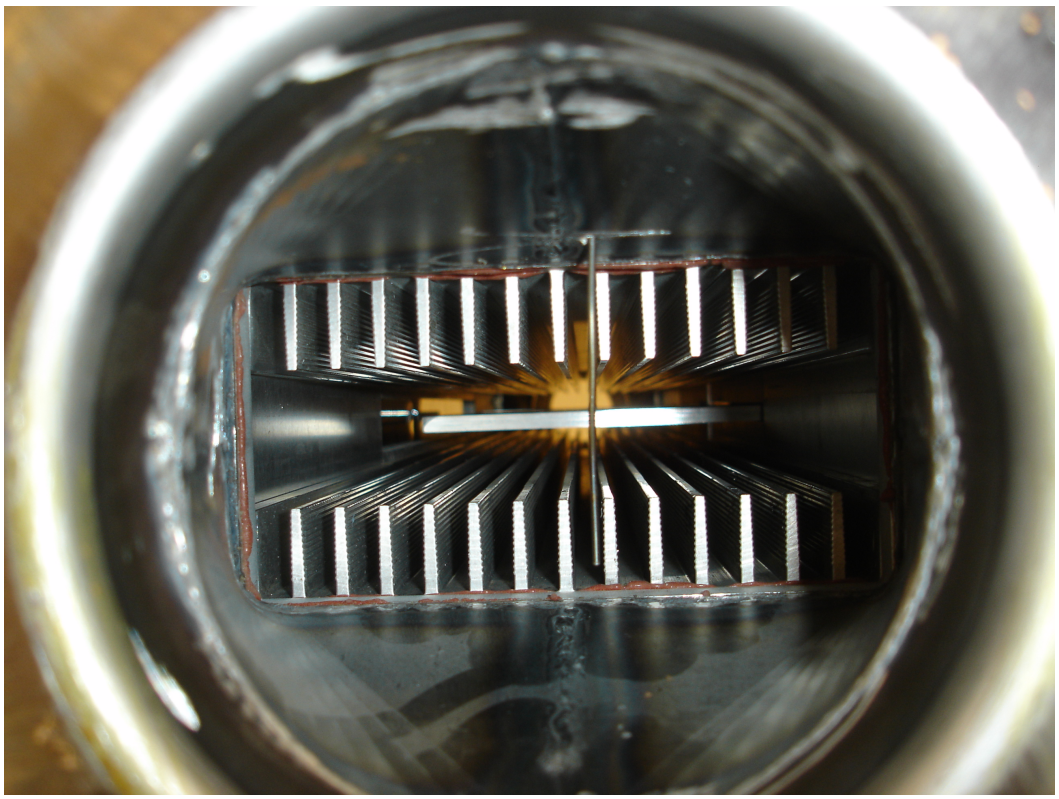

Figure 3.4.: A look inside the cooling chamber from the left side. The steel plate is inserted from the right in this picture. In the top and bottom of the channel are the cooling fins. The upper cooling element is the one being water cooled in the experiments. The infrasound travels along the axis pointing into the plane. Also visible is the fourth K-element used to measure the ambient temperature in the cooling chamber and one of the unheated extensions of the steel plate in the middle of the picture.

3.1.6. Cooling with infrasound

The test plate was placed in the heating station made of bricks with its underside facing up. The temperature measurement was started in the Agilent Benchlink software connected to the data logger. The water supply was turned to the coldest setting and the maximum flow. The gas was turned on and the heating of the plate began. When the plate reached around 300 $°C$, the pulsator was turned on by the person not heating the plate. When the plate had reached at least 600 $°C$, the plate was inserted into the cooling chamber with top side facing up. While waiting for the plate to cool down, the pressure sensor measurements were taken from the oscilloscope and saved to a computer using the Tektronix Open Choice Desktop software. The consumed power was read from the frequency converter and noted. When the measured temperature went below 50 $°C$, the measurement was turned off. Following, the pulsator and the water were turned off. If the experiment was the first try for the specific case, the plate was removed from the

chamber and placed with its underside facing up in the cooling station again and the second try was carried out. Otherwise, the plate was left in the cooling chamber.

3.1.7. Measuring sound pressure

The sound pressure sensor used was a gauge pressure sensor, meaning it output approximately 5 V corresponding to 0 bar when the pulsator was not running. It was positioned on the short pipe of the pulsator close to the crank house, see Fig. (3.5). The output from the sensor could be visualized using an oscilloscope. Due to the oscillatory nature of the sound wave produced by the pulsator, the output signal would show up as a sinusoidal wave on the oscilloscope. The maximum gauge pressure measurable by the sensor was 0.5 bar and corresponded to a 10 V output signal. The minimum gauge pressure was -0.5 bar, corresponding to a 0 V output signal. By using a built in feature of the oscilloscope called peak to peak voltage, the peak voltage could thus be calculated as

$$\hat{V} = V_{pk-pk}/2 \tag{3.1}$$

where $\hat{V}$ is the voltage amplitude with unit V and V_{pk-pk} is the peak to peak voltage with unit V.

The voltage amplitude output was then converted to sound pressure amplitude by multiplication with a factor of 10 to get kPa as

$$\hat{p} = \hat{V} \cdot 10\ kPa/V \tag{3.2}$$

where $\hat{p}$ is the sound pressure amplitude with unit kPa.

When the first try of a new case was performed, the oscilloscope was read during the cooling of the plate in the cooling chamber. The oscilloscope was connected to a laptop and using the OpenChoice desktop software, two pictures depicting the present oscilloscope screen were saved. Some consideration was put in the selection of the specific frame to capture since the measured frequency and peak to peak voltage constantly fluctuated. The two frames were taken at the most stable conditions in regard to the peak to peak voltage. Because of the fluctuations, no new frames were captured for the second try. However, the oscilloscope was checked every second try as well to ensure it agreed with the first try. The precision of the oscilloscope output was 4 digits.

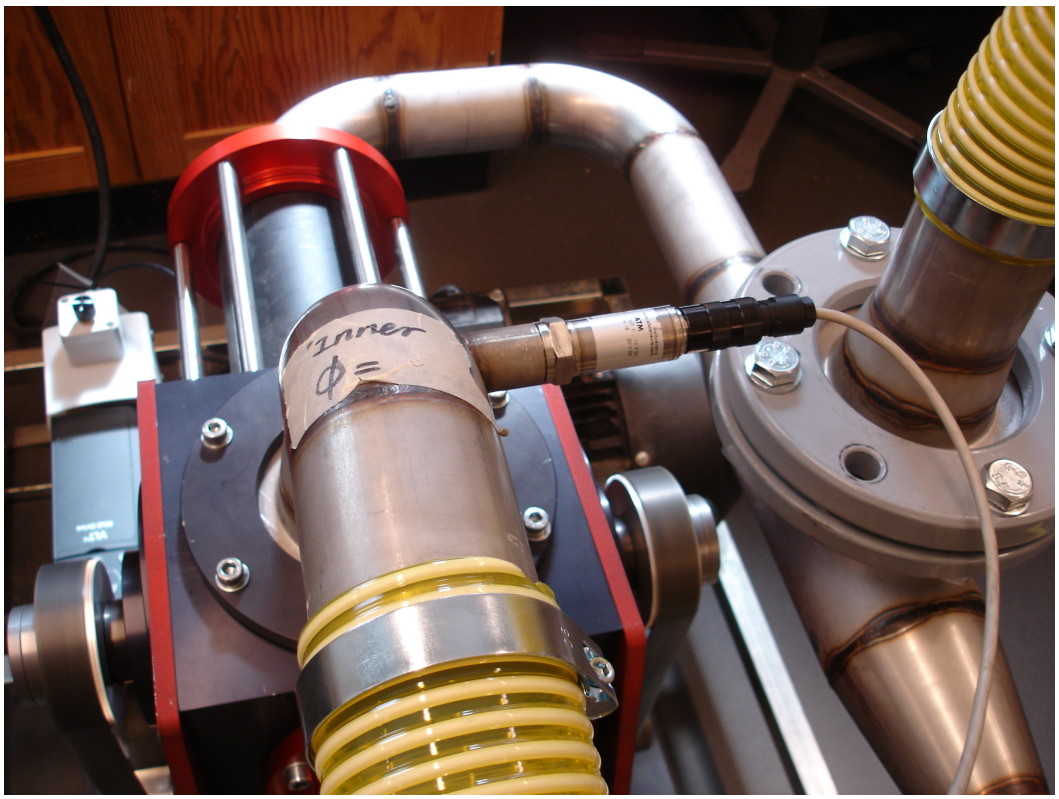

Figure 3.5.: The pressure sensor connected to the short pipe on the pulsator. The grey cable was connected to the oscilloscope.

3.1.8. Changing resonance frequency

Attempts to predict the tube lengths needed to produce a certain resonance frequency were made. The formula used was

$$\frac{\lambda}{2} = \frac{c}{2f} = L_R + \Delta L_{Correction} \tag{3.3}$$

where λ is the wavelength with unit m, c is the sound speed with unit m/s, f is the frequency with unit Hz, L_R is the total length of tube in the system with unit m and $\Delta L_{Correction}$ is the correction of tube length including the length of pipe in the pulsator and the cooling chamber with unit m.

L_R was defined as $L_R = L_{long} + L_{short}$ with the relation $L_{long} = L_{short} + 0.9\,m$. This was to account for the longer pipe on one side of the pulsator. One side of the pulsator had a longer metal pipe solely because of design choices. The thought was $\Delta L_{Correction}$ would remain constant as the length of the pipes connected to the pulsator and the length of cooling chamber were constant. From the known first scenario, $\Delta L_{Correction}$ could be

calculated. With the assumption of $c = 340\ m/s$, the needed L_R was calculated for the next frequency. As this phenomenon was not predicted to be linear, $\Delta L_{Correction}$ was updated after each cut with the measured frequency instead of the predicted frequency. The order of the frequencies was 9.9 Hz, 11.5 Hz, 13.1 Hz, (new longer tube was bought), 5.5 Hz, 7 Hz, 8.3 Hz and 9.6 Hz. See Tab. (3.2) for real data frequencies and the calculated $\Delta L_{Correction}$.

Table 3.2.: Frequencies with their corresponding tube lengths and correction length

$f\ [Hz]$	$L_{long}\ [m]$	$L_{short}\ [m]$	$L_R\ [m]$	$\Delta L_{Correction}\ [m]$
5.5	14	13.1	27.1	3.8
7	10.7	9.8	20.5	3.8
8.3	8.6	7.7	16.3	4.2
9.6	(-)	(-)	(-)	(-)
9.9	7.4	6.5	13.9	3.3
11.5	5.9	5	10.9	3.9
13.1	5	4.1	9.1	3.9

The two resonance tubes were disconnected from the cooling chamber while still being connected to the pulsator. The longer tube was straightened out on the floor and the part to be cut off was measured using a tape measure. One person marked the tube with a permanent marker while the other held the tube straight. The tube was cut using a snap-off knife while one person bent the tube to facilitate cutting. From the second shorter tube, the same length of tube was removed.

The two shortened resonance tubes were refastened to the cooling chamber. The pulsator was started to check for leakage of air in the connections to the cooling chamber.

To find the resonance frequency, the test plate was inserted into the cooling chamber, the pulsator was turned on and a frequency sweep was performed with the frequency converter. Beginning 2 Hz below the calculated new frequency, the control frequency of the frequency converter was increased by 0.1 Hz every 5 seconds while the output of the pressure sensor on the oscilloscope was filmed using a mobile phone. When a frequency 2 Hz higher than the calculated frequency was found, the sweep was done in reverse down past the calculated new frequency while continuing to film the oscilloscope. Then the video footage was reviewed and the frequency corresponding to the peak amplitude was assumed to be the resonance frequency. The control frequency was then adjusted to give the correct resonance frequency.

3.1.9. Changing stroke length

First, the connection box was turned off and the pulsator was ensured to be turned off before proceeding. The cable connecting the pressure sensor to the oscilloscope was disconnected from the pressure sensor and was stored on the work bench during the whole change. The bent pipe connecting the longer tube to the crank house was removed from the crank house. The shorter tube was disconnected from the longer connecting pipe. The longer connecting pipe was removed from the two cylinders. One of the two cylinders was removed from the crank house, see Fig. (3.6a), and the piston operating in the now removed cylinder was unscrewed from its crank. Next, if the new stroke length was found on the same set of cranks, the other piston was unscrewed from its crank and was screwed into a new hole on the same crank corresponding to the new stroke length. The belt tension was released on the side where no piston was attached and the connection between the crank and the belt cog wheel was loosened to allow adjustment of the crank position. The other piston was screwed into the hole on the crank corresponding to the same stroke length as the other piston. The angular position of the free crank was adjusted to be 180° out of phase with the fixed crank by sight of eye. The connection between the free crank and the belt cog wheel was tightened, see Fig. (3.6b), and the phase was checked again to ensure no slippage occurred when tightening the connection.

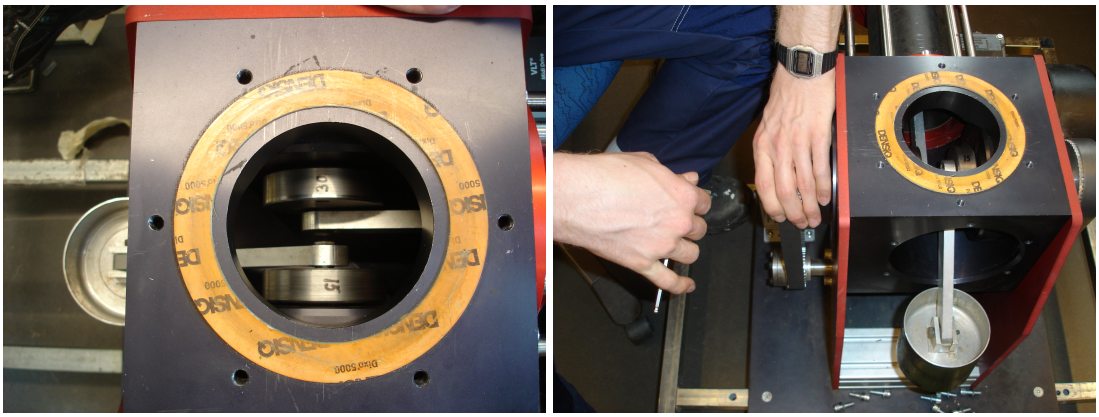

(a) **(b)**

Figure 3.6.: **(a)** Looking down the crank house with one cylinder and the short pipe removed. The holes in the crank are slightly visible. The cranks are 180° out of phase.
(b) The connection between the belt and the crank is tightened. The synchronization of the two cranks is done by eyesight.

If the new stroke length was found on the other set of cranks, the other piston was unscrewed from its crank and its connecting rod was place out of the top of the crank house. The belt tension was loosened on both sides and the connections between the cranks and their respective belt cog wheels were loosened on both sides. The connections and the belt cog wheels were removed on both sides. The piece holding the cranks to the crank house was removed on both sides. The clamp holding the crank to the previously

removed piece was removed and the crank was switched on both sides. Next followed the procedure in reverse up until tightening the connections between cranks and belt cog wheels. One side was tightened while the other was left loose to allow the angular position to be adjusted according to the method explained at the end of the previous paragraph.

3.1.10. Forced convection

A fan with power 260 W was mounted to the cooling chamber using tape, see Fig. (3.7). One of the diffusors had been removed prior to mounting the fan and the resonance tube in the other end had been removed to allow free flow in the chamber. The nozzle diameter of the fan was close to the diameter of the inlet of the cooling chamber without the diffusor. The water was turned on at the coldest setting with maximum flow and the temperature measurement started. The plate was heated using previously explained methodology. To try to replicate the methodology used when cooling the plate with the pulsator as precisely as possible, the following method was used. When the plate reached 300 $°C$, the fan was turned on at maximum power. When the plate reached 600 $°C$, the plate was slid into the cooling chamber and was allowed to cool. Upon reaching 50 $°C$, the measurement was stopped and the water was turned off. Beforehand, the flow out of the chamber when running the fan at maximum power was measured with an anemometer.

3.1.11. Natural convection in the water cooled chamber

For this experiment, the ends of the cooling chamber were sealed with tape. Firstly, the water was adjusted to maximum flow and coldest temperature. The temperature measurement was started and the steel plate was heated using the methodology previously explained. When the plate reached 600 $°C$, it was slid into the cooling chamber and was left to cool. When T_s went below 50 $°C$, the measurement was stopped and the water was turned off.

3.2. The calculations

3.2.1. Choosing values for constant properties

Many of the values chosen for the constant properties were inherited from SSAB and Infrasonik AB as they had done previous experiments and possessed knowledge in the field. See Table 3.3

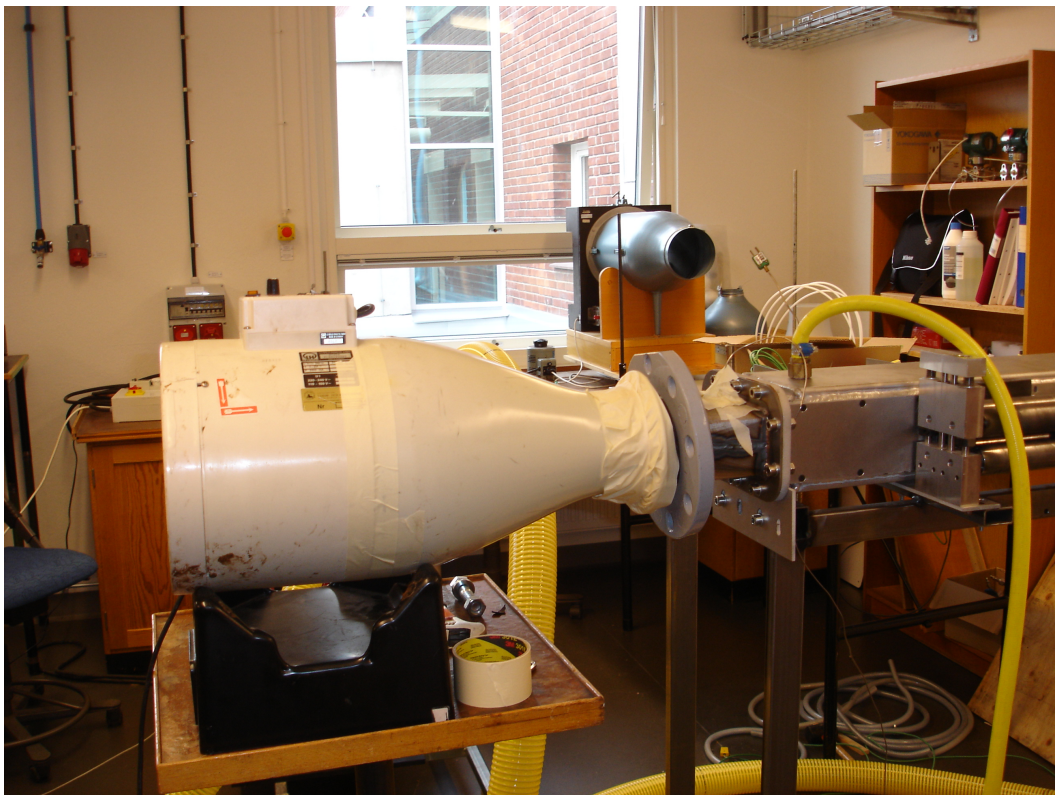

Figure 3.7.: The fan used for forced convection attached using tape to the cooling chamber.

3.2.2. Preparing the data

The output from the data logger was in the form of .csv files with 6 columns as follows: scan number, elapsed time, channel 1 [$°C$], channel 2 [$°C$], channel 3 [$°C$] and channel 4 [$°C$]. Channel 1 to 3 corresponded to the three K-elements soldered to the test plate while channel 4 corresponded to a K-element positioned inside the diffusor of the cooling chamber. As the scan frequency chosen was one measurement per second, with the first scan at 0.00 s, the scan number minus one was chosen as the time. This was because the elapsed time was not given in seconds but in the format $days : hours : minutes : seconds : milliseconds$.

Channel 3 had very unreliable measurements and would differ depending on the angle of the plate and was therefore omitted. The temperature used as T_s was the average between channel 1 and 2. The ambient temperature used was at first the temperature measured by channel 4, but was at a later stage changed to the constant T_b as the measurements of channel 4 was not considered to give a good representation of the surface temperature of the cooling elements due to its position away from the cooling elements and the plate.

The temperature data could then be visualized by plotting T_s as a function of time.

Table 3.3.: Constant parameters chosen

Name	Symbol	Value	Unit	Source
Density of steel	ρ_s	7850	kg/m^3	Same as in studies by Infrasonik AB
Specific heat capacity of steel	c_s	480	$J/(kgK)$	Same as in studies by Infrasonik AB
Emissivity of steel	ε	0.59	$(-)$	Same as in studies by Infrasonik AB
Density of air at T_b	ρ_{a,T_b}	1.184	kg/m^3	taken from [2] at 25 $°C$ and 1 atm
Speed of sound in air at T_b	c	347.4	m/s	calculated from Eq. (2.11) at 25 $°C$
Kinematic viscosity of air at T_b	ν	$1.562 \cdot 10^{-5}$	m^2/s	taken from [2] at 25 $°C$ and 1 atm
Thermal conductivity of air at T_f	k_f	$4.418 \cdot 10^{-4}$	$W/(mK)$	taken from [2] at 300 $°C$ and 1 atm
Prandtl number	Pr	0.7	$(-)$	standard value for most gases

3.2.3. Calculating the heat transfer coefficient using lumped body analysis

The maximum heat transfer coefficient was assumed to be no larger than 200 $W/(m^2K)$ and the the Biot number could thus be calculated as $Bi = hL_c/k \approx 0.013$. As this meant the value was smaller than 0.1, the lumped body analysis could be used [2]. The upper limit for the heat transfer coefficient, while still keeping $Bi < 0.1$, was $h_{max} < Bik/L_c = 500\ W/(m^2K)$. For a lumped body, the relation between temperature and time can be written as

$$\frac{\theta}{\theta_i} = \frac{T_s - T_\infty}{T_i - T_\infty} = e^{-bt} \tag{3.4}$$

Eq. (3.4) was modified to include $T_b = 300\ K = 27\ °C$ instead of T_∞

$$\frac{\theta}{\theta_i} = \frac{T_s - T_b}{T_i - T_b} = e^{-bt} \tag{3.5}$$

where T_s is the temperature of the plate in $°C$ at t seconds, T_∞ is the ambient temperature in $°C$, T_i is the initial plate temperature in $°C$, t is the time in seconds and b is the time constant defined as

$$b = \frac{hA_s}{m_s c_s} \tag{3.6}$$

where h is the heat transfer coefficient with unit $W/(m^2K)$, A_s is the heat transfer area of the plate with unit m^2, m_s is the mass of the plate with unit kg and c_s is the specific heat capacity of steel with unit $J/(kgK)$.

To remove the uncertainty of calculating the area and mass of the plate, the relation

$$\frac{A_s}{m_s} = \frac{1}{\frac{V_s}{A_s}\frac{m_s}{V_s}} = \frac{1}{L_c \rho_s} \tag{3.7}$$

was used.

From Eq. (3.6) and (3.7), the time constant b could be written as

$$b = \frac{h}{\rho_s L_c c_s} \tag{3.8}$$

From Eq. (3.8), h could be expressed as

$$h = b\rho_s L_c c_s \tag{3.9}$$

The heat transfer coefficient was calculated in intervals of 50 $°C$, beginning at 550 $°C$ and ending at 50 $°C$. This was done because h was not constant across all temperatures. However, in intervals of 50 $°C$, h could be considered constant. For every data point in the interval, θ/θ_i was calculated. Time was taken as time elapsed from the beginning of the interval to the actual data point. By taking the natural logarithm on both sides of Eq. (3.5), the relation was linearized. After division with $-t$ the new relation was

$$b = \frac{-ln(\theta/\theta_i)}{t} \tag{3.10}$$

The mean b was calculated as the mean slope of the cooling curve in an interval according to

$$b_{mean} = \frac{\sum -ln(\theta/\theta_i)}{\sum t} \tag{3.11}$$

Meaning, h_{mean} in an interval was calculated as $h_{mean} = b_{mean}\rho L_c c_s$. From now on, h_{mean} will be referred to as $h_{Tot} = h_{Rad} + h_{Conv}$ as it included both radiative and convective heat transfer. To get the h_{Conv}, h_{Rad} was removed from h_{Tot}. This was achieved by calculating the ratio of radiative to total heat transfer in the interval and scaling the heat transfer coefficient accordingly. To avoid using area and volume in the calculations, Q_{Tot}/V and Q_{Rad}/A was calculated as

$$Q_{Tot}/V = \rho_s c_s (T_{end} - T_i) \qquad [J/m^3] \tag{3.12}$$

where T_{end} is the end temperature in the interval in $°C$, and [2]

$$Q_{Rad}/A_s = \varepsilon\sigma \int (T_s(t)^4 - T_b^4) dT_s \qquad [J/m^2] \tag{3.13}$$

where $T_s(t)$ is the temperature of the steel plate with unit K, T_b is the bulk temperature with unit K, ε is the emissivity of the steel and σ is the Stefan Boltzmann constant $\sigma = 5.67 \cdot 10^{-8}\ W/(m^2K^4)$.

By combining Eq. (3.12) and Eq. (3.13), the ratio could be written as

$$Q_{Ratio} = \frac{Q_{Rad}/A_s}{Q_{Tot}/V} L_c = \frac{Q_{Rad} V_s}{Q_{Tot} A_s} \cdot \frac{A_s}{V_s} = \frac{Q_{Rad}}{Q_{Tot}} \tag{3.14}$$

The convective heat transfer h_{Conv} was then calculated as

$$h_{Conv} = (1 - Q_{Ratio}) h_{Tot} \tag{3.15}$$

For every scenario, four different heat transfer coefficients were calculated:

1. $\langle h_{Tot} \rangle$ is the mean total heat transfer coefficients across all intervals except 550 to 500 $°C$. It is a sum och the convective and radiative heat transfer coefficients.
2. $h_{Conv,\,300}$ is the convective heat transfer coefficient in the interval 350 to 300 $°C$
3. $\langle h_{Conv} \rangle$ is the mean convective heat transfer coefficients across all intervals except 550 to 500 $°C$
4. $\langle h_{Conv\,C} \rangle$ is the mean corrected convective heat transfer coefficients across all intervals except 550 to 500 $°C$

The interval from 550 to 500 $°C$ was excluded from the averages as the heat transfer coefficient in this interval was no trusted as it was close to the insertion temperature of the plate.

3.2.4. Correction of the convective heat transfer coefficient to account for the effect of variable properties

Given a wall with a uniform heat flux cooled by convection, Newtons law of cooling states:

$$\dot{Q} = hA_s(T_s - T_\infty) \tag{3.16}$$

where $\dot{Q}$ is the heat transfer rate with unit W. With constant fluid properties and fully developed flow, the heat transfer coefficient h is constant [2]. This means $\dot{Q}$ is expected to vary with varying T_s while h remains constant. However, the calculated convective heat transfer coefficient h_{Conv} was observed to decrease with increasing T_s. Therefore, the corrected convective heat transfer coefficient was calculated to take into account the effects of variable fluid properties.

A film layer with temperatures close to T_s surrounding the test plate was assumed to exist. Given the high temperatures of air in the film layer, $Re = uL/\nu$ was assumed to decrease since the viscosity of air increases with temperature [2]. By correcting the convective heat transfer coefficient, the results could then be compared to existing textbook scenarios and other studies to broaden the understanding of the infrasound cooling phenomenon.

To correct h_{Conv}, the relation used was [7]

$$\frac{Nu}{Nu_{Corr}} = \left(\frac{T_s}{T_b}\right)^n \tag{3.17}$$

where $Nu = h_{Conv}L/k$ is the Nusselt number using constant properties of air, $Nu_{Corr} = h_{Conv\,C}L/k$ is the Nusselt number using variable properties of air, T_s is the temperature of the test plate with unit K, T_b is the bulk temperature with unit K and n is an empirically determined constant. For heated air, $n = -0.5$ is appropriate [7].

Since characteristic length L and heat conductivity k were assumed to be constant, Eq. (3.17) could be rewritten as

$$\frac{\langle h_{Conv}\rangle}{\langle h_{Conv\,C}\rangle} = \left(\frac{T_s}{T_b}\right)^{-0.5} \tag{3.18}$$

To calculate the mean corrected convective heat transfer coefficient $\langle h_{Conv\,C}\rangle$, in each interval, Eq. (3.18) was rewritten as

$$\langle h_{Conv\,C}\rangle = \langle h_{Conv}\rangle \left(\frac{T_s}{T_b}\right)^{0.5} \tag{3.19}$$

The T_s used was the mean plate temperature of the interval, meaning $T_s = (T_i + T_{end})/2$. T_b is equal to 300 K.

3.2.5. Calculating the particle velocity in the cooling chamber

Since there was a cross sectional difference between the tube and the cooling chamber, the calculated particle velocity based on the measured sound pressure in the tube had to be corrected. This was done to generalize the results further and make them comparable to existing data.

The formula used to calculate the particle velocity amplitude in the cooling chamber was a combination of Eq. (2.13), Eq. (2.14) and Eq. (2.15) and was written as

$$\hat{u}_{ch} = \frac{p}{z} \cdot \frac{Z_{tube}}{Z_{ch}} = \frac{\hat{p}}{\rho_a c} \cdot \frac{S_{tube}}{S_{ch}} \tag{3.20}$$

where $\hat{u}_{ch}$ is the particle velocity amplitude in the chamber with unit m/s, p is the sound pressure with unit Pa, z is the specific acoustic impedance with unit $Pa \cdot s/m$, Z_{tube} and Z_{ch} are the acoustic impedances in the tube and the cooling chamber respectively, both with unit $Pa \cdot s/m^3$, $\hat{p}$ is the sound pressure amplitude measured by the pressure sensor with unit Pa, ρ_a is the density of air with unit kg/m^3, c is the speed of sound in air with unit m/s, and S_{tube} and S_{ch} are the cross sectional areas of the tube and the cooling chamber respectively, both with unit m^2.

3.2.6. Heat transfer coefficient as a function of particle velocity amplitude in the chamber

To visualize the important parameters affecting the heat transfer coefficient, the calculated heat transfer coefficients were first assumed to be a function of the sound pressure. Since the corrected particle velocity amplitude was directly derived from the measured sound pressure, both relations would be alike, only scaled by a constant. For generalizability, the corrected particle velocity amplitude was chosen. All four calculated single point heat transfer coefficients were plotted against their calculated corrected particle velocity amplitude in four different figures. The data was fitted using a power series and the function was plotted. The equation was on the general form

$$h = a \cdot (\hat{u}_{ch})^b \tag{3.21}$$

where h is a single point heat transfer coefficient with unit $W/(m^2K)$, a and b are constants determined by the fit and $\hat{u}_{ch}$ is the corrected particle velocity amplitude with unit m/s.

Two additional lines were plotted representing an increase of 5% and decrease of 5% in the power series to provide a visualization of the validity of the fit.

3.2.7. Heat transfer coefficient as a function of frequency

The same procedure was also done for the heat transfer coefficient as a function of frequency. The fitted curve had the general form

$$h = a \cdot f^b \tag{3.22}$$

where f is the frequency with unit Hz.

3.2.8. Heat transfer coefficient as a function of the corrected particle velocity amplitude and frequency

The heat transfer coefficient was now assumed to be a function of both corrected particle velocity amplitude and frequency and a fit on the general form

$$h = a \cdot (\hat{u}_{ch})^b \cdot f^c \tag{3.23}$$

was employed. This was plotted as a surface in 3D with the data points overlaid.

3.2.9. Consumed power as a function of corrected particle velocity and frequency

Following the methodology in the previous three subsections, the consumed power was fitted according to the three equations

$$P = a \cdot (\hat{u}_{ch})^b \tag{3.24}$$

$$P = a \cdot f^b \tag{3.25}$$

$$P = a \cdot (\hat{u}_{ch})^b \cdot f^c \tag{3.26}$$

3.2.10. Corrected particle velocity as a function of stroke length and frequency

Following the previous methodology, the corrected particle velocity was fitted according to equations

$$\hat{u}_{ch} = a \cdot SL^b \tag{3.27}$$

$$\hat{u}_{ch} = a \cdot f^b \tag{3.28}$$

$$\hat{u}_{ch} = a \cdot SL^b \cdot f^c \tag{3.29}$$

where SL is the stroke length in mm.

3.2.11. Assessing the goodness of the fit

The goodness of the fit was assessed by calculating the standard error of the residuals according to the general formula

$$SE = \sqrt{\frac{\sum(y_i - y_p(x_i))^2}{n}} \tag{3.30}$$

where SE is the standard error with the same unit as the measured parameter y_i, y_i is the actual value of the response variable obtained from the data set, $y_p(x_i)$ is the predicted value of the response variable based on the parameter x_i from the data set and n is the sample size.

Eq. (3.22) and Eq. (3.23) were applied as $y_p(x_i)$ in Eq. (3.30). To normalize SE, it was divided by the mean value of the response variable from the data set. The lowest normalized SE corresponded to the best curve fitting of the data.

3.2.12. Comparison of infrasound cooling and forced convection at a similar mean velocity

The comparison between infrasound cooling and forced convection was made. For comparability, the calculated corrected particle velocity amplitude $\hat{u}_{ch}$ was converted to corrected mean absolute velocity as the forced convection was not an oscillating flow.

The formula used was

$$\langle \hat{u}_{ch} \rangle = \frac{1}{2\pi} \int_0^{2\pi} |u_{ch}(\omega t)| \, d(\omega t) = \frac{2}{\pi} \hat{u}_{ch} \tag{3.31}$$

The flow of the forced convection was measured using an anemometer and was considered mean flow by default. A data set with infrasound cooling was chosen having a $\langle \hat{u}_{ch} \rangle$ value close to the measured $\langle u_{F.Conv} \rangle$. The two cooling curves were plotted, as well as the cooling curve for the natural convection.

3.2.13. Comparison of Nusselt number of the forced convection to existing formulas

To provide insight in the heat transfer situation in the cooling chamber, the heat transfer was made non-dimensional as the average Nusselt number over the flat plate according to Eq. (3.32). The flow velocity was non-dimensionalized in Eq. (3.33) as the Reynolds number across a flat plate. Both relations were found in [2].

$$Nu_L = \frac{hL}{k} \tag{3.32}$$

$$Re_L = \frac{uL}{\nu} \tag{3.33}$$

where h is the heat transfer coefficient with unit $W/(m^2K)$, L is the length of the plate with unit m, k is the thermal conductivity with unit $W/(mK)$, u is $\hat{u}_{ch}$ with unit m/s.

The formula for the average Nu_L for laminar flow over an isothermal flat plate [2] was found as

$$Nu_L = 0.664 Re_L^{0.5} Pr^{1/3} \tag{3.34}$$

The respective formula for flat plates with uniform heat flux [2] was

$$Nu_L = 0.906 Re_L^{0.5} Pr^{1/3} \tag{3.35}$$

The two theoretical forced convection lines were plotted using Eq. (3.34) and (3.35) in the Re_L range $0 - 8 \cdot 10^4$. The four calculated heat transfer coefficients were converted to Nu_L using Eq. (3.32) and then they were plotted against their common Re_L, calculated using Eq. (3.33), for comparison to the theoretical cases.

3.3. On the accuracy of measurements and systematic errors

Some inaccuracies and errors occurred in the experiments. The oscilloscope only featured four digits meaning it showed either two or three decimals depending on if the value had one or two digits before the decimal. Measurements from the oscilloscope usually had a $\pm 0.05\ V$ or $\pm 0.5\%$ difference. The required power differed roughly by $\pm 0.5\ kW$ or $\pm 25\%$. Temperature measurements had good accuracy as no unstable behavior was observed in channel 1 and 2 and therefore the standard accuracy for K-elements could be considered $\pm 0.3\ ^{\circ}C$ or, in this case, $\pm 0.1\%$. However, channel 3 was eliminated as it had very unstable and erratic behavior. Channel 4 was also omitted and the constant bulk temperature was used instead. The anemometer used to measure the mean velocity in the cooling chamber for the forced convection had an accuracy of $\pm 0.2\ m/s$ or $\pm 1\%$.

Chapter 4.

Results

Please note, as the $\hat{u}_{ch}$ symbol was not available in Matlab, $\hat{u}_{ch}$ appears in the figures as u.

4.1. Heat transfer coefficient as $g(T_s)$

The figures featured in this section of the result can be found in full size in appendix A.

4.1.1. Total heat transfer coefficient as a function of steel plate temperature

The total heat transfer coefficient shows a generally decreasing trend with increasing steel plate temperature across all frequencies and corrected particle velocities, see Fig. (4.1a - 4.1g). However, a slight increase in h_{Tot} can be observed between 450 $°C$ and 500 $°C$. It is most noticeable in Fig. (4.1e). Across all f and $\hat{u}_{ch}$, h_{Tot} decreases monotonically with increasing T_s, although the 13.6 m/s line is breaking the trend towards the higher T_s in Fig. (4.1f). The range of h_{Tot} values is best illustrated by Fig. (4.1f) and is approximately 65 - 175 $W/(m^2K)$.

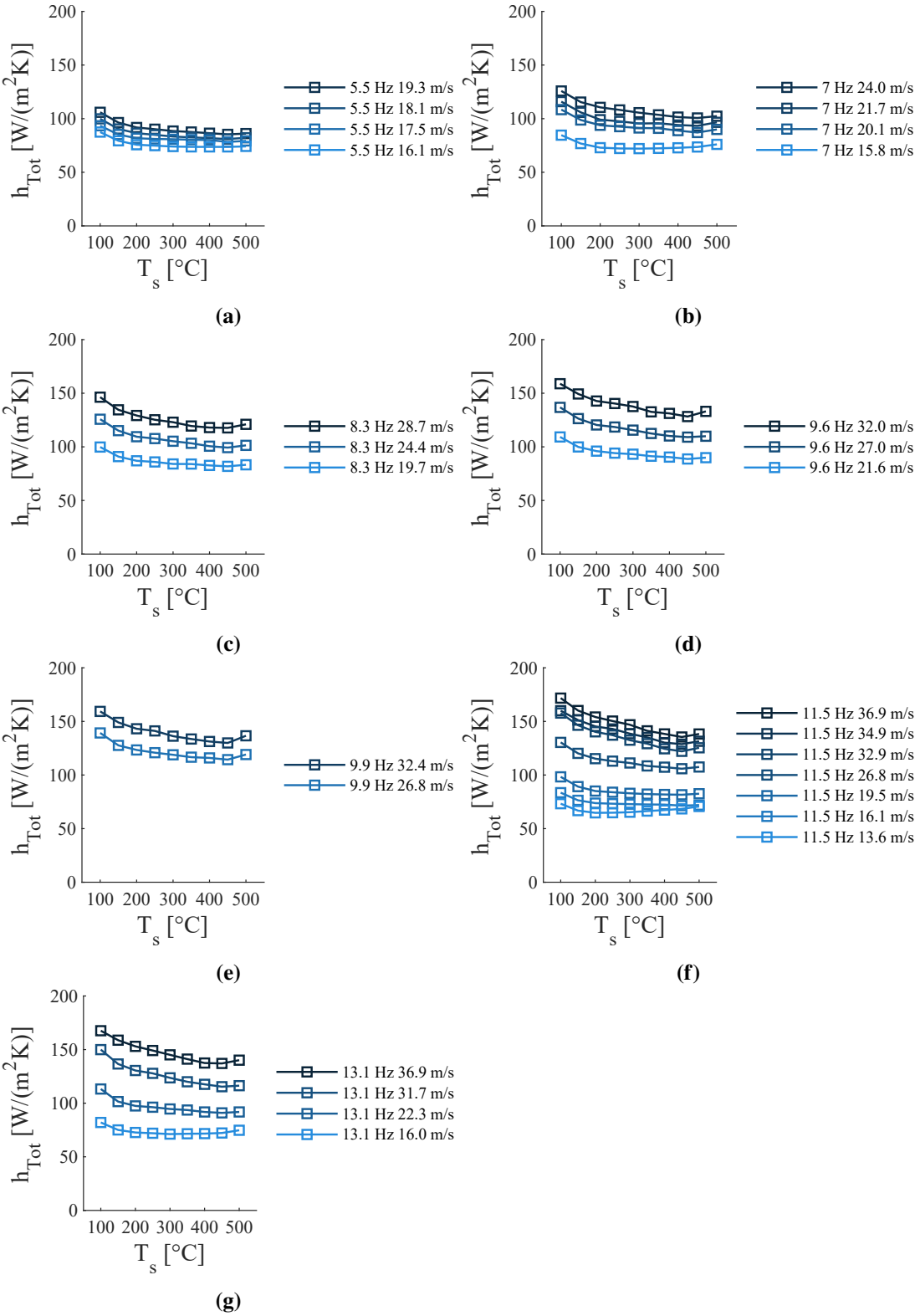

Figure 4.1.: Total heat transfer coefficient h_{Tot} at different steel plate temperatures T_s and varying corrected particle velocities $\hat{u}_{ch}$ at **(a)** $f = 5.5\ Hz$, **(b)** $f = 7\ Hz$, **(c)** $f = 8.3\ Hz$, **(d)** $f = 9.6\ Hz$, **(e)** $f = 9.9\ Hz$, **(f)** $f = 11.5\ Hz$ and **(g)** $f = 13.1\ Hz$

4.1.2. Convective heat transfer coefficient as a function of steel plate temperature

The convective hat transfer coefficient shows a more decreasing trend with increasing steel plate temperature compared to the total heat transfer coefficient, see Fig. (4.2a - 4.2g). The decrease of h_{Conv} with respect to increase of T_s is monotonic except in some cases between 450 $°C$ and 500 $°C$, see for example Fig. (4.2e). The range of h_{Conv} values are seen in Fig. (4.2f) and is approximately 50 - 170 $W/(m^2K)$.

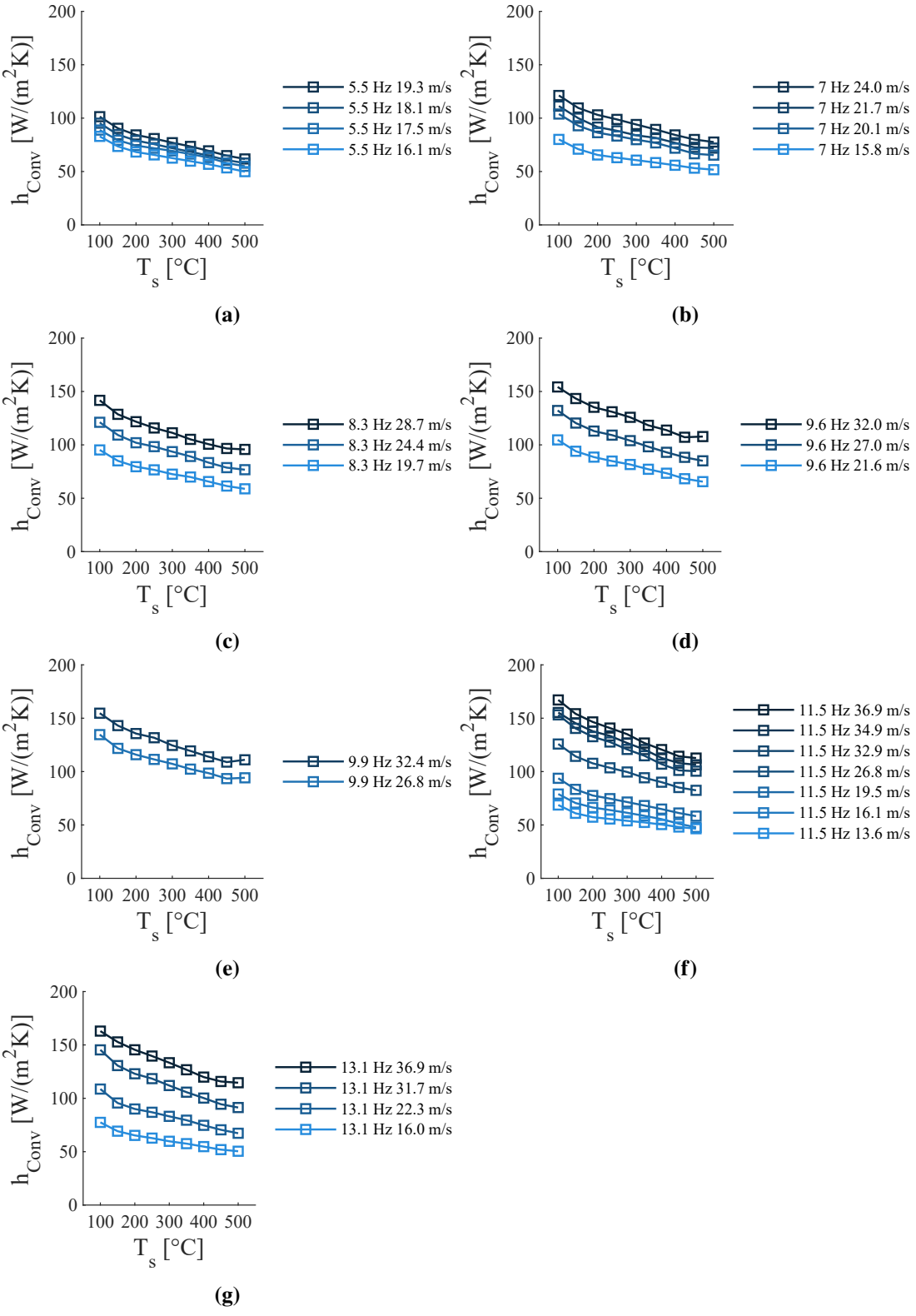

Figure 4.2.: Convective heat transfer coefficient h_{Conv} at different steel plate temperatures T_s and varying corrected particle velocities $\hat{u}_{ch}$ at **(a)** $f = 5.5\ Hz$, **(b)** $f = 7\ Hz$, **(c)** $f = 8.3\ Hz$, **(d)** $f = 9.6\ Hz$, **(e)** $f = 9.9\ Hz$, **(f)** $f = 11.5\ Hz$ and **(g)** $f = 13.1\ Hz$

4.1.3. Corrected convective heat transfer coefficient as a function of steel plate temperature

The corrected convective heat transfer coefficient displays a flatter profile across all steel plate temperatures compared to the total and the convective heat transfer coefficient, see Fig. (4.3a - 4.3g). $h_{Conv\,C}$ does not decrease or increase monotonically and often has a local peak value between 250 $°C$ and 350 $°C$, see Fig. (4.3f). The tail between 100 $°C$ and 150 $°C$ can either be higher or lower than the local maximum, see Fig. (4.3g). Furthermore, the same is true for the tail between 450 $°C$ and 500 $°C$, see Fig. (4.3c) and Fig. (4.3g). The range of $h_{Conv\,C}$ values is between 70 and 180 $W/(m^2K)$ and can be seen in Fig. (4.3f).

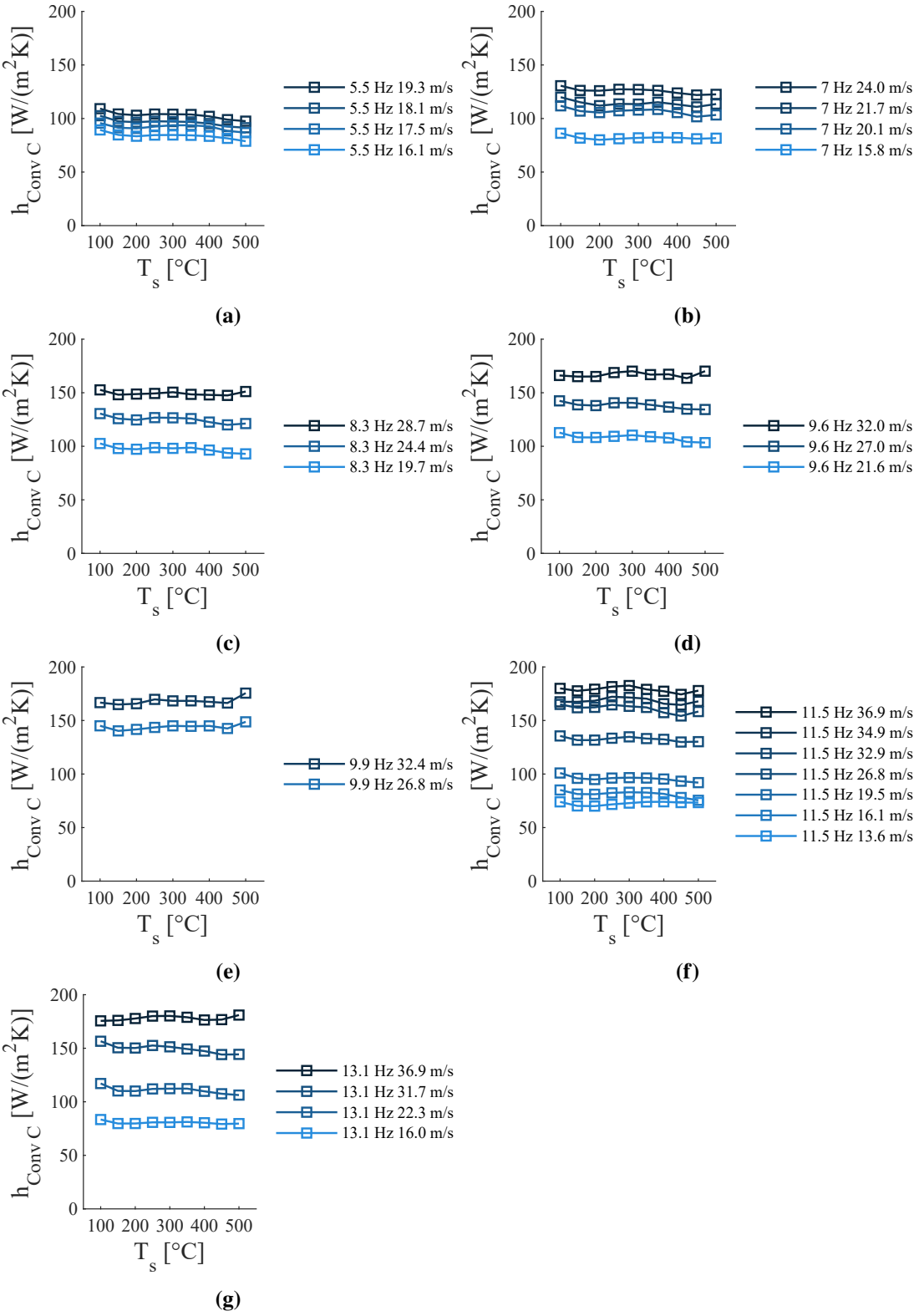

Figure 4.3.: Corrected convective heat transfer coefficient $h_{Corr\,Conv}$ at different steel plate temperatures T_s and varying corrected particle velocities $\hat{u}_{ch}$ at **(a)** $f = 5.5\ Hz$, **(b)** $f = 7\ Hz$, **(c)** $f = 8.3\ Hz$, **(d)** $f = 9.6\ Hz$, **(e)** $f = 9.9\ Hz$, **(f)** $f = 11.5\ Hz$ and **(g)** $f = 13.1\ Hz$

4.2. Heat transfer coefficient as $g(\hat{u}_{ch},\ f)$

The figures featured in this section of the result can be found in full size in appendix B.

4.2.1. Heat transfer coefficient as a function of corrected particle velocity

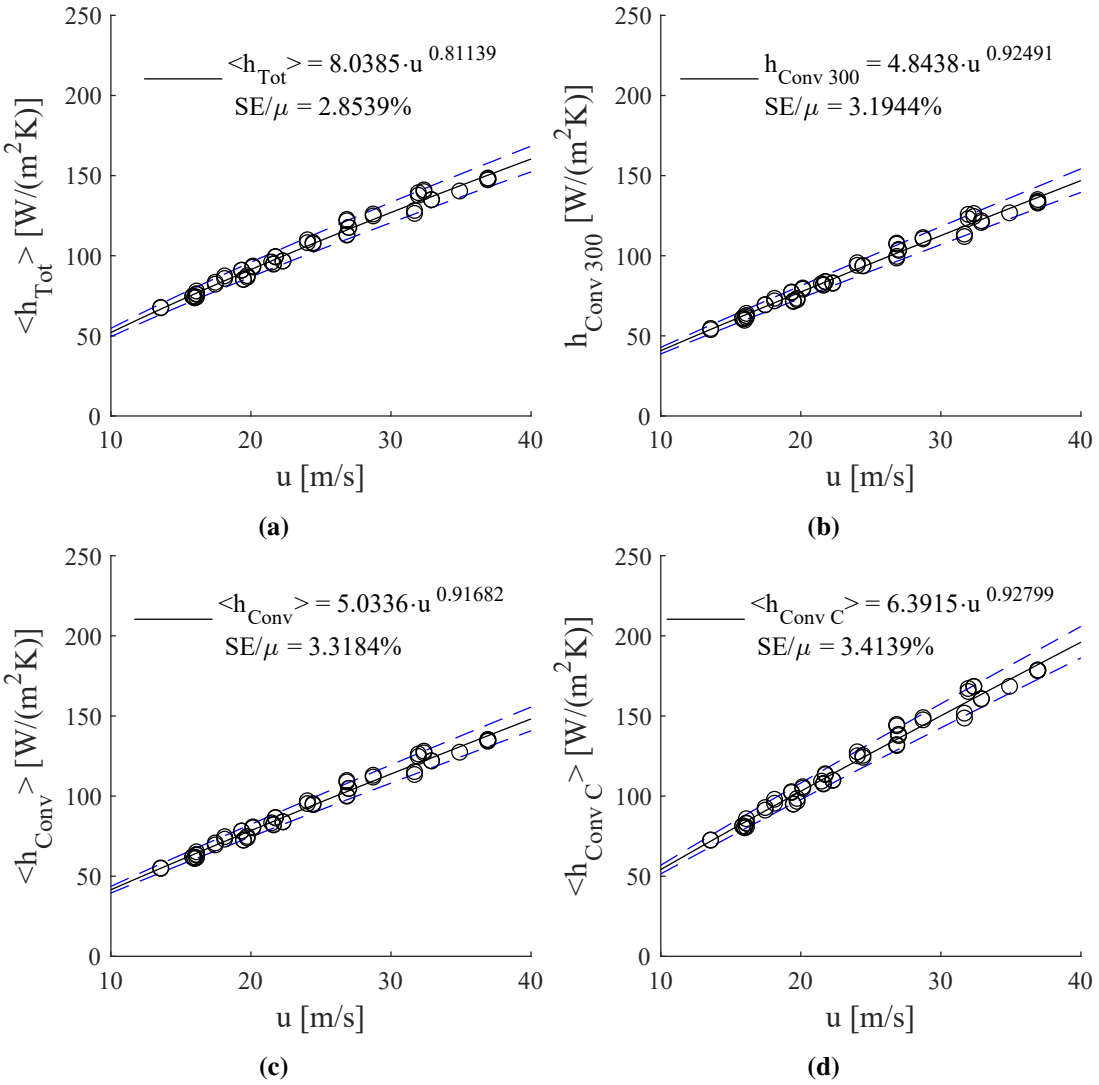

Figure 4.4.: The four calculated heat transfer coefficients with varying f and $\hat{u}_{ch}$ as one-term power series of $\hat{u}_{ch}$:
(a) $\langle h_{Tot} \rangle$, **(b)** $h_{Conv\,300}$, **(c)** $\langle h_{Conv} \rangle$ and **(d)** $\langle h_{Conv\,C} \rangle$

The four cases show the points clustering along the fitted one-term power series, see Fig. (4.4).

The one-term power series representing $\langle h_{Tot} \rangle$ as a function of corrected particle velocity shows good agreement to the data when the influence of frequency is neglected, see Fig. (4.4a). All data points are within the ±5% bounds of the curve and the normalized standard error is at 2.85%. In the tested range of frequencies and $\hat{u}_{ch}$, $\langle h_{Tot} \rangle$ depends almost linearly on $\hat{u}_{ch}$.

The power series fitted to $h_{Conv\,300}$, see Fig. (4.4b), is closer to linear compared to $\langle h_{Tot} \rangle$. However, the normalized standard error is slightly higher at 3.20%. All data points are within the ±5% bounds.

$\langle h_{Conv} \rangle$ behaves similar to $h_{Conv\,300}$, see Fig. (4.4c). The normalized standard error is close to identical at 3.20%.

The mean corrected heat transfer coefficient has a similar fit to $\hat{u}_{ch}$ compared to $h_{Conv\,300}$ and $\langle h_{Conv} \rangle$, see Fig. (4.4d). The normalized standard error is slightly higher at 3.41%

The outlier of the four heat transfer coefficients is $\langle h_{Tot} \rangle$, see Fig. (4.4a), as it shows the least linearity and the highest intercept.

4.2.2. Heat transfer coefficient as a function of frequency

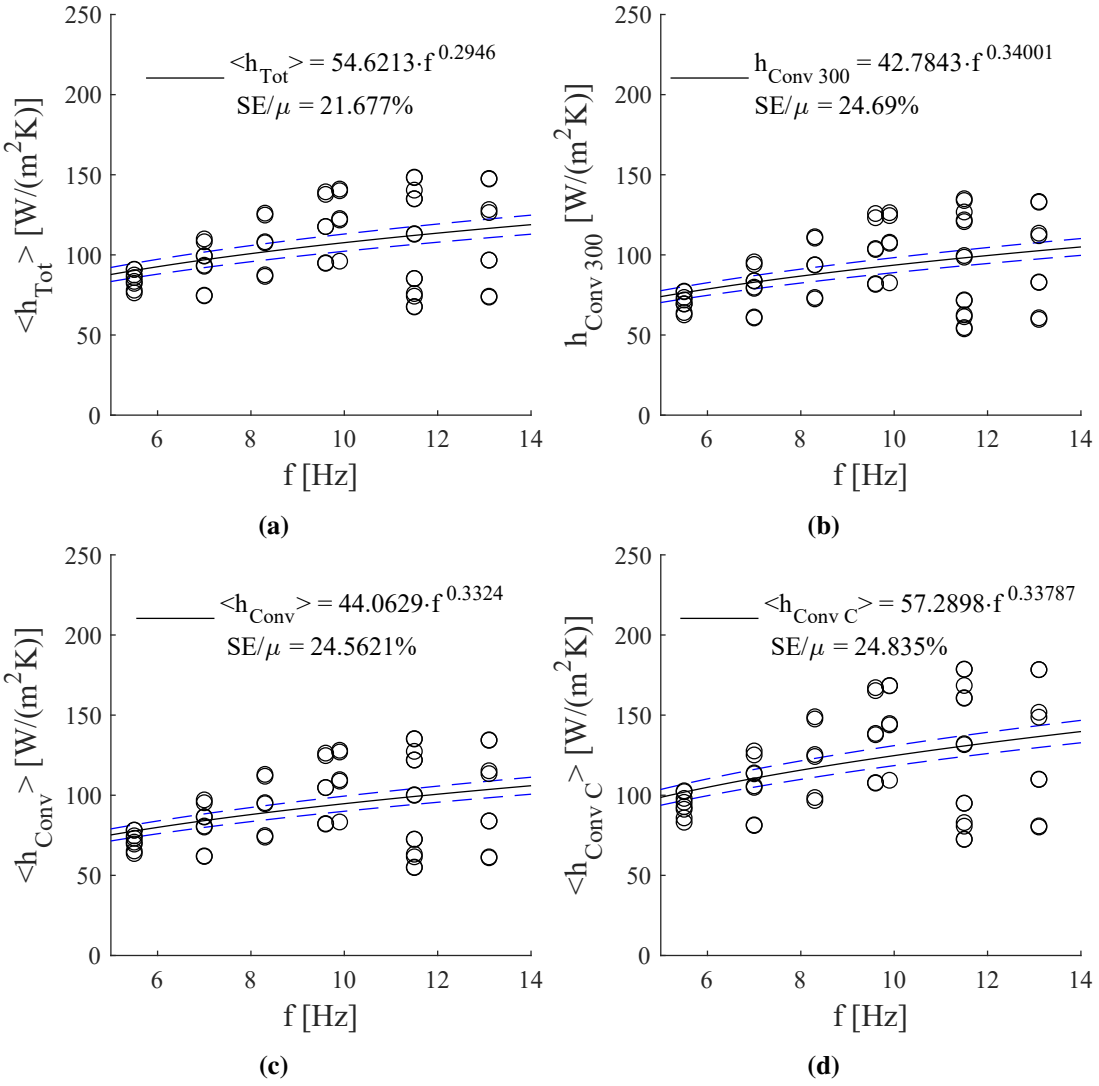

Figure 4.5.: The four calculated heat transfer coefficients with varying f and $\hat{u}_{ch}$ as one-term power series of f:
(a) $\langle h_{Tot} \rangle$, **(b)** $h_{Conv\,300}$, **(c)** $\langle h_{Conv} \rangle$ and **(d)** $\langle h_{Conv\,C} \rangle$

Across all of Fig. (4.5), values of the heat transfer coefficient are scattered. They appear along vertical lines corresponding to the 7 different series of frequencies. The most notable difference among the four cases is the intercept/constant varying from 42.8 to 57.3 as it decides the overall level of the fit. In the 5.5 Hz series they are the least scattered and in the 11.5 Hz series they are the most scattered.

Out of the four one-term power series fitted to the calculated heat transfer coefficients, $\langle h_{Tot} \rangle$ shows the least standard error at 21.7%, see Fig. (4.5a). It also has the lowest exponent.

$h_{Conv\,300}$ has a standard error of 24.7% and has the lowest intercept out of the four at 42.8, see Fig. (4.5b).

$\langle h_{Conv} \rangle$ has a similar standard error to $h_{Conv\,300}$ at 24.6%, see Fig. (4.5c).

$\langle h_{Conv\,C} \rangle$ has the highest standard error at 24.8% as well as the highest intercept at 57.3, see Fig. (4.5d).

The standard error of the fits is large and the frequency is thus predicted to not have a big influence on the heat transfer coefficient.

4.2.3. Heat transfer coefficient as a function of corrected particle velocity and frequency

When adding dependency on frequency to the data fit, the normalized standard error of the points to the fitted surface decreases in all four cases, see Fig. (4.6), indicating a better fit compared to both previous one-term power fits, see Fig. (4.5) and (4.4).

For $\langle h_{Tot} \rangle$, the dependency on $\hat{u}_{ch}$ moves closer to linear and the dependency on frequency is low, see Fig. (4.6a). The normalized standard error is smaller in Fig. (4.6a), at 2.22%, compared to the normalized standard error of the fit in Fig. (4.4a), at 2.85%, indicating a better fit. The dependency on frequency is inverted across all four calculated heat transfer coefficients, see Fig. (4.6a - 4.6d), meaning a lower frequency contributes to a higher heat transfer coefficient.

The dependency on $\hat{u}_{ch}$ is closer to linear for $h_{Conv\,300}$ with added frequency dependency, see Fig. (4.6b). The normalized standard error is 2.46%.

Again, $\langle h_{Conv} \rangle$ and $h_{Conv\,300}$ show similar fits and equal goodness at normalized standard error 2.46%, see Fig. (4.6b) and Fig. (4.6c).

$\langle h_{Conv\,C} \rangle$ in Fig. (4.6d) has a fit similar to $\langle h_{Conv} \rangle$ in Fig. (4.6c). However, the normalized standard error is slightly higher at 2.63%.

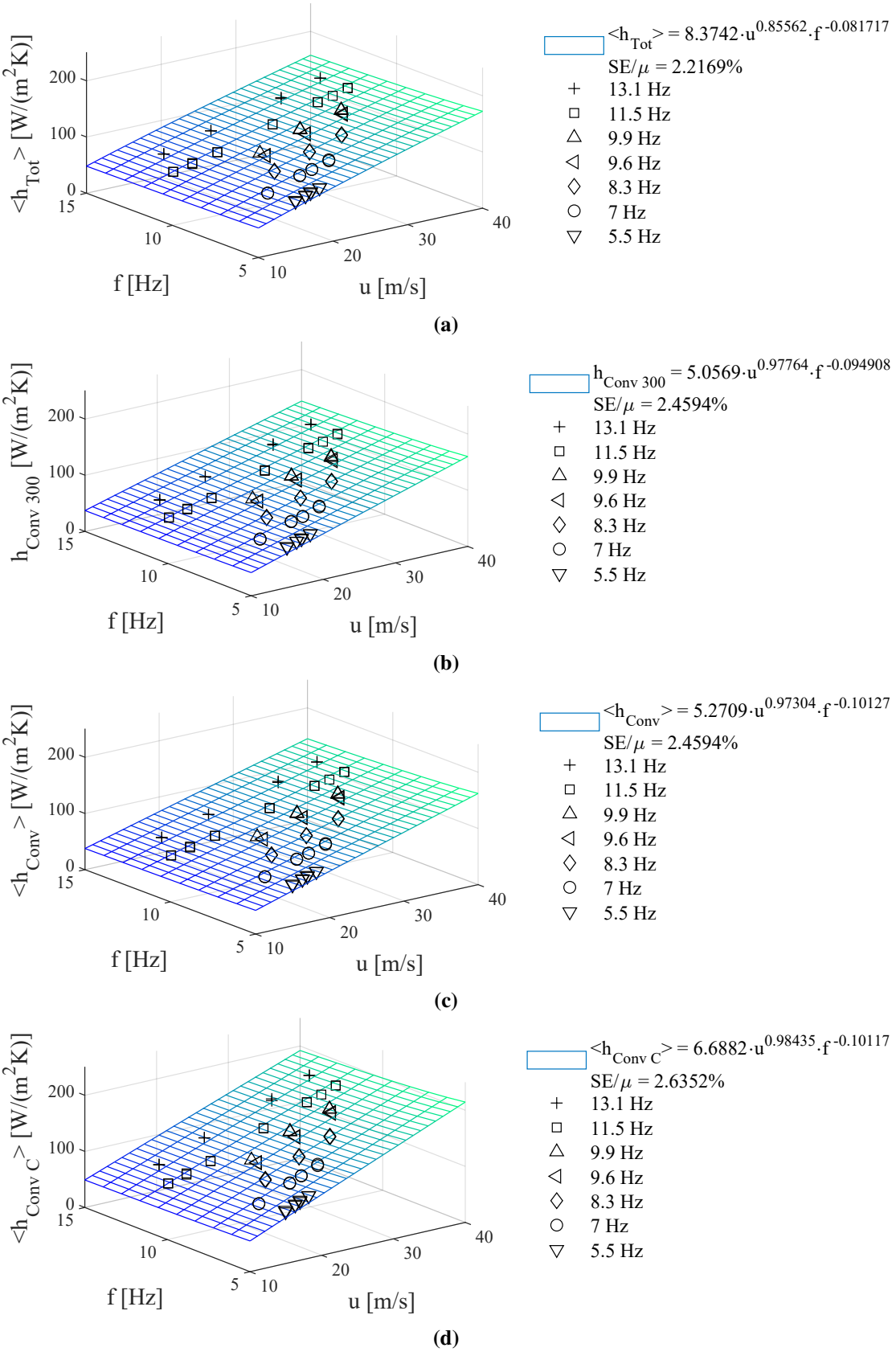

Figure 4.6.: The four calculated heat transfer coefficients as non-linear surfaces with respect to $\hat{u}_{ch}$ and f: **(a)** $\langle h_{Tot} \rangle$, **(b)** $h_{Conv\ 300}$, **(c)** $\langle h_{Conv} \rangle$ and **(d)** $\langle h_{Conv\ C} \rangle$

4.3. Particle velocity as $g(f,\ SL)$

4.3.1. Particle velocity as a function of stroke length

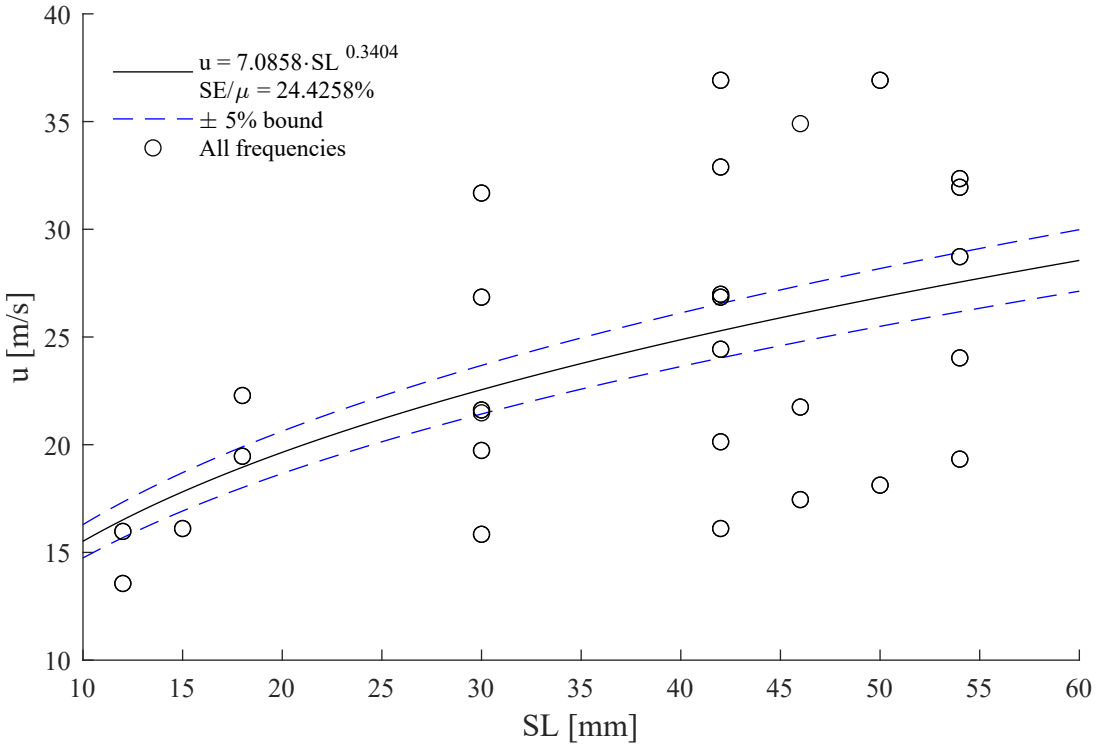

Figure 4.7.: $\hat{u}_{ch}$ as a one-term power series of stroke length with varying f and SL

In Fig. (4.7), the points are positioned on either of the 8 tested stroke lengths in the experiment. The points are scattered along these lines and the fit has a standard error of 24.4%.

4.3.2. Particle velocity as a function of frequency

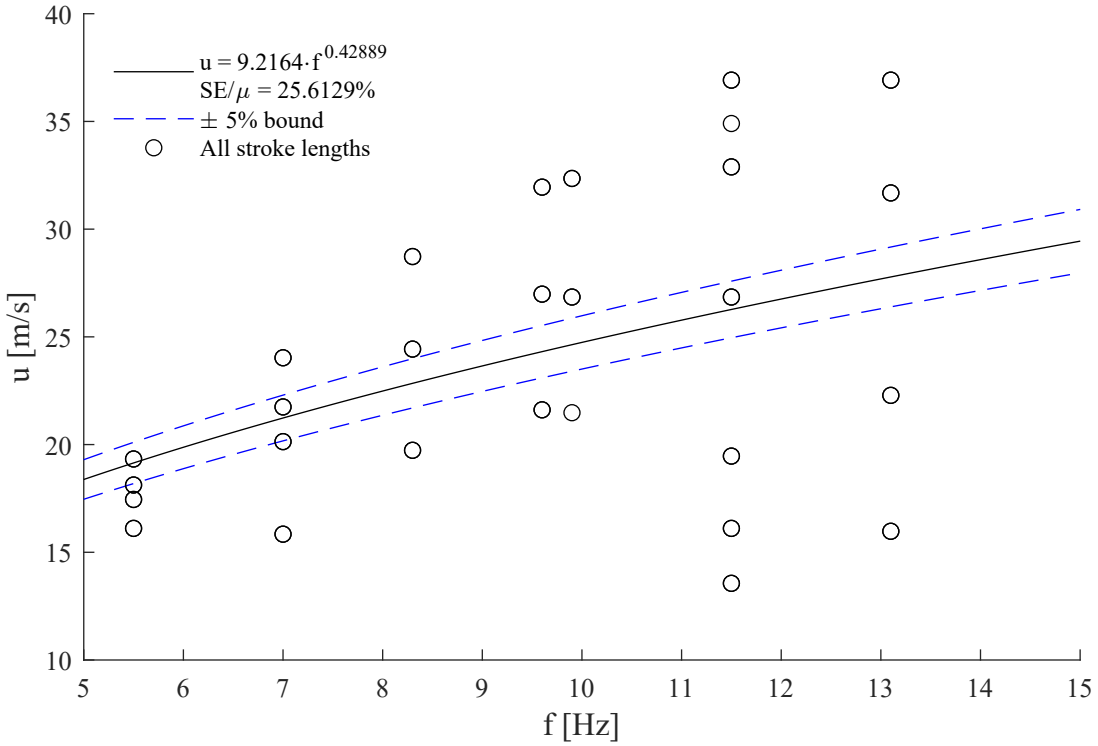

Figure 4.8.: $\hat{u}_{ch}$ as a one-term power series of f with varying f and SL

The points in Fig. (4.8) appear along the 7 different frequencies present in the experiments and show scattering. Points are the most scattered at 11.5 Hz and the least scattered at 5.5 Hz. The standard error of the fit is 25.6%.

4.3.3. Particle velocity as a function of frequency and stroke length

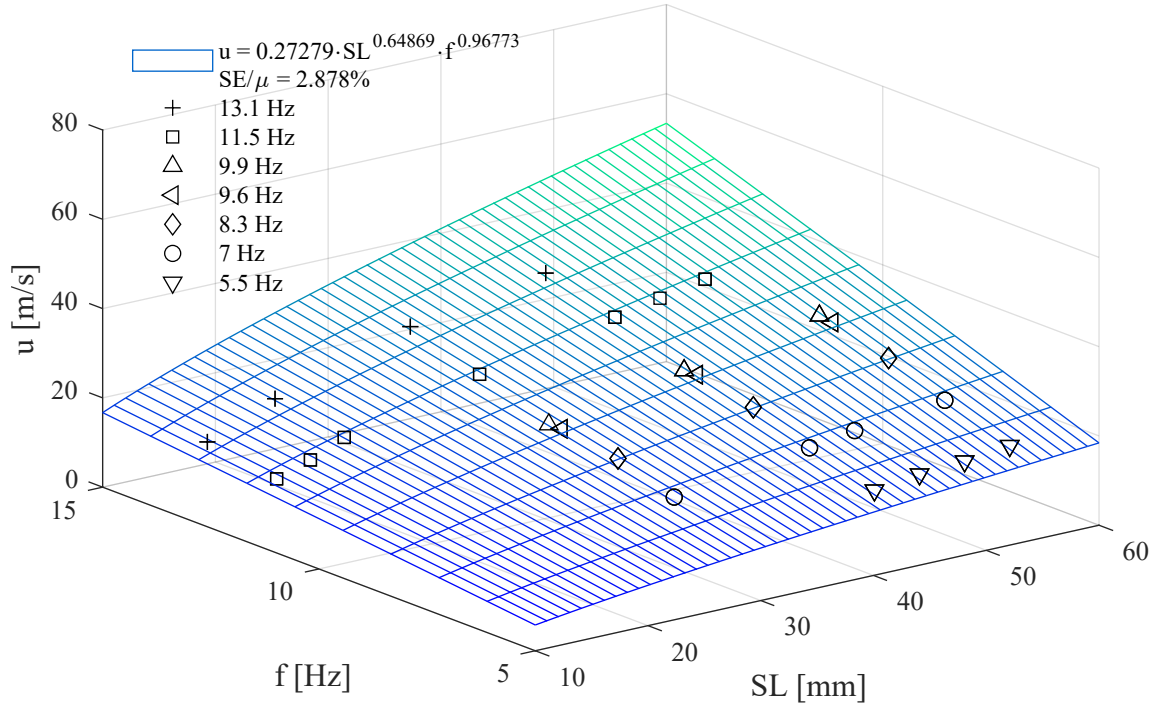

Figure 4.9.: $\hat{u}_{ch}$ as a non-linear surface with respect to f and SL

However, despite high standard errors in the fits in Fig. (4.8) and (4.7), the non-linear surface with respect to f and SL shows a low standard error of 2.9%, see Fig. (4.9). Therefore, the combination of the two parameters f and SL have a high influence on the corrected particle velocity, whereas the two parameters on their own does not. According to the surface fit, $\hat{u}_{ch}$ is almost linearly dependent on f while the exponent of SL is lower.

4.4. The power consumption as $g(f,\ \hat{u}_{ch})$

4.4.1. The power consumption as function of corrected particle velocity

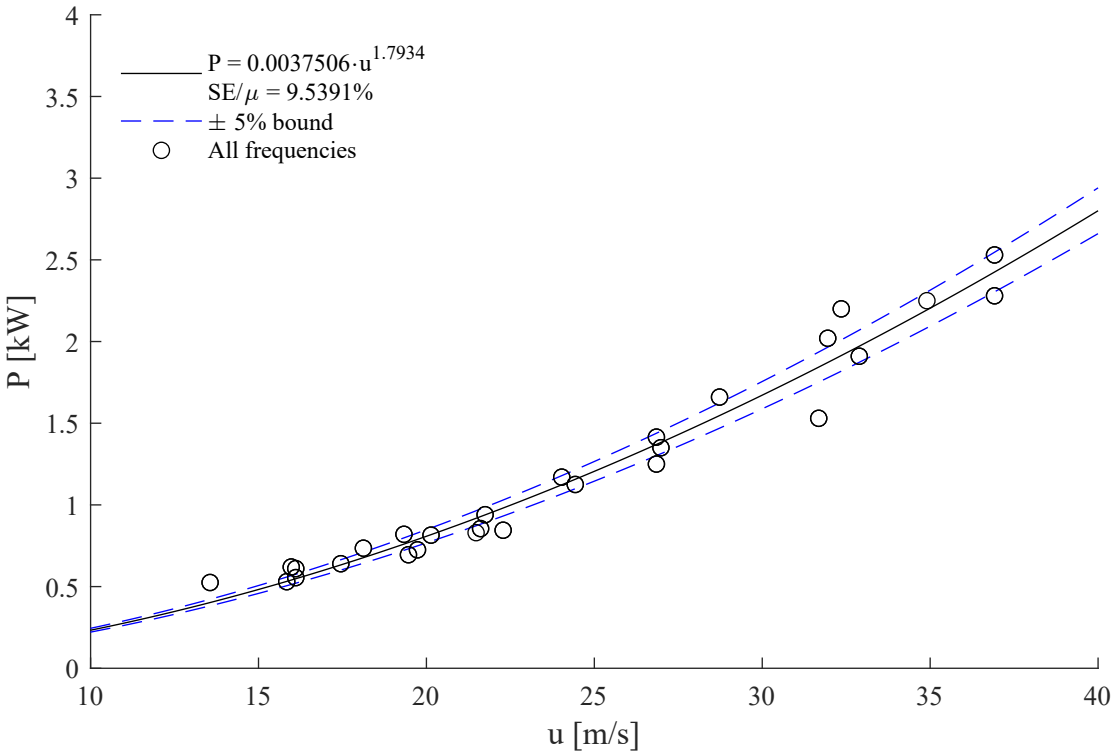

Figure 4.10.: Power consumption as a one-term power series of $\hat{u}_{ch}$

The exponent is above one and the fit is closer to a $2nd$ degree polynomial fit than a linear fit for the power consumption as a function of $\hat{u}_{ch}$, see Fig. (4.10). The normalized standard error is high at 9.5% compared to the fits of heat transfer coefficient to corrected particle velocity in Fig. (4.4).

4.4.2. The power consumption as function of frequency

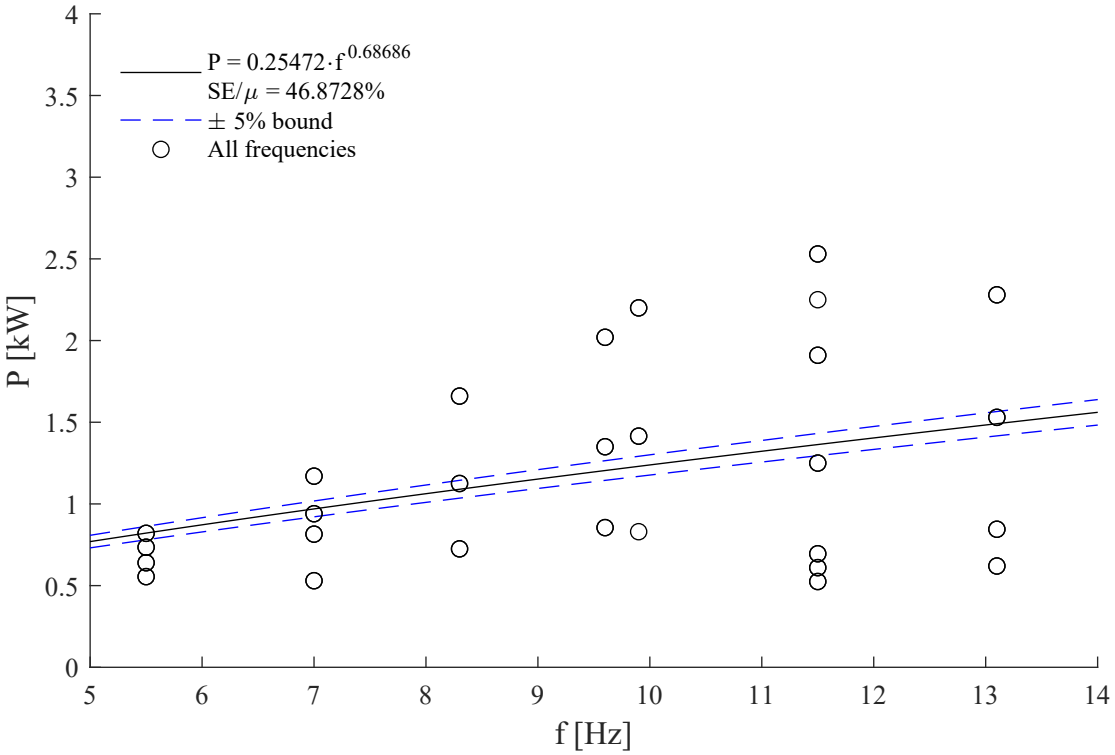

Figure 4.11.: Power consumption as a one-term power series of f

The power measurements are scattered along the 7 frequency lines, see Fig. (4.11). The standard error is the highest observed among all fits at 46.9%. The power consumption shows a better fit to the corrected particle velocity compared to frequency, see Fig. (4.10) and (4.11).

4.4.3. The power consumption as function of frequency and corrected particle velocity

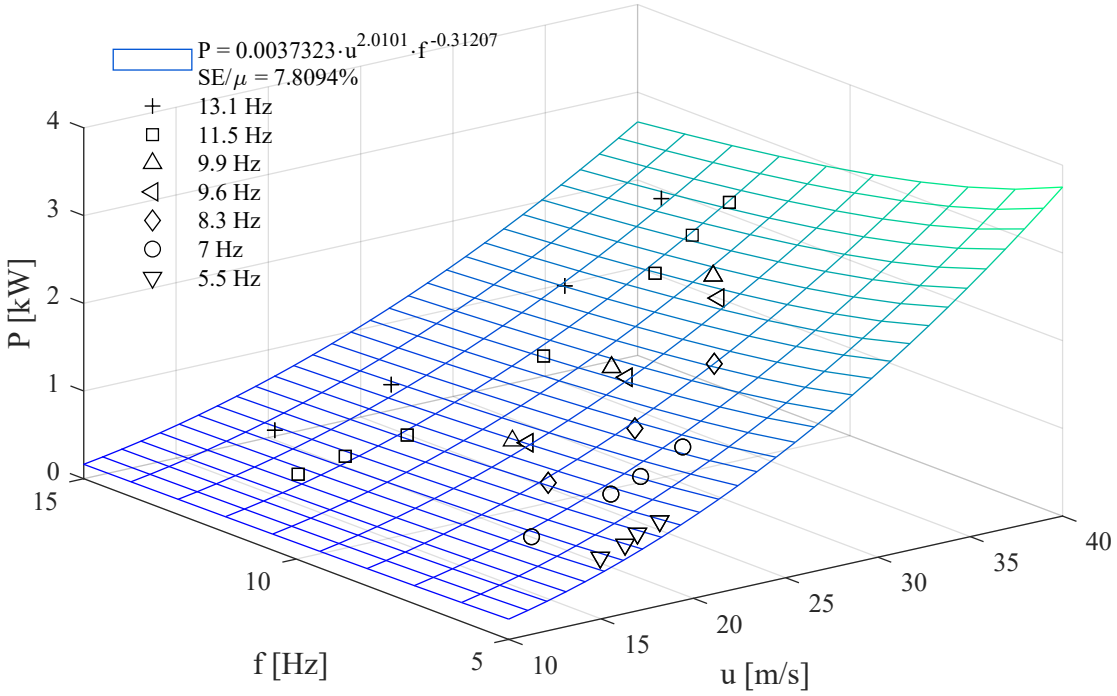

Figure 4.12.: Power consumption as a non-linear surface with respect to $\hat{u}_{ch}$ and f

The fitted surface, see Fig. (4.12) has a slightly lower standard error at 7.8% compared to the one-term power series fit in Fig. (4.10). The surface fit has a high exponent on the corrected particle velocity at 2.0 and a negative but low exponent on frequency at -0.3.

4.5. Comparison of infrasound cooling to natural and forced convection

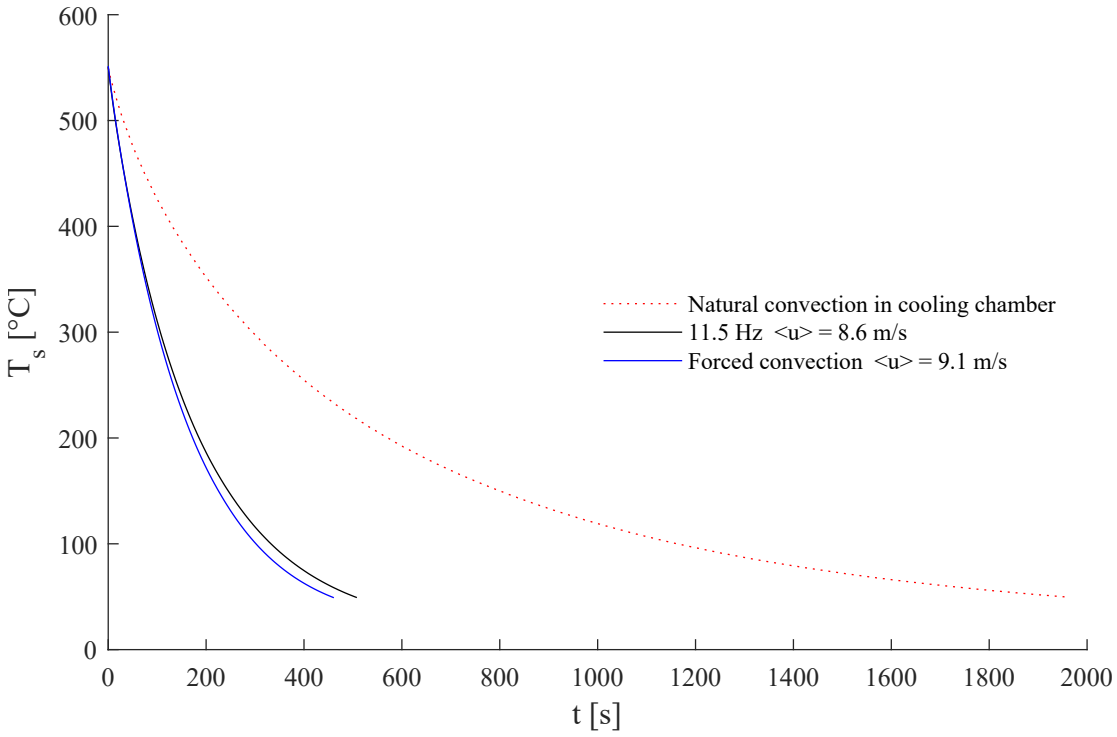

Figure 4.13.: Comparison of the cooling curves of natural convection, forced convection and infrasound cooling

Comparatively, natural convection takes the longest time followed by infrasound cooling at 11.5 Hz with $\langle u \rangle = 8.6\, m/s$ closely followed by forced convection with $\langle u \rangle = 9.1\, m/s$, see Fig. (4.13). According to Tab. (4.1), this is reflected in the four calculated heat transfer coefficients, with shorter cooling times leading to higher heat transfer coefficients.

Table 4.1.: Comparison of heat transfer coefficients

Type	$\langle u_{ch} \rangle$ $[m/s]$	f $[Hz]$	$\langle h_{Tot} \rangle$ $[\frac{W}{m^2K}]$	$h_{Conv\,300}$ $[\frac{W}{m^2K}]$	$\langle h_{Conv} \rangle$ $[\frac{W}{m^2K}]$	$\langle h_{Conv\,C} \rangle$ $[\frac{W}{m^2K}]$
Natural convection	-	-	20.7	8.3	8.2	10.5
Infrasound cooling	8.6	11.5	67.5	53.9	54.9	72.4
Forced convection	9.1	-	73.8	60.4	61.1	80.3

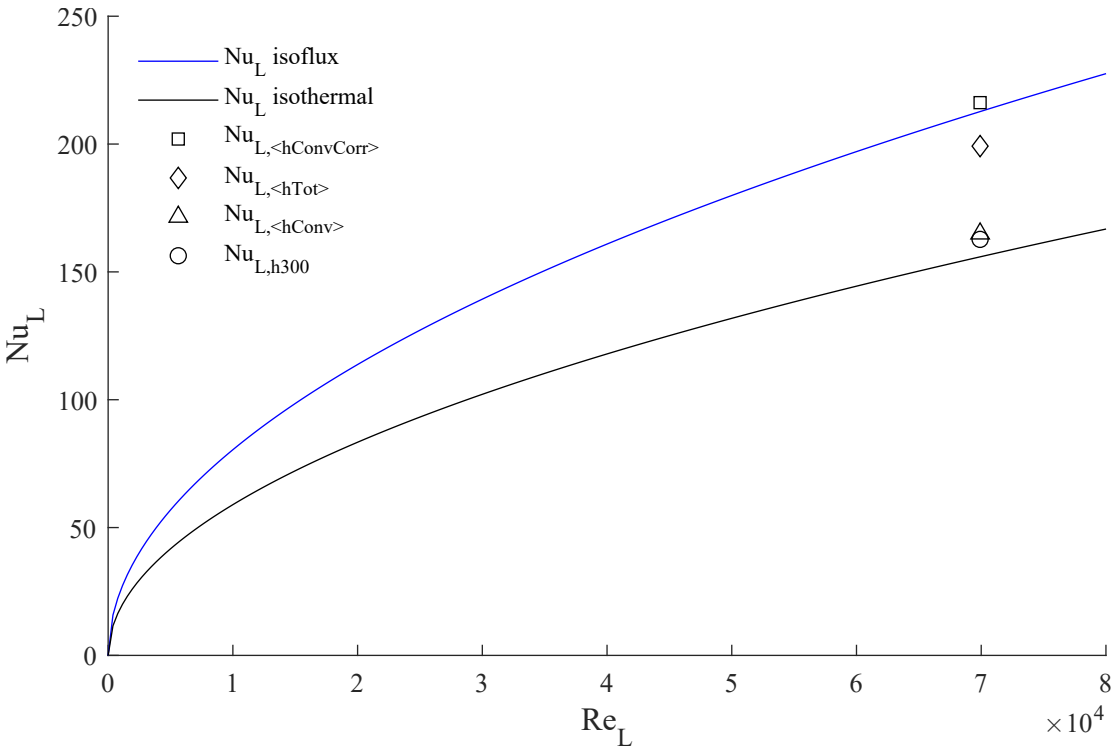

Figure 4.14.: Nusselt number for cooling with forced convection calculated using the four different heat transfer coefficients and compared to two existing empirical relations for mean Nusselt number for laminar flow over a flat plate as a function of the Reynolds number.

In Fig. (4.14), the Nusselt number for the four calculated heat transfer coefficients for the forced convection are shown in relation to two empirical formulas for Nusselt number as a function of Reynolds number. The Nusselt number for $\langle h_{Conv\,C} \rangle$ and $\langle h_{Tot} \rangle$ are closer to the formula for uniform heat flux whereas $h_{Conv\,300}$ and $\langle h_{Conv} \rangle$ are closer to the formula for uniform temperature.

Chapter 5.

Discussion

5.1. Open questions

For me, the experiments have been very interesting and thought provoking. In this section some of my questions will be discussed.

5.1.1. The validity of the lumped system analysis

Because of the tight placement of the K-elements it is not possible to verify if the lumped system analysis is valid or not. According to the Biot number calculation, the steel plate is a lumped body with a big margin to increase the heat transfer coefficient without leaving the lumped body range. However, if the plate was much wider while remaining the same thickness, there might be non-uniform temperature distribution due to uneven heating and cooling. This would affect the validity of the lumped system analysis despite having a low Biot number. If the plate was thicker, the Biot number would rise and potentially nullify the lumped body assumption.

5.1.2. Assumption of plane waves

According to Eq. (2.16), the sound wave in a tube or a pipe can be considered plane if the frequency of the wave is below $f = 100/r$. Using our resonance tubes with radius of 0.0375 m, this frequency is

$$f = \frac{100}{0.00375} = 2667\ Hz$$

Thus, the assumption of the waves being plane is valid.

5.1.3. Transmittance of power as sound wave reaches cooling chamber

Eq. (2.19) states only a part of the power will be transmitted when the cross sectional area of the tube changes. This could be the case when sound wave travels from the resonance tubes to the cooling chamber. The cross sectional area of the resonance tubes is $S_1 = 4418\,mm^2$ and the cross sectional area of the cooling chamber is $S_2 = 8066\,mm^2$. This gives a transmittance coefficient of acoustic power of

$$T_\Pi = \frac{4S_1S_2}{(S_1 + S_2)^2} = \frac{4 \cdot 4418 \cdot 8066}{(4418 + 8066)^2} = 0.91$$

meaning 9% of the power is lost through the passage.

5.1.4. Correlation between stroke length and frequency of the pulsator

When taking the measurements of frequency and peak to peak voltage from the oscilloscope, the accuracy was very low as the values would constantly change. It was therefore thought small variation in frequency between tries from the same frequency series were random. However, upon closer inspection it turned out there was a small correlation between the highest frequency in the series and the highest stroke length. Not every series displayed this. However, this could be because of random error.

The effect was small and I therefore assumed it to not be of great importance to the results. As a consequence, all tries in the same series were assumed to have the same frequency. Due to technical limitations this could not be further investigated. A solution could have been if we had an oscilloscope with the ability to log measurements over time and provide an average over the entire measurement. The method for getting the oscilloscope measurements relied too heavily on the skill of the person taking the measurements, meaning me. The contrast to this would be the logging of temperature measurements as this process did not rely on any particular skill except clicking a button to initiate the logging.

5.1.5. The importance of frequency

Although this thesis did not find the heat transfer coefficient had a significant dependency on frequency, this may not be true in other cases. The test plate is very small compared to the wavelength of the infrasound and a simple dimensional analysis can shed some light on this. When comparing the timescale of the flow

$$t_{flow} = \frac{L}{\hat{u}_{ch}} \tag{5.1}$$

where L is the width of the plate with unit m, to the timescale of the infrasound

$$t_{infrasound} = \frac{1}{f} \tag{5.2}$$

it becomes apparent they operate on a different scale, see Tab. (5.1).

Table 5.1.: Comparison of t_{flow} and $t_{infrasound}$

$f\ [Hz]$	$L\ [m]$	$\hat{u}_{ch}\ [m/s]$	$t_{flow}\ [s]$	$t_{infrasound}\ [s]$	$t_{flow}/t_{infrasound}$
5.5	0.12	19.3	0.0062	0.18	0.034
5.5	0.12	16.1	0.0075	0.18	0.042
9.6	0.12	32.0	0.0038	0.10	0.036
9.6	0.12	21.6	0.0056	0.10	0.053
11.5	0.12	36.9	0.0033	0.087	0.037
11.5	0.12	13.6	0.0088	0.087	0.10
13.1	0.12	36.9	0.0033	0.076	0.043
13.1	0.12	16.0	0.0075	0.076	0.10
113.6	0.12	16.0	0.0088	0.0088	1
10.0	2.0	20	0.10	0.10	1

In the last two rows of Tab. (5.1) there are two examples of how equal t_{flow} and $t_{infrasound}$ could be achieved. The later example is more relevant to the topic since it is within the infrasound realm. Also, this is close to the expected industrial application of SSAB as plate widths of up to 3 m is common. While on the subject of reality, as the frequency approaches zero, the resonance tube length needed increases very fast. This both takes up space and could make the system prone to attenuation, as attenuation increases with distance from the sound source. Another potential problem is the decrease in particle velocity amplitude when the stroke length is kept constant and the frequency decreases. This implies a considerable increase in stroke length is required to achieve a high heat transfer coefficient at lower frequencies. This is because a high particle velocity amplitude is necessary to achieve a high heat transfer coefficient.

5.1.6. Skewed result when looking at $h = g(f)$ due to limited sound pressure in the lower frequencies

When looking at Fig. (4.5), (4.8) and (4.11), all depicting a parameter as function of f, it becomes apparent the values of said parameter are very scattered. It is also evident the fit of the one-term power series is poor. When solely looking at, for example, Fig. (4.5), it could be easy to be tricked into believing there is a trend in how the heat transfer coefficients increase with increasing frequency. However, this is a problem built into the experiment as the limited selection of stroke lengths meant the lower frequencies would not be able to produce particle velocities near the highest possible in the higher frequencies. In Fig. (4.9), it is shown how $\hat{u}_{ch}$ depends heavily on the combination of frequency and stroke length, meaning there is a limit on the maximum $\hat{u}_{ch}$ achievable for a certain frequency with a fixed maximum stroke length.

Because of time constraints, it was deemed unfeasible to test all stroke lengths at all different frequencies. This practice was limited to the frequency 11.5 Hz and even here it was not possible to use the 54 mm stroke length as the sound pressure became too high and the sound wave broke down. When choosing stroke lengths, the emphasis was put on getting overlapping $\hat{u}_{ch}$ between one frequency and the next. This meant the three shortest stroke lengths were only tested on the two highest frequencies and the longest stroke length only on the five lowest frequencies. Coming back to Fig. (4.5), (4.8) and (4.11), if the emphasis was put on getting a wide range of $\hat{u}_{ch}$ for each frequency and the stroke lengths were more variable and the time available was infinite, I think the curve would be linear with no slope and an intercept at the mean value of the data set. What I mean is, these figures have an air of implying the parameter in focus changes a lot depending on the frequency. The same can be said about Fig. (4.7), but for the influence of stroke length alone on $\hat{u}_{ch}$. However, I think this is an illusion stemming from the limit in available stroke lengths and thus a limit in available $\hat{u}_{ch}$.

In the case where frequency was combined with $\hat{u}_{ch}$ as in Fig. (4.6) and (4.12) the relative standard error decreased roughly 20% in both cases (compared to the fit using only $\hat{u}_{ch}$), stating frequency has an effect, although ever small on this scale. However, in Fig. (4.4), the standard error using only $\hat{u}_{ch}$ was already in the acceptable region below 5%. In the case where frequency was combined with stroke length the influence of the combination of both parameters was much more prominent and the relative standard error decrease was 88%. This lowered the standard error from roughly 25%, looking at single parameters, to 2.9%, when combining them.

5.1.7. On forced convection

From Fig. (4.13) and Tab. (4.1), it might seem like a good idea to use forced convection instead of infrasound cooling as it is suggested forced convection has a higher rate of cooling compared to infrasound at a similar mean flow. The difference in consumed

power also confirms this belief as the fan running at its maximum power required 0.26 kW, whereas the pulsator required 0.53 kW for this particular case. While these two facts are undeniable, they are perhaps only valid for this very experiment. One of the benefits of using infrasound cooling, compared to fan cooling from one side, is the uniform heat transfer across the whole plate width. A fan blowing from one side will cool a wide plate unevenly and risk jeopardizing its material properties. It should also be noted the potential to increase the heat transfer rate further was limited when using the fan, as it was already running at maximum velocity. The infrasound cooling on the other hand could at least double the velocity by increasing the stroke length, translating roughly to a doubling of the heat transfer coefficient.

5.1.8. The uncertainty of constant emissivity

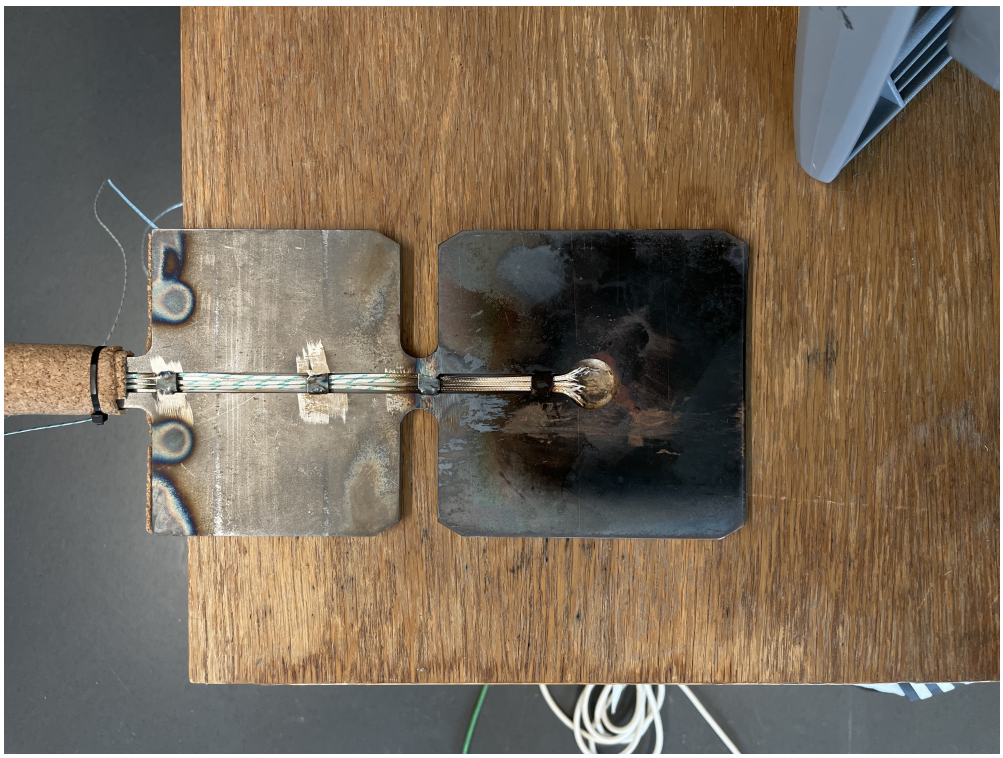

Figure 5.1.: The oxidized top side of the test plate

According to [6], the emissivity of stainless steel is related to surface temperature in the range 750 - 1150 K, with higher temperatures leading to higher emissivity. As our plate temperature went up to 870 K during heating, this might have affected the emissivity of our test plate. Another phenomenon noted is the effect of heating time on the emissivity, with sample seeing a drastic increase in emissivity after 3 hours of heating at a constant temperature of 900 K. After the 3 hours, the emissivity remained constant and this was accredited to the oxidization of the plate being completed [6]. Again, this might

have occurred in our experiments. The top side of our test plate developed a large black oxidized spot as the experiments progressed, suggesting this part could have an increased emissivity compared to being unoxidized, see Fig. (5.1). Unfortunately I did not note when this change took place but I know it was not in the first half of the experiments. The underside of the test plate did not show a notable visual change, see Fig. (5.2).

However, for this experiment, a constant emissivity was still chosen as it would involve a lot of uncertainty to choose a variable emissivity. The temperature range in this experiment is not the most affected by radiative heat transfer and the emissivity should therefore not play a major role in the heat transfer.

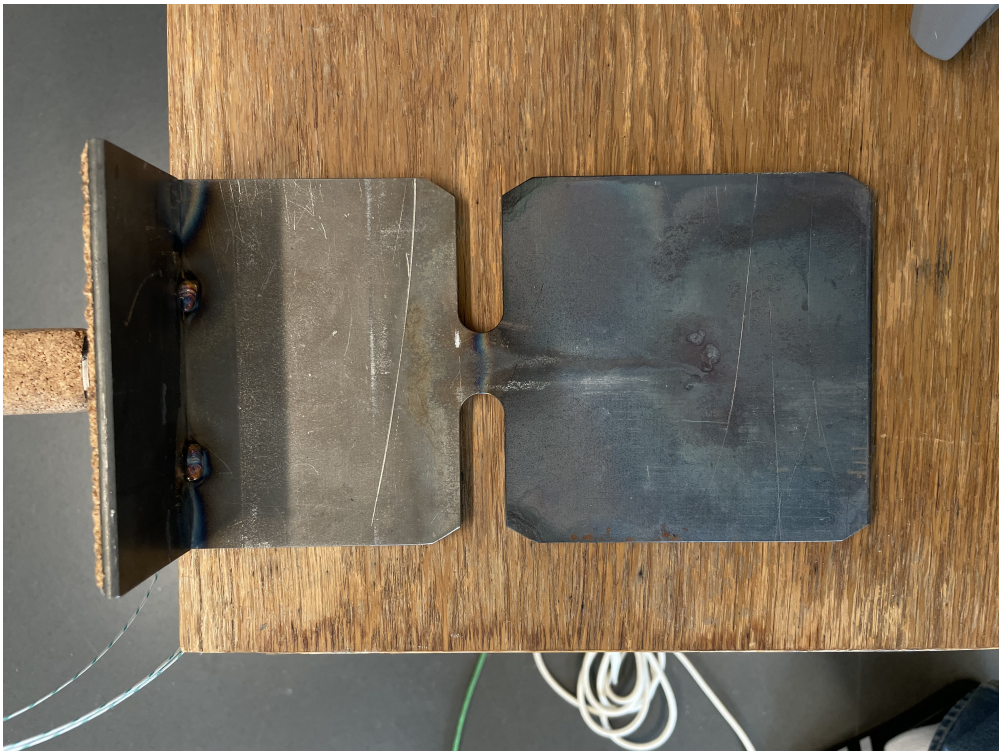

Figure 5.2.: The unoxidized underside of the test plate

5.2. Ideas for further research

From doing the experiments and seeing the results I have come up with a few recommendations for future research and some improvements to my research.

5.2.1. Particle image velocimetry measurements (PIV)

Before beginning the experiments, I immediately got interested by the flow in the cooling chamber. Especially since I had completed several courses on the topic of computational fluid dynamics. Flow plays a big role in heat transfer and by adjusting flow characteristics as well as geometry, the heat transfer can be influenced a lot. Through discussion, many have pointed out there is no flow in a closed system like this and I suppose they are right. However, there is certainly movement of air inside the chamber and through some leakage you can feel pulses of air escaping the chamber. In my mind, I envisioned a pulse going one way then suddenly being met by another pulse going the opposite way would lead to chaotic flow and turbulence.

To improve the understanding of the whole phenomenon, I would advice carrying out non intrusive PIV measurements on the cooling chamber. On the backside of the chamber is an opening. During our test, this opening was sealed with a sheet of steel and tape to prevent leakage. When performing the PIV measurements, the sheet of steel could be swapped for acrylic glass for visibility.

5.2.2. Computational fluid dynamics simulations (CFD)

Another interesting aspect would be to develop a methodology for infrasound cooling in for example OpenFOAM. Initially, I had wanted to do something similar within the scope of this master thesis as CFD is my background. Unfortunately, I understood quickly it would not be enough time for both experiments and simulations. The idea of simulating the flow in the chamber is still very interesting to me and I think future research should also include simulations. However, if CFD studies has taught me anything it is:

"A simulation is worth nothing without validation."

Christer Fureby

I believe the quote speaks for itself.

5.2.3. Automating the oscilloscope data collection

There was some inaccuracy in the measuring of voltage and frequency using the oscilloscope. Both the voltage and the frequency would oscillate and rarely stay constant. Probably this was what the pressure sensor picked up and relayed to the oscilloscope. Nevertheless, if there was a possibility to log the readings over time to then take the average, it would would have been the best. The data capturing method used in the experiments was subpar and would greatly benefit from the automation of the oscilloscope measurements. This would eliminate the human error and potential bias when selecting frames to capture.

5.2.4. Water cooling both the top and the bottom of cooling chamber

As previously mentioned, we only had water cooling on the top side of the cooling chamber. This was mostly due to time constraints and our eagerness to get going with the experiments. We did not have a T-junction to split the flow or another tap to run separate cooling hoses. When we had already performed the majority of the experiments this way, somebody pointed out we could have connected the cooling water in series to the top and bottom sides in series. I thought this was a very clever solution but I did not want to change the setup now, since it would mean risking the comparability between the measurements. Still, if there would be another project using this cooling chamber, I would suggest running cooling on both sides, either in series or parallel. Maybe counter flow for symmetry?

5.2.5. More tests with forced convection

It would be very interesting to conduct more experiments using a fan with higher velocity to see how forced convection compares to infrasound cooling. These experiments could then also be used to extend the validation of the Nusselt number against the empirical formulas seen in Fig. (4.14). If a wider plate was used, it would also be interesting to see how much difference there is in the uniformity of the cooling between infrasound cooling and forced convection.

5.2.6. Use heater to control the heat flux from the steel plate

Convection across a flat plate is very sensitive to boundary conditions in laminar flow. The choice is mainly between a constant heat flux or a constant wall temperature. To ensure the validity of the measured heat transfer coefficient it would be interesting to study the cooling in the chamber using a heater to provide a constant heat flux

boundary condition. This would give accurate measurements in line with the norms and standards in the heat transfer field and comparison would be easier. In our experiments, forced convection produced heat transfer coefficients in between the two main boundary conditions, see Fig. (4.14).

5.2.7. Is infrasound unique?

While I undoubtedly have seen infrasound cooling at work throughout my experiments, I cannot help but wonder if there are other methods of achieving the same benefits. In comparison with forced convection, the main benefit of infrasound is the uniform cooling across the steel plate. What if a conveyor belt with fans placed in a staggered manner, see Fig. (5.3), could improve uniformity of cooling the same way infrasound does? The steel plate will move on a conveyor belt through the staggered blowers and will thus experience varying direction of the flow as it traverses.

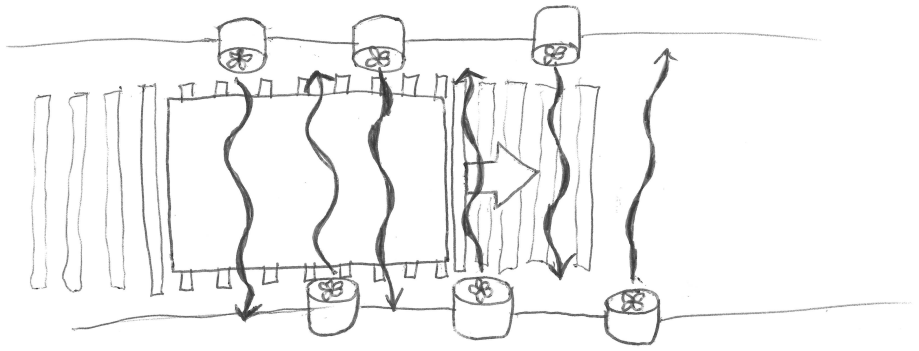

Figure 5.3.: Concept sketch of steel plate cooling using staggered fans along a conveyor belt to achieve cooling uniformity

Another idea is to construct a fan with a T-junction valve alternating the flow direction into the cooling chamber as in Fig. (5.4). The alternating frequency of the valve could be adjusted to match the frequency of infrasound. Then, what is infrasound?

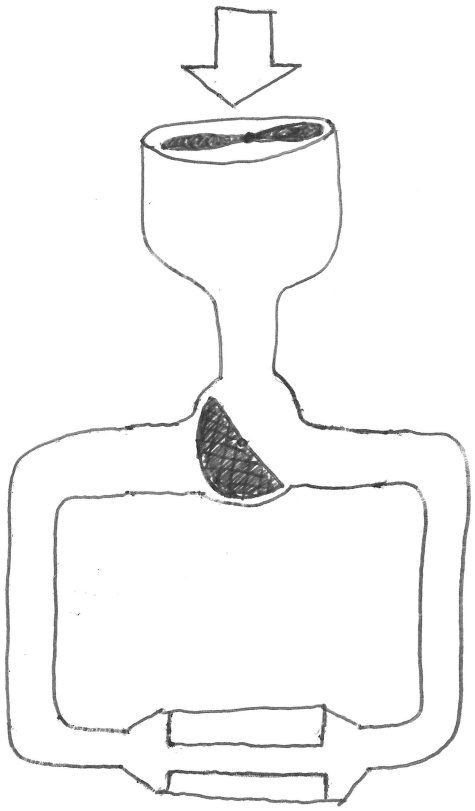

Figure 5.4.: Concept sketch of an alternative way to achieve alternating flow in the cooling chamber using a fan and an alternating T-junction valve

Chapter 6.

Conclusion

In a field with few published articles, this thesis will hopefully spark an interest for the infrasound cooling technique among both industry and academia as well as provide some knowledge in the field.

The results obtained in the experiments have shown the heat transfer coefficient largely depends on the sound pressure level and thus the particle velocity in the cooling chamber. At this scale of steel plate and within the measured interval of frequencies, it is probable forced convection and infrasound cooling have similar heat transfer coefficients. Although, not enough measurements of forced convection were conducted to verify this. When cooling the plate with infrasound, the general trend for the convective heat transfer coefficient was to increase with decreasing plate temperature. Theoretically, this was not expected and a correction from [7] was applied, making the convective heat transfer coefficient more independent of plate temperature. The reason for the unexpected behavior was believed to be changes in the temperature dependent properties of air in the film layer closest to the plate.

When combining the influence of particle velocity and frequency on the heat transfer coefficient, the heat transfer coefficient was slightly inversely proportional to frequency with exponent close to -0.1, see Fig. (4.6). No optimal frequency was found. Rather, the lower the better according to the fitted surface. However, as it was also shown the particle velocity depended heavily on frequency, see Fig. (4.9), the stroke length would need to be excessive to achieve a combination of high particle velocity and low frequency. Another factor is the consumed power. It also has a negative exponent of -0.3 on frequency, see Fig. (4.12), suggesting the motor is slightly more efficient at higher frequencies. The particle velocity still has the dominant influence on the required power and thus energy can be saved by not using too high particle velocities in combination with a higher frequency.

It must be noted however, the frequency may have a bigger influence on the heat transfer coefficient if the plate is wider like in a real steel mill with plates up to 3 m wide.

The required power increases with an exponent of 2.0 while $\langle h_{Conv} \rangle$ only increases with an exponent of 1.0, both with respect to $\hat{u}_c h$, see Eq. (6.2) and (6.3). Thus, the particle

velocity should be kept lower to keep the unit heat transfer coefficient per unit required power from getting too low. The heat transfer coefficient and the consumed power can be compared in some adapted form of the thermal efficiency equation. The general form of thermal efficiency is

$$\eta_{th} = \frac{Benefit}{Cost} \tag{6.1}$$

Normally, benefit and cost have the same unit. If the constraint to have the same unit is removed, $\langle h_{Conv} \rangle$ can be the benefit and P can be the cost. From Fig. (4.6) and (4.12) the equations for $\langle h_{Conv} \rangle$ and P are taken.

$$\langle h_{Conv} \rangle = 5.27 \cdot \hat{u}_{ch}^{0.97} \cdot f^{-0.10} \quad [W/(m^2K)] \tag{6.2}$$

$$P = 3.73 \cdot \hat{u}_{ch}^{2.01} \cdot f^{-0.31} \quad [kW] \tag{6.3}$$

Combining Eq. (6.2) and (6.3) gives

$$\frac{\langle h_{Conv} \rangle}{P} = \frac{5.27 \cdot \hat{u}_{ch}^{0.97} \cdot f^{-0.10}}{3.73 \cdot \hat{u}_{ch}^{2.01} \cdot f^{-0.31}} = 1.41 \cdot \hat{u}_{ch}^{-1.04} \cdot f^{-0.41} \tag{6.4}$$

From Eq. (6.4) it is clear both the $\hat{u}_{ch}$ and f must be kept low to keep the efficiency high. The dominant parameter is still $\hat{u}_{ch}$.

Another perspective is to substitute $\hat{u}_{ch}$ in Eq. (6.2) and (6.3) with the empirical formula from Fig. (4.9)

$$\hat{u}_{ch} = 0.27 \cdot SL^{0.65} \cdot f^{0.97} \quad [m/s] \tag{6.5}$$

This gives

$$\langle h_{Conv} \rangle = 5.27 \cdot (0.27 \cdot SL^{0.65} \cdot f^{0.97})^{0.97} \cdot f^{-0.10} = 1.48 \cdot SL^{0.63} \cdot f^{0.86} \tag{6.6}$$

$$P = 3.73 \cdot (0.27 \cdot SL^{0.65} \cdot f^{0.97})^{2.01} \cdot f^{-0.31} = 0.27 \cdot SL^{1.31} \cdot f^{1.64} \tag{6.7}$$

And further,

$$\frac{\langle h_{Conv} \rangle}{P} = \frac{5.27 \cdot (0.27 \cdot SL^{0.65} \cdot f^{\,0.97})^{0.97} \cdot f^{\,-0.10}}{3.73 \cdot (0.27 \cdot SL^{0.65} \cdot f^{\,0.97})^{2.01} \cdot f^{\,-0.31}} = 5.51 \cdot SL^{\,-0.68} \cdot f^{\,-0.80} \quad (6.8)$$

Again, SL and f must be minimized to get higher efficiency. From this perspective f is the dominant parameter. This is because $\hat{u}_{ch}$ is dependent on SL and f where f is the dominant parameter, see Eq. (6.5).

Keep in mind, these calculations are all empirical formulas based on the experiments and are case specific. The reasoning surrounding the thermal efficiency is **not** generalizable and should be viewed only in the context of this master thesis.

Bibliography

[1] L. L. Beranek, *Acoustics*. McGraw-Hill Book Company, 1954.

[2] Y. Çengel, *Heat transfer: a practical approach*, 2nd ed. McGraw-Hill Higher Education, 2002.

[3] L. E. Kinsler, A. R. Frey, A. B. Coppens and J. V. Sanders, *Fundamentals of acoustics*, 4th ed. Wiley, 2000.

[4] S. G. Lee, M. Kaviany and J. Lee, "Role of quenching method on cooling rate and microstructure of steels: Variations in coolant and its flow arrangement", *International Journal of Heat and Mass Transfer*, vol. 189, pp. 122–702, 2022.

[5] G. Leventhall, "What is infrasound?", *Progress in Biophysics and Molecular Biology*, vol. 93, no. 1, pp. 130–137, 2007.

[6] Y. Liu, Z. Hu, D. Shi and K Yu, "Experimental investigation of emissivity of steel", *International Journal of Thermophysics*, vol. 34, pp. 496–506, 2013.

[7] B. S. Petukhov, "Heat transfer and friction in turbulent pipe flow with variable physical properties", in *Advances in heat transfer*, vol. 6, Elsevier, 1970, pp. 503–564.

[8] J. Preston and W. Johnson, "Acoustic enhancement of the rate of heat transfer over a flat plate-an experimental investigation", 1997.

[9] B. Sundén, *Introduction to heat transfer*. WIT Press, 2012.

[10] B. G. Woods, "Sonically enhanced heat transfer from a cylinder in cross flow and its impact on process power consumption", *International journal of heat and mass transfer*, vol. 35, no. 10, pp. 2367–2376, 1992.

Appendix A.

Full size images of h as a function of T_s

A.1. h_{Tot} as $g(T_s)$

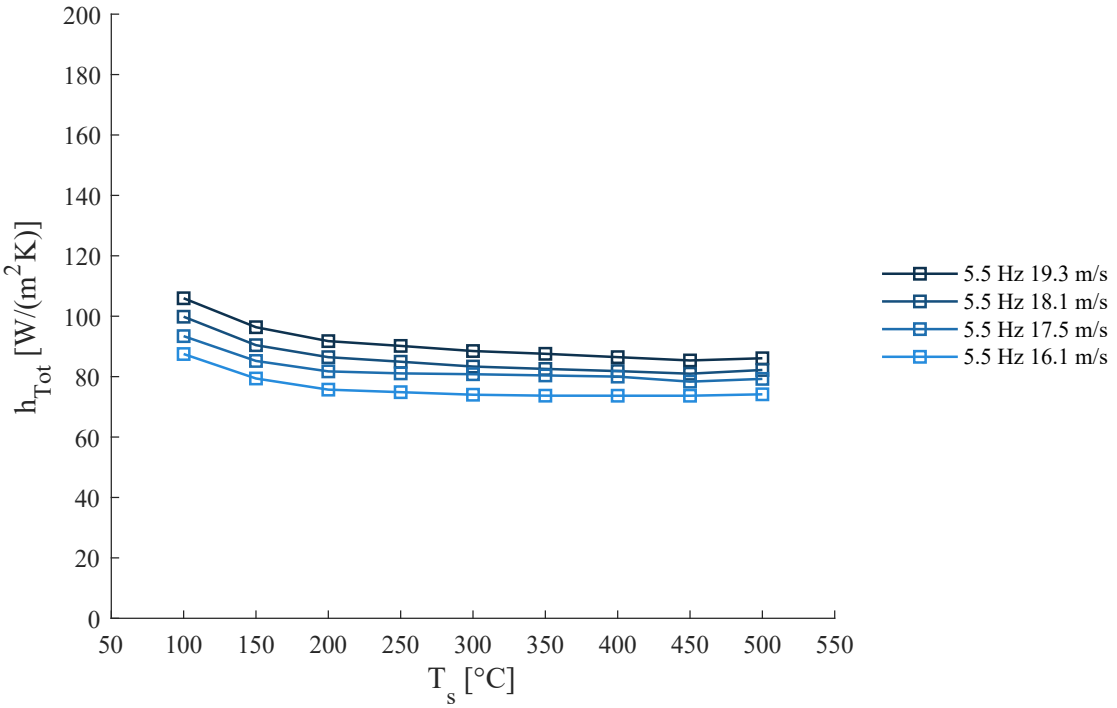

Figure A.1.: Total heat transfer coefficient h_{Tot} at different steel plate temperatures T_s and varying corrected particle velocities $\hat{u}_{ch}$ at $f = 5.5\ Hz$

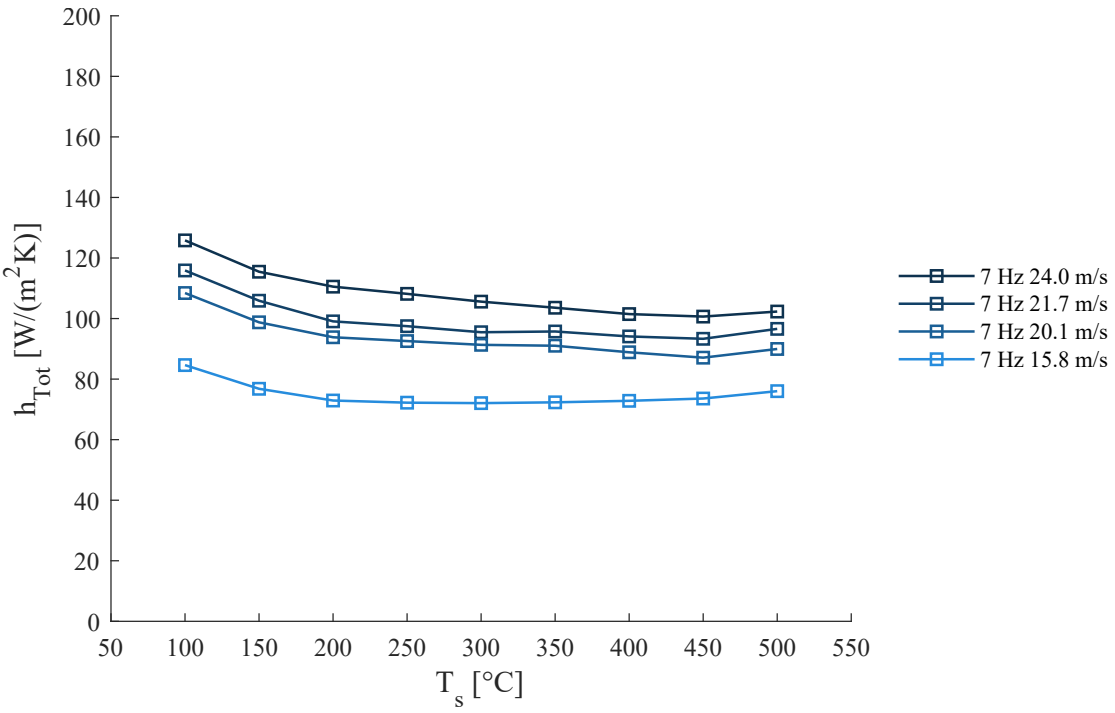

Figure A.2.: Total heat transfer coefficient h_{Tot} at different steel plate temperatures T_s and varying corrected particle velocities $\hat{u}_{ch}$ at $f = 7\ Hz$

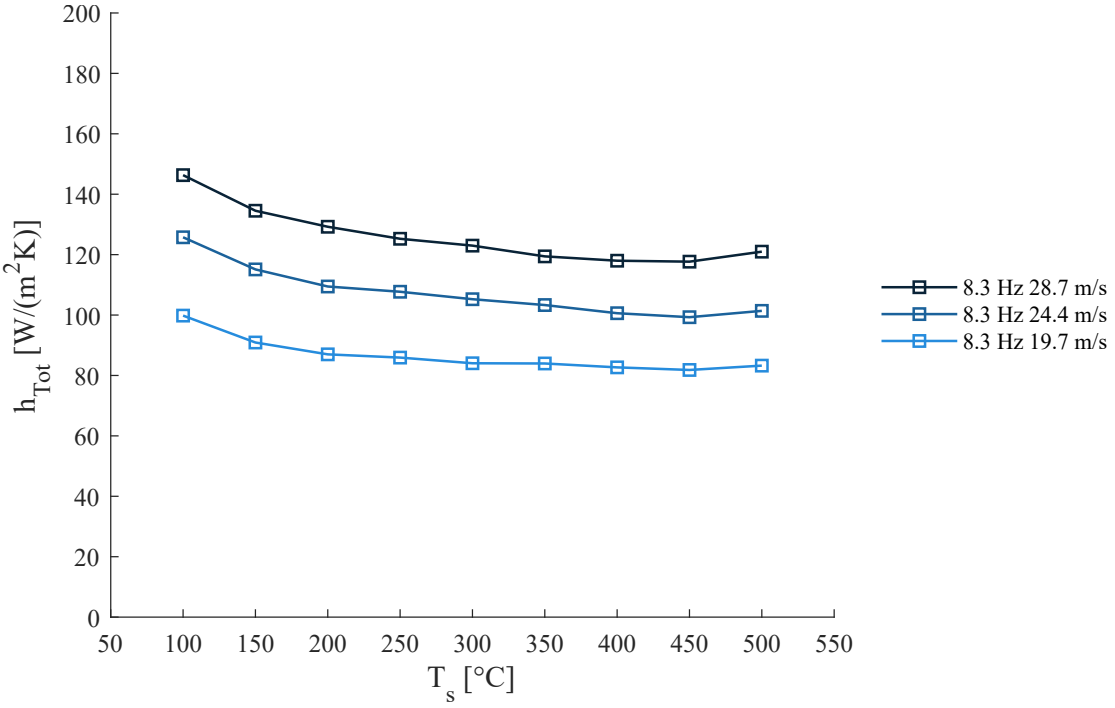

Figure A.3.: Total heat transfer coefficient h_{Tot} at different steel plate temperatures T_s and varying corrected particle velocities $\hat{u}_{ch}$ at $f = 8.3\ Hz$

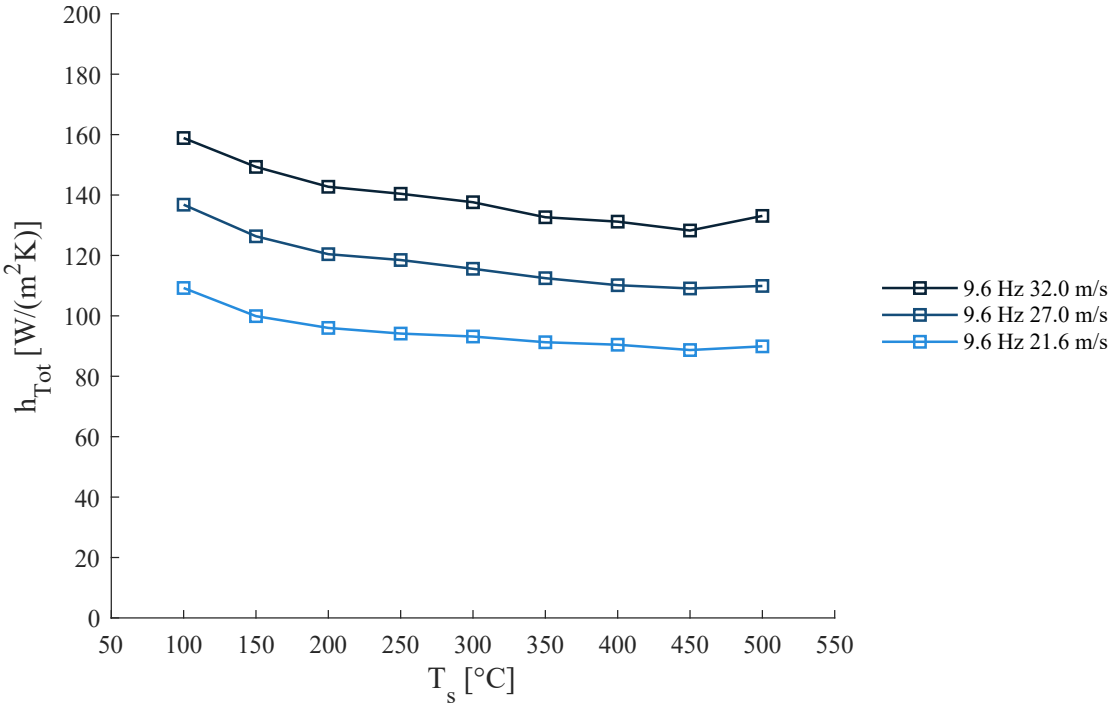

Figure A.4.: Total heat transfer coefficient h_{Tot} at different steel plate temperatures T_s and varying corrected particle velocities $\hat{u}_{ch}$ at $f = 9.6\ Hz$

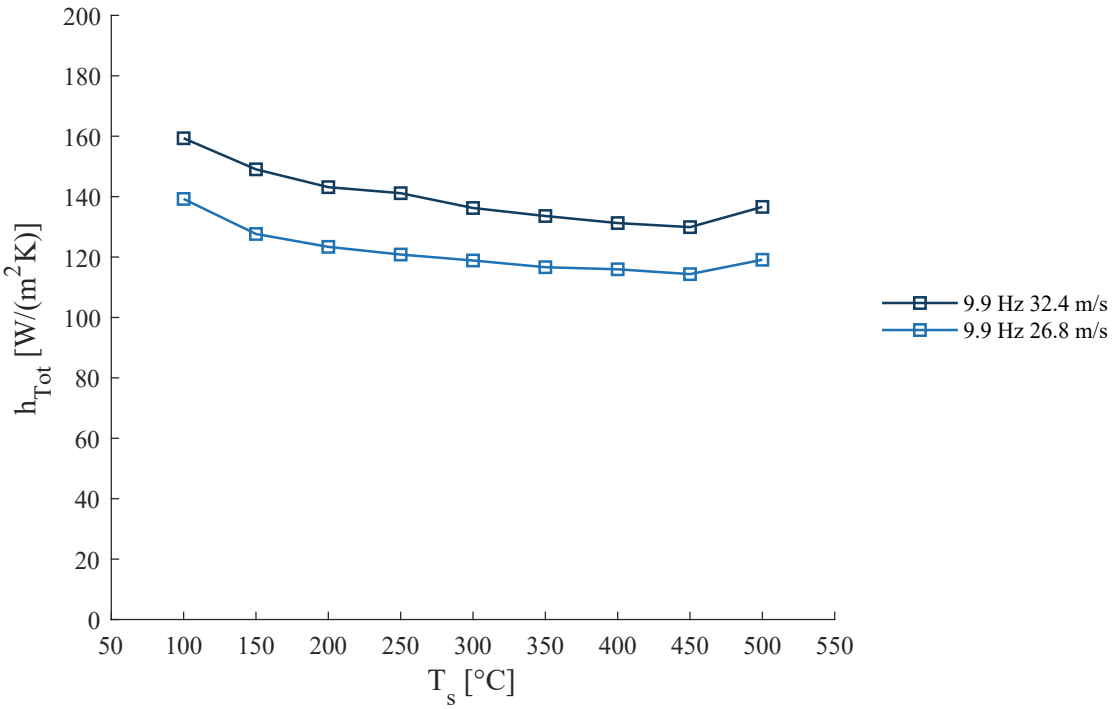

Figure A.5.: Total heat transfer coefficient h_{Tot} at different steel plate temperatures T_s and varying corrected particle velocities $\hat{u}_{ch}$ at $f = 9.9\ Hz$

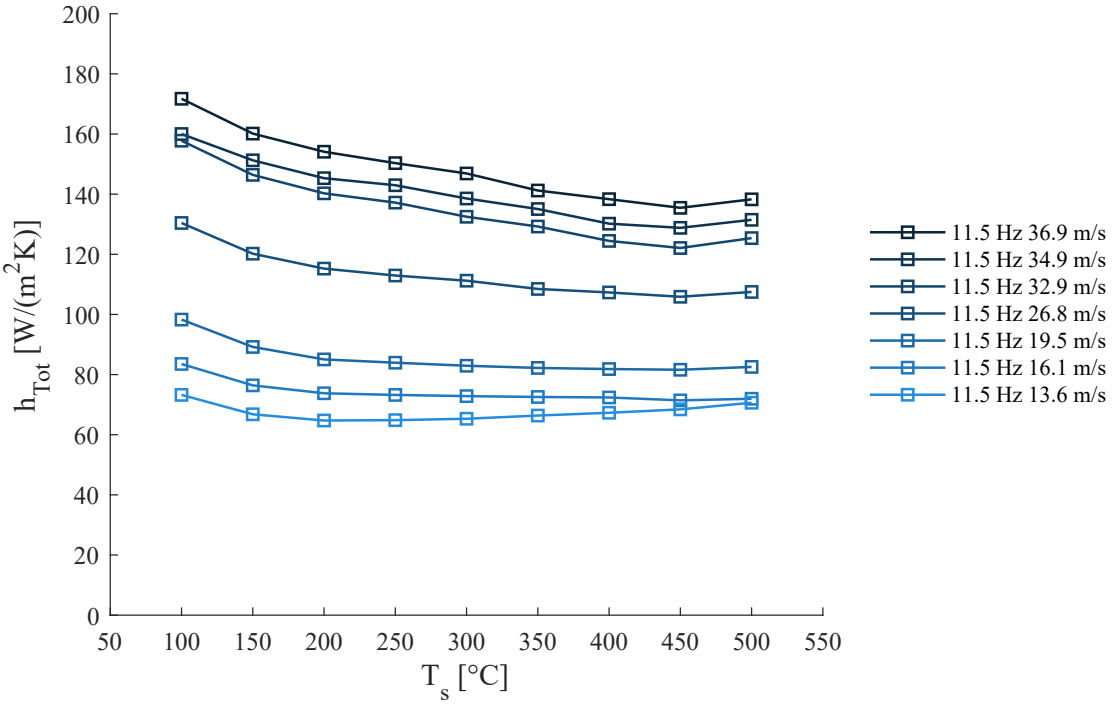

Figure A.6.: Total heat transfer coefficient h_{Tot} at different steel plate temperatures T_s and varying corrected particle velocities $\hat{u}_{ch}$ at $f = 11.5\ Hz$

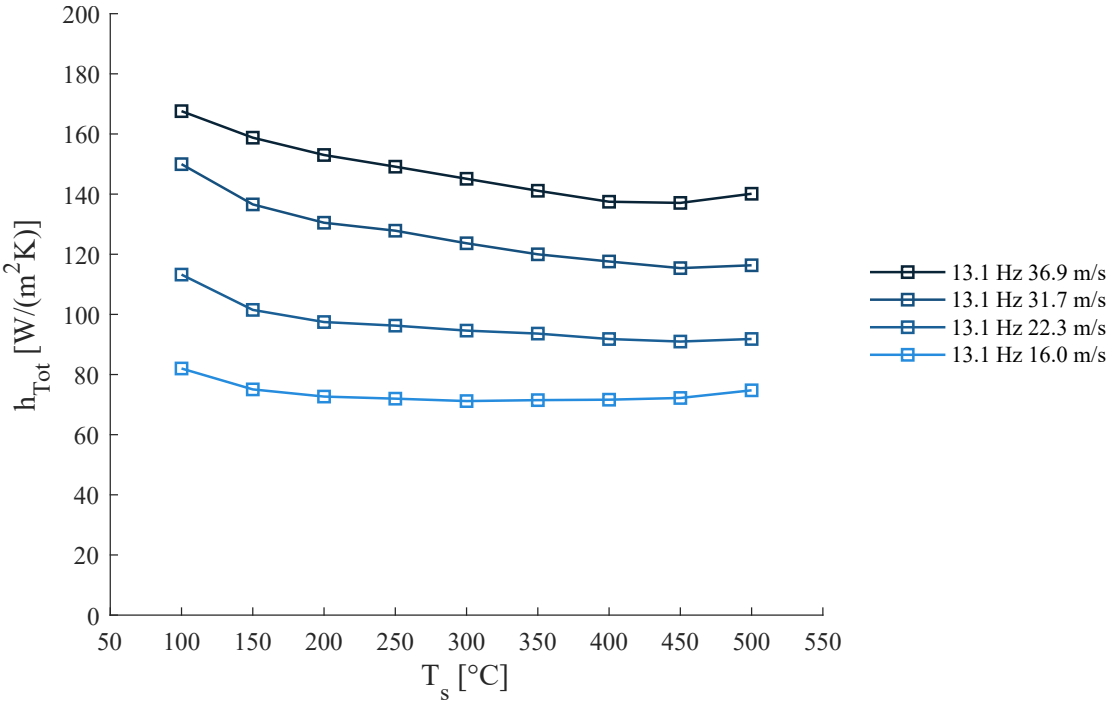

Figure A.7.: Total heat transfer coefficient h_{Tot} at different steel plate temperatures T_s and varying corrected particle velocities $\hat{u}_{ch}$ at $f = 13.1\ Hz$

A.2. h_{Conv} as $g(T_s)$

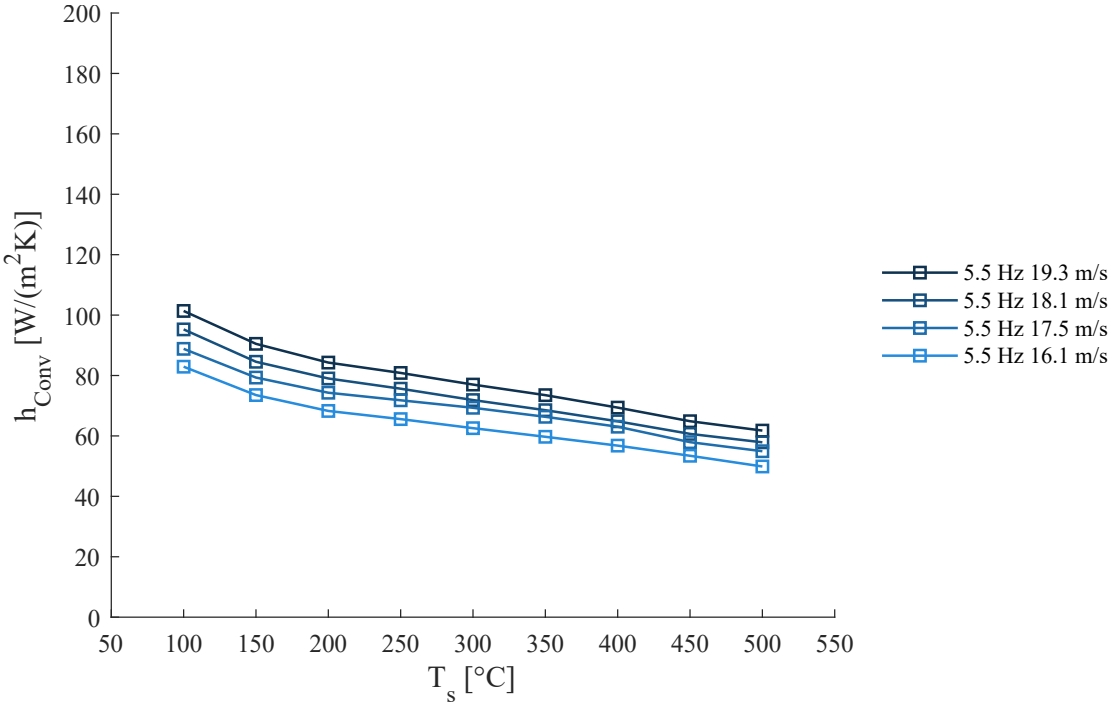

Figure A.8.: Convective heat transfer coefficient h_{Conv} at different steel plate temperatures T_s and varying corrected particle velocities $\hat{u}_{ch}$ at $f = 5.5\ Hz$

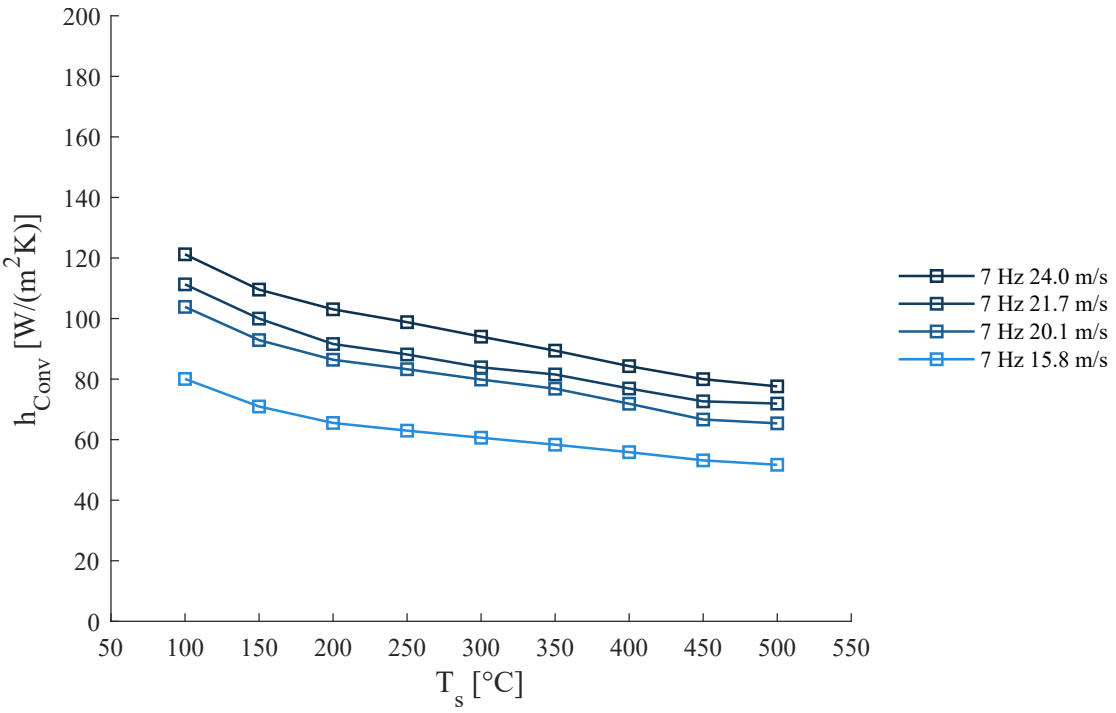

Figure A.9.: Convective heat transfer coefficient h_{Conv} at different steel plate temperatures T_s and varying corrected particle velocities $\hat{u}_{ch}$ at $f = 7\ Hz$

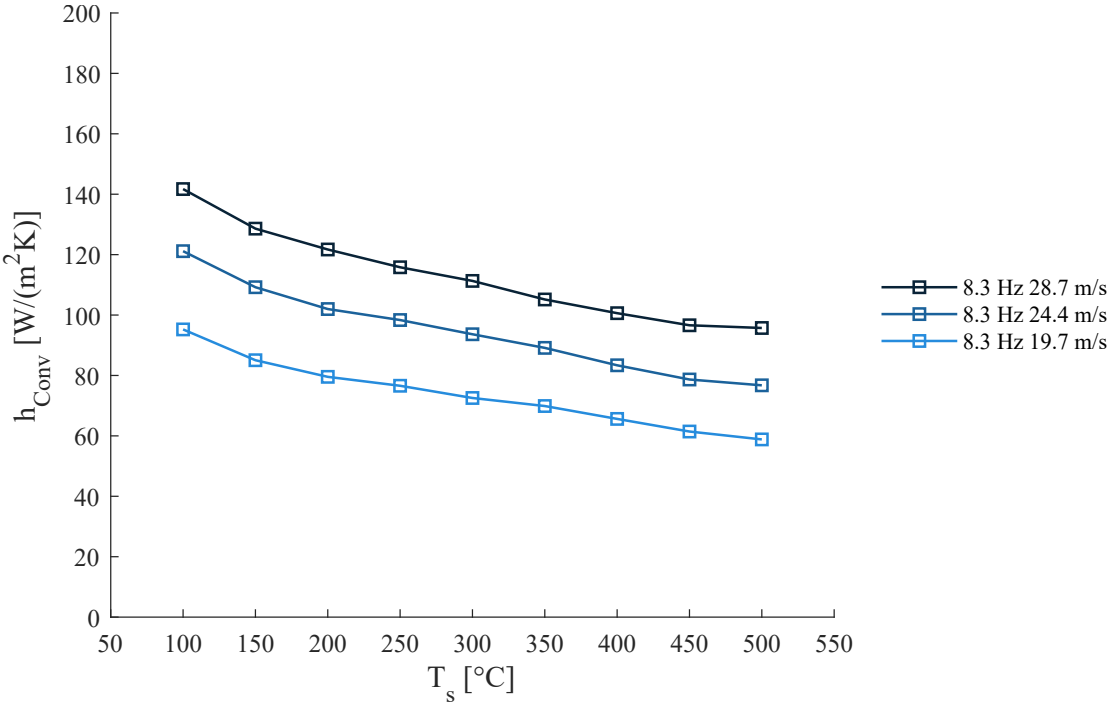

Figure A.10.: Convective heat transfer coefficient h_{Conv} at different steel plate temperatures T_s and varying corrected particle velocities $\hat{u}_{ch}$ at $f = 8.3\ Hz$

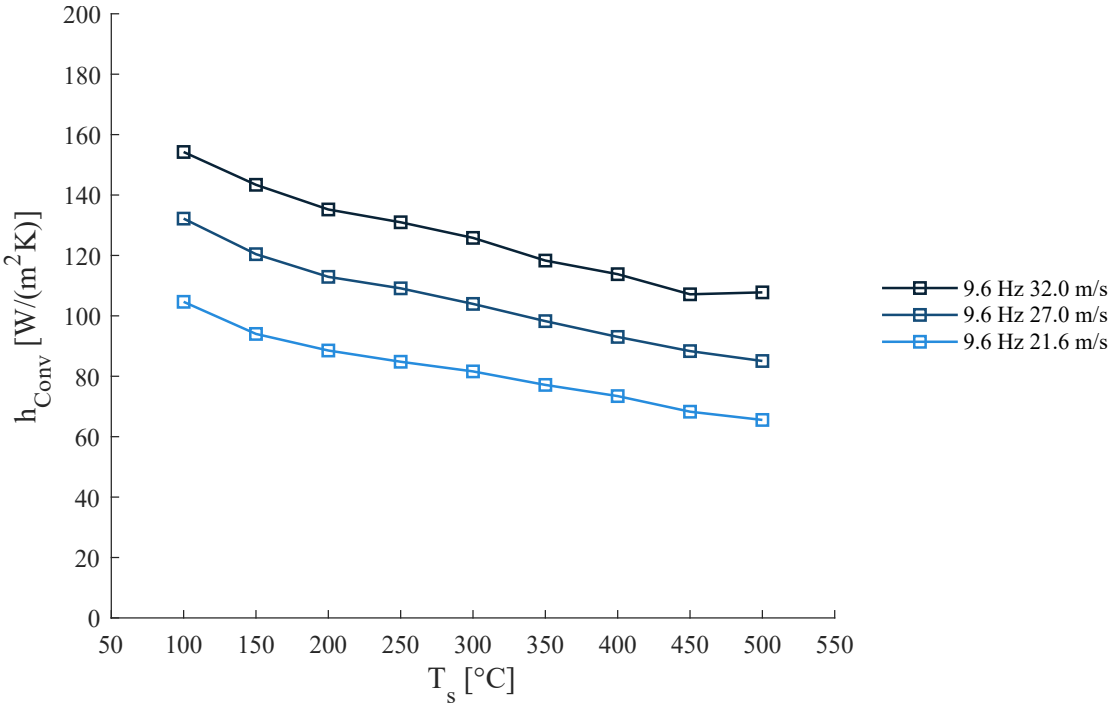

Figure A.11.: Convective heat transfer coefficient h_{Conv} at different steel plate temperatures T_s and varying corrected particle velocities $\hat{u}_{ch}$ at $f = 9.6\,Hz$

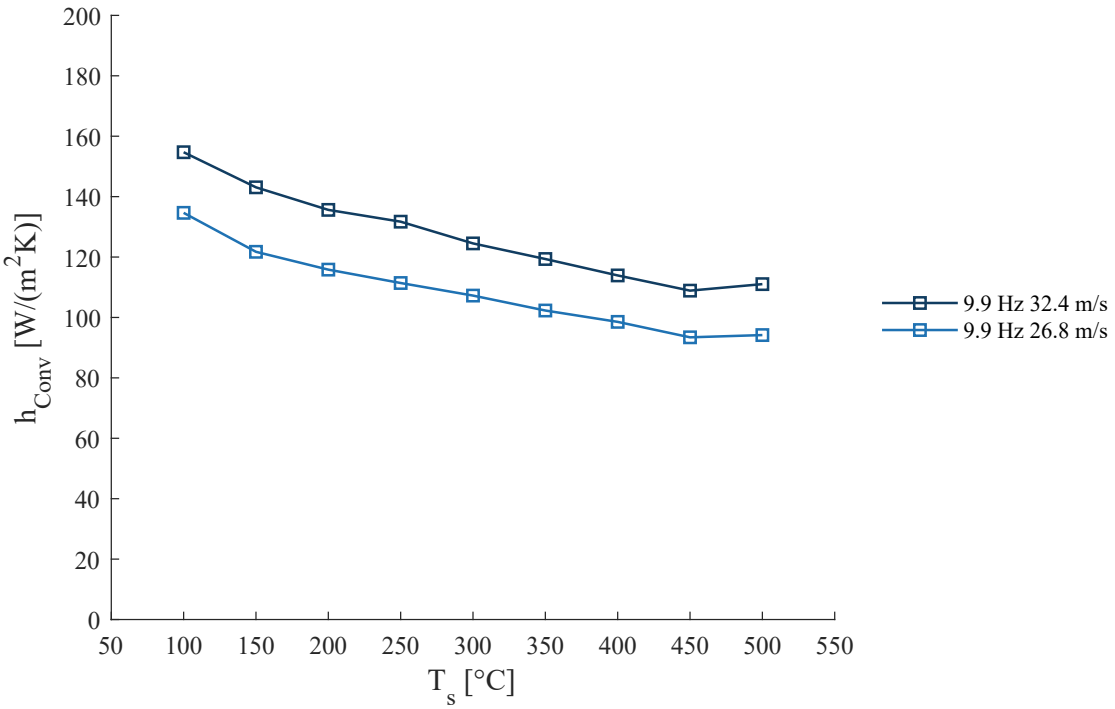

Figure A.12.: Convective heat transfer coefficient h_{Conv} at different steel plate temperatures T_s and varying corrected particle velocities $\hat{u}_{ch}$ at $f = 9.9\,Hz$

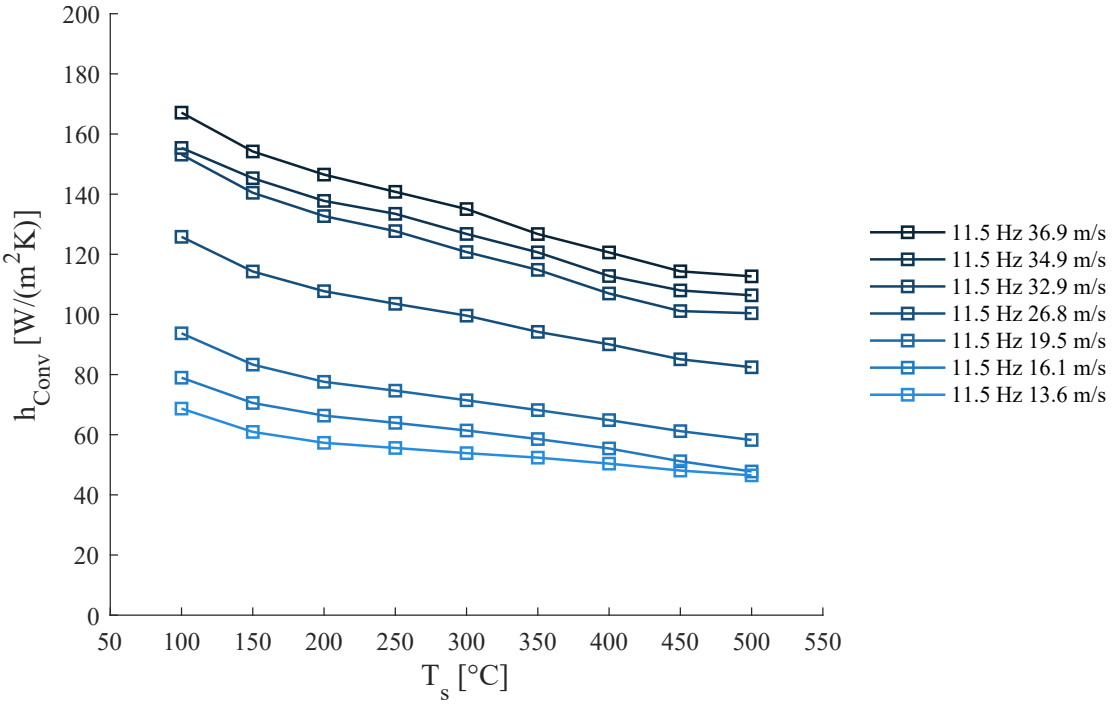

Figure A.13.: Convective heat transfer coefficient h_{Conv} at different steel plate temperatures T_s and varying corrected particle velocities $\hat{u}_{ch}$ at $f = 11.5\ Hz$

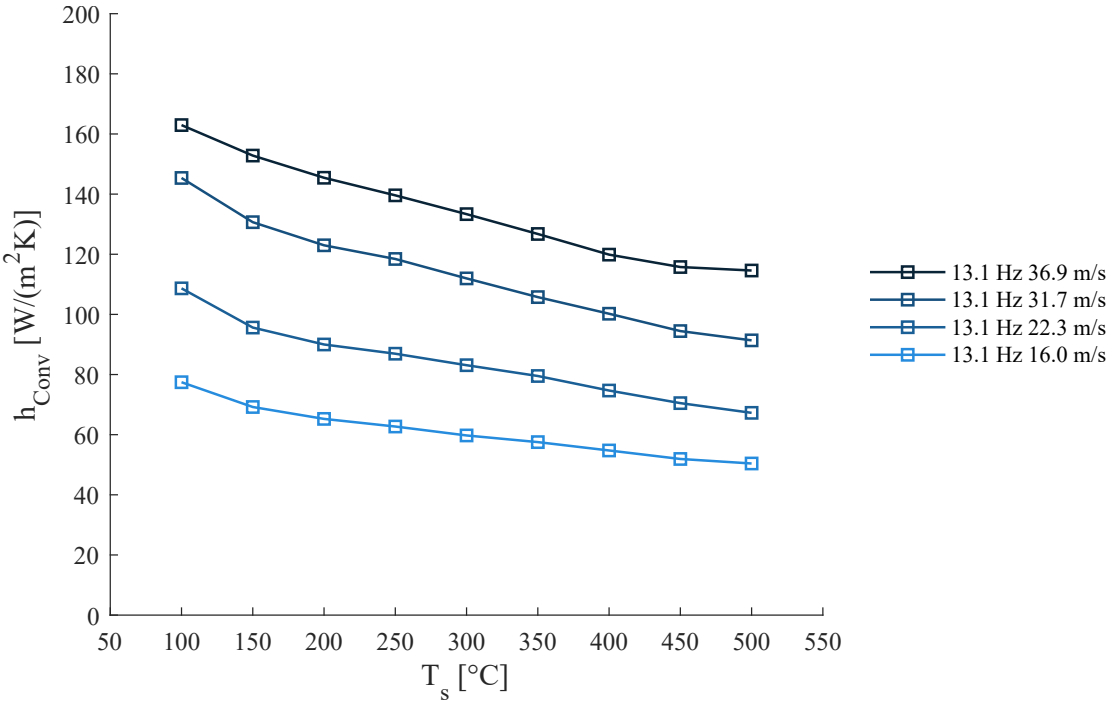

Figure A.14.: Convective heat transfer coefficient h_{Conv} at different steel plate temperatures T_s and varying corrected particle velocities $\hat{u}_{ch}$ at $f = 13.1\ Hz$

A.3. $h_{Conv\,C}$ as $g(T_s)$

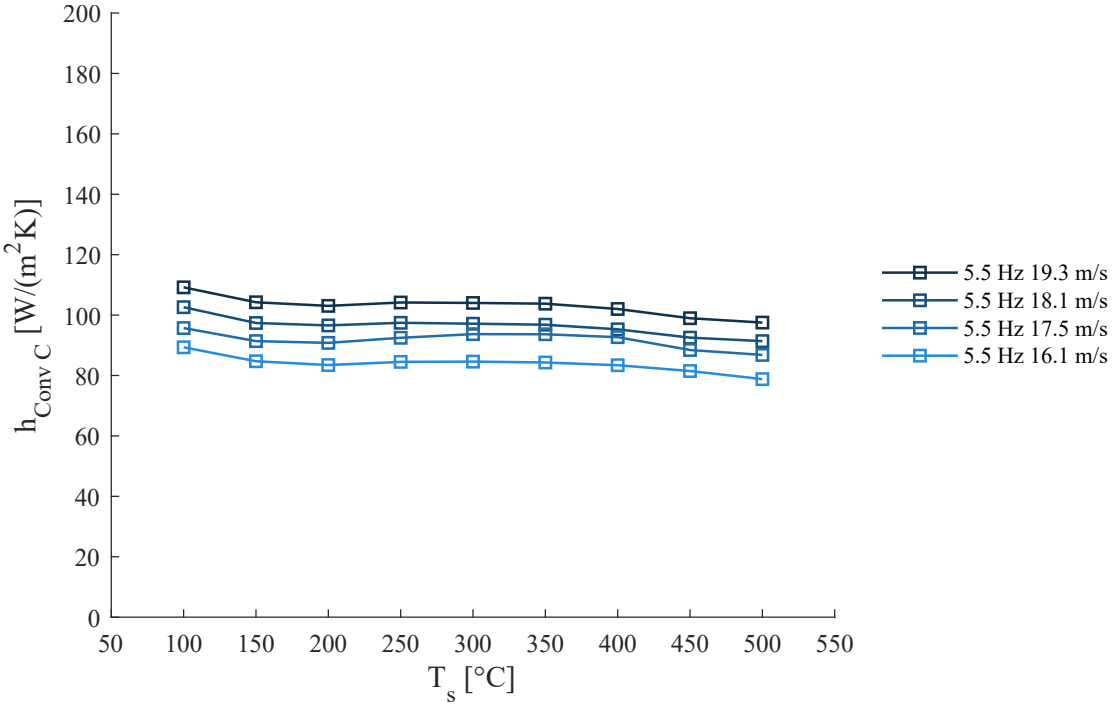

Figure A.15.: Corrected convective heat transfer coefficient $h_{Corr\,Conv}$ at different steel plate temperatures T_s and varying corrected particle velocities $\hat{u}_{ch}$ at $f = 5.5\ Hz$

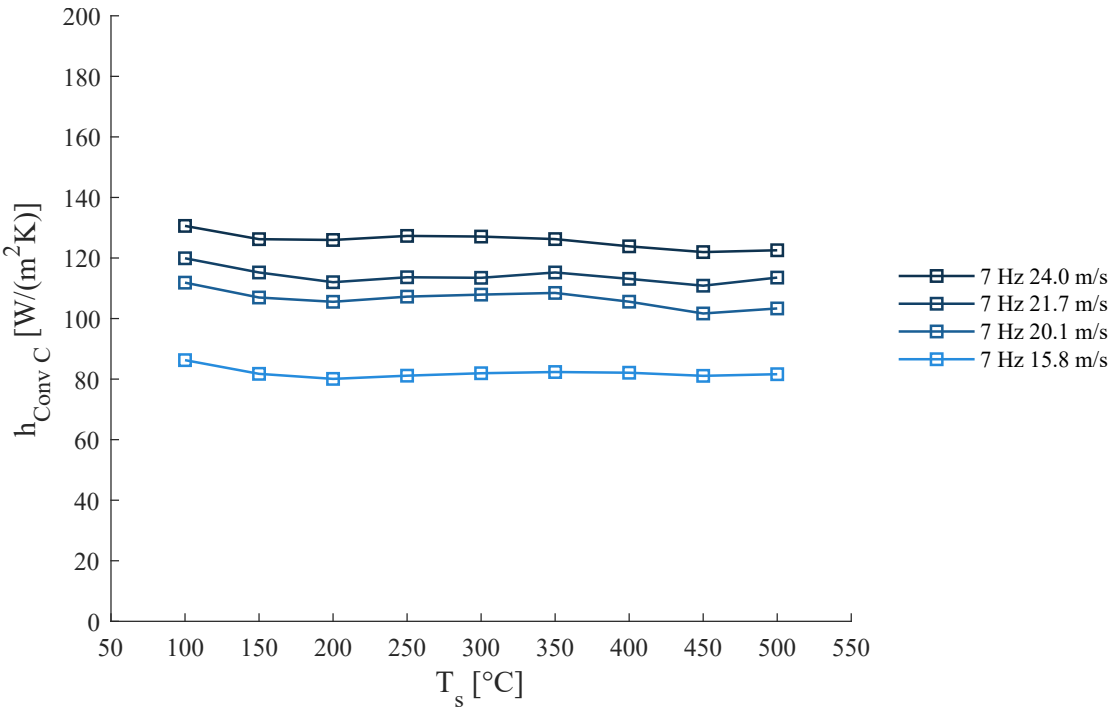

Figure A.16.: Corrected convective heat transfer coefficient $h_{Corr\ Conv}$ at different steel plate temperatures T_s and varying corrected particle velocities $\hat{u}_{ch}$ at $f = 7\ Hz$

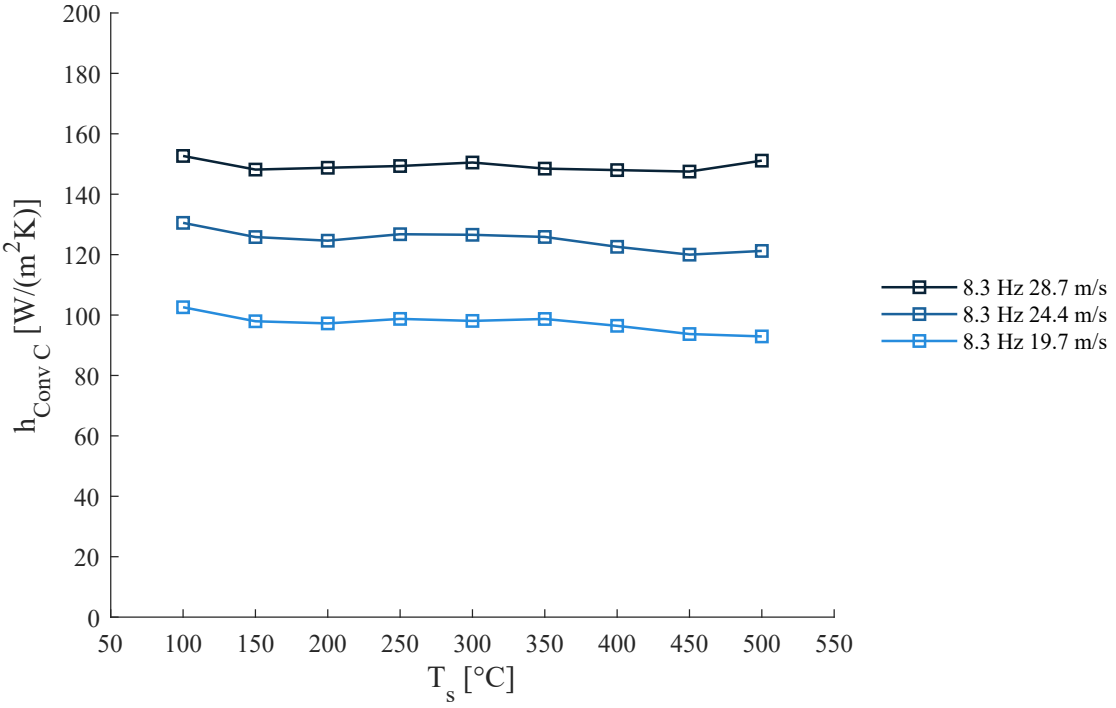

Figure A.17.: Corrected convective heat transfer coefficient $h_{Corr\ Conv}$ at different steel plate temperatures T_s and varying corrected particle velocities $\hat{u}_{ch}$ at $f = 8.3\ Hz$

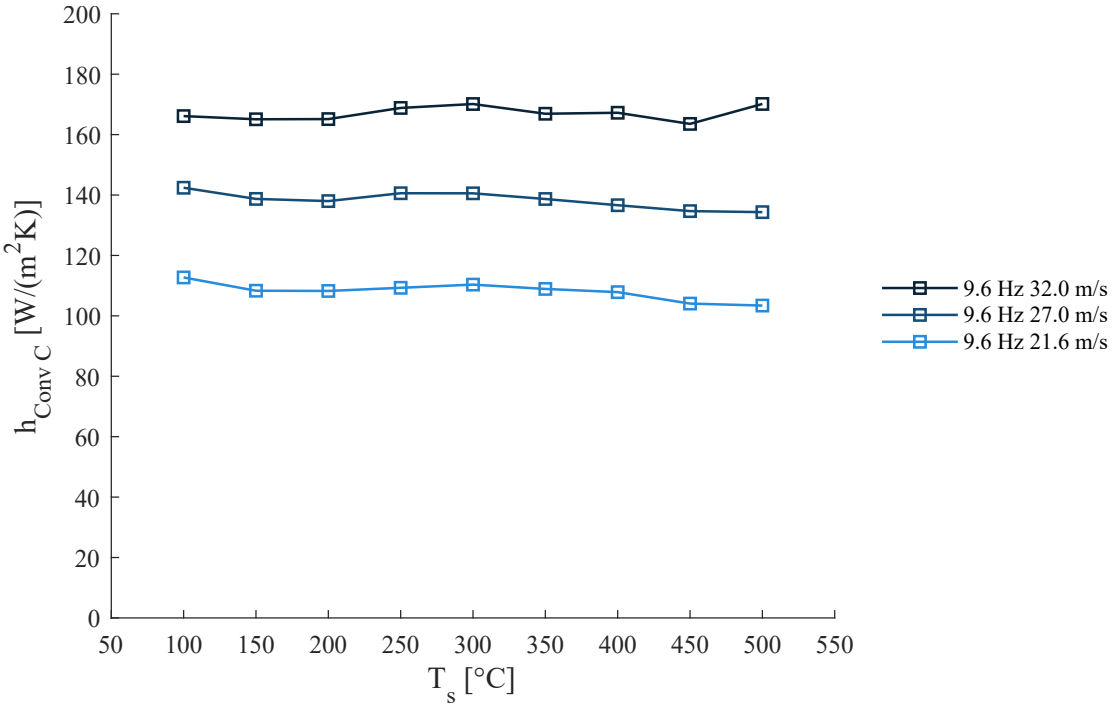

Figure A.18.: Corrected convective heat transfer coefficient $h_{Corr\,Conv}$ at different steel plate temperatures T_s and varying corrected particle velocities $\hat{u}_{ch}$ at $f = 9.6\,Hz$

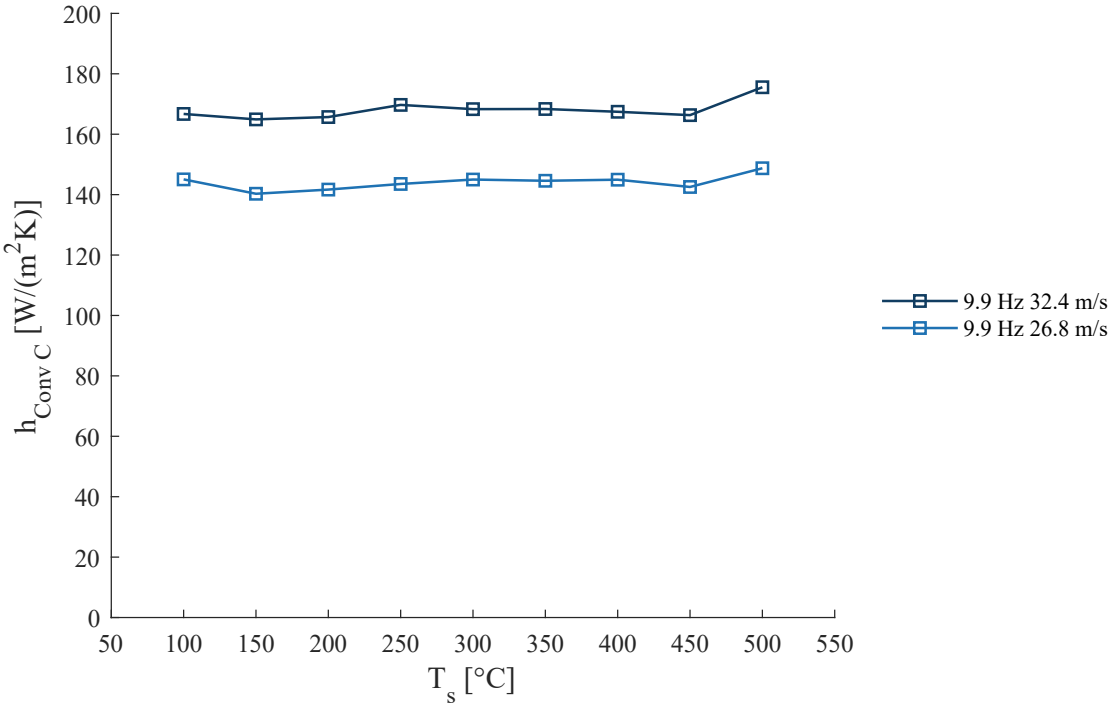

Figure A.19.: Corrected convective heat transfer coefficient $h_{Corr\,Conv}$ at different steel plate temperatures T_s and varying corrected particle velocities $\hat{u}_{ch}$ at $f = 9.9\,Hz$

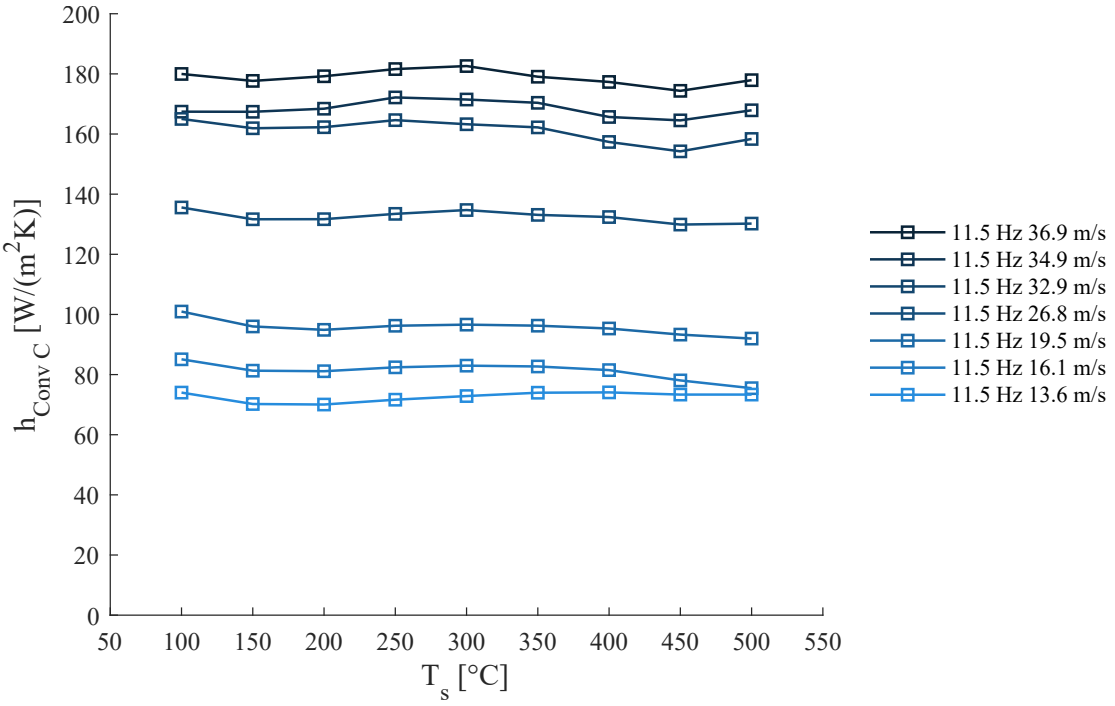

Figure A.20.: Corrected convective heat transfer coefficient $h_{Corr\ Conv}$ at different steel plate temperatures T_s and varying corrected particle velocities $\hat{u}_{ch}$ at $f = 11.5\ Hz$

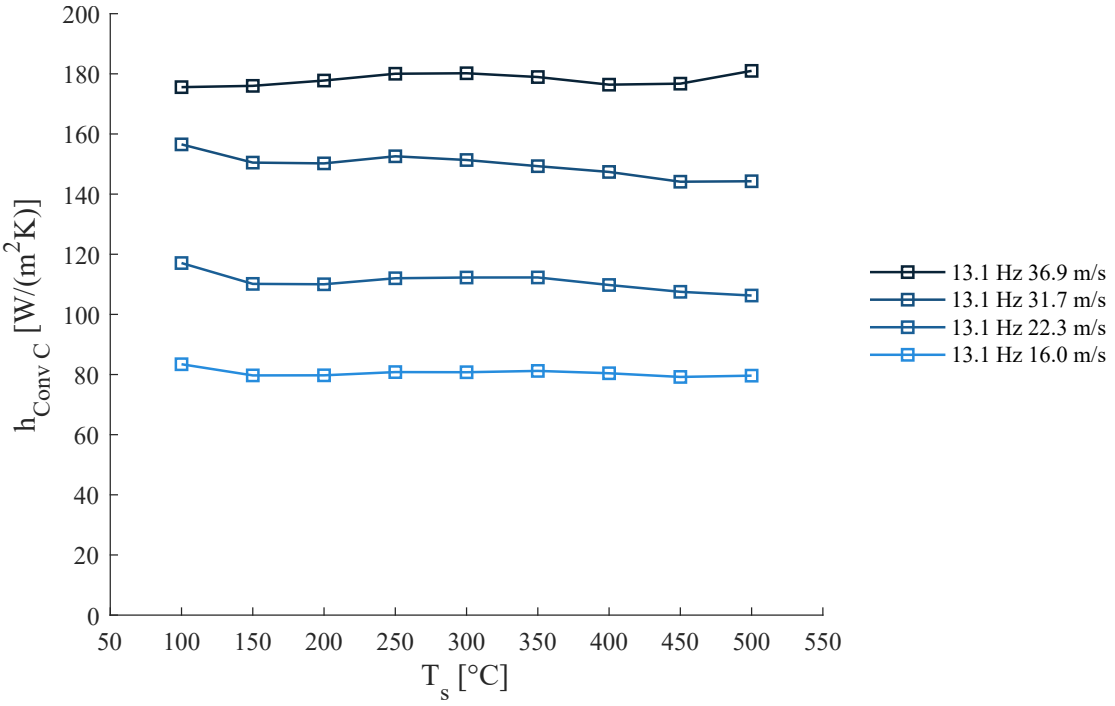

Figure A.21.: Corrected convective heat transfer coefficient $h_{Corr\ Conv}$ at different steel plate temperatures T_s and varying corrected particle velocities $\hat{u}_{ch}$ at $f = 13.1\ Hz$

Appendix B.

Full size images of h as a function of $\hat{u}_{ch}$ and f

B.1. h as $g(\hat{u}_{ch})$

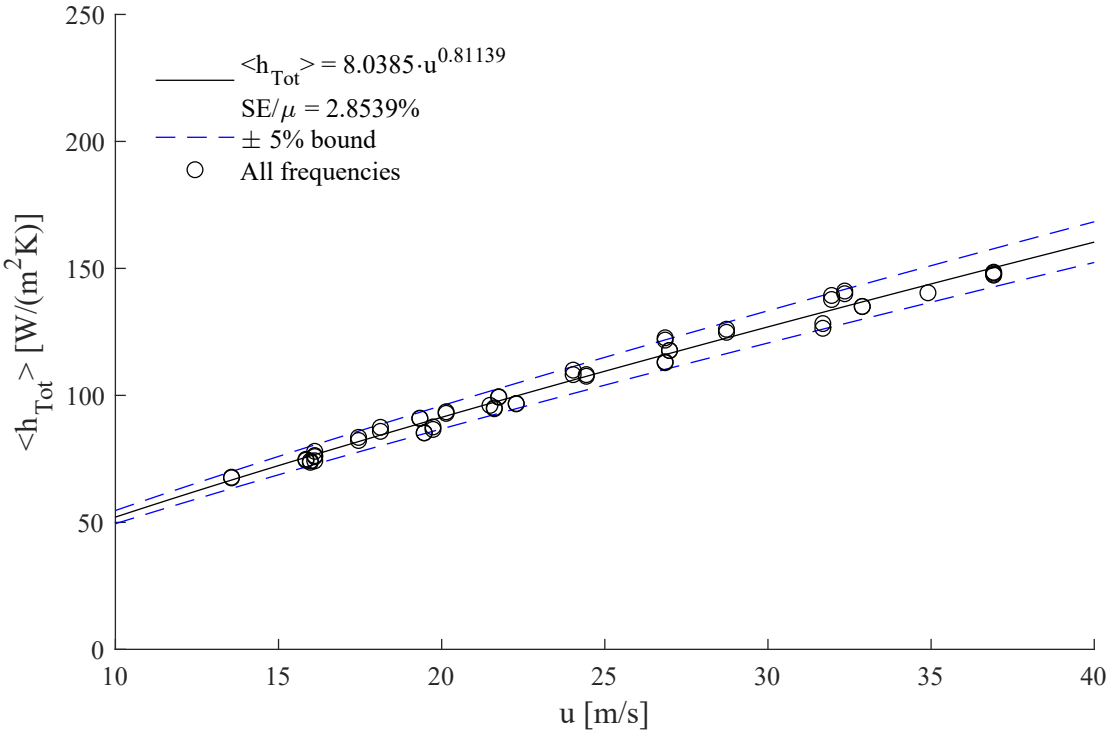

Figure B.1.: Mean total heat transfer coefficient as a function of corrected particle velocity

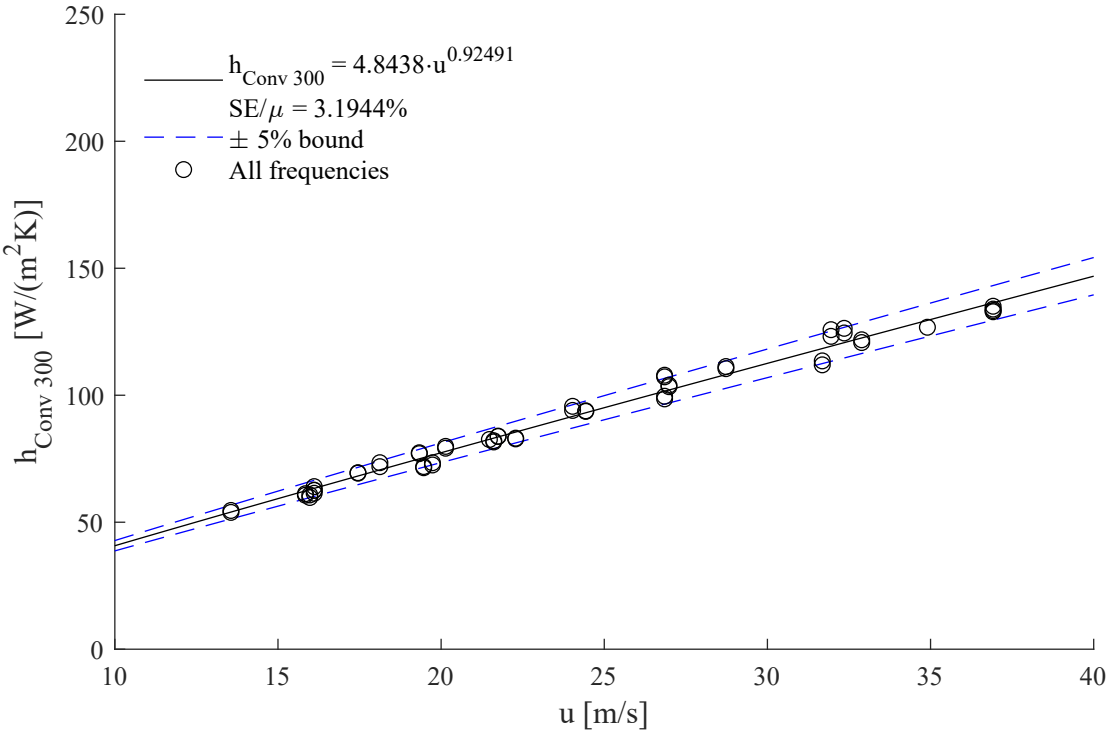

Figure B.2.: Convective heat transfer coefficient as a function of corrected particle velocity at 300 °*C*

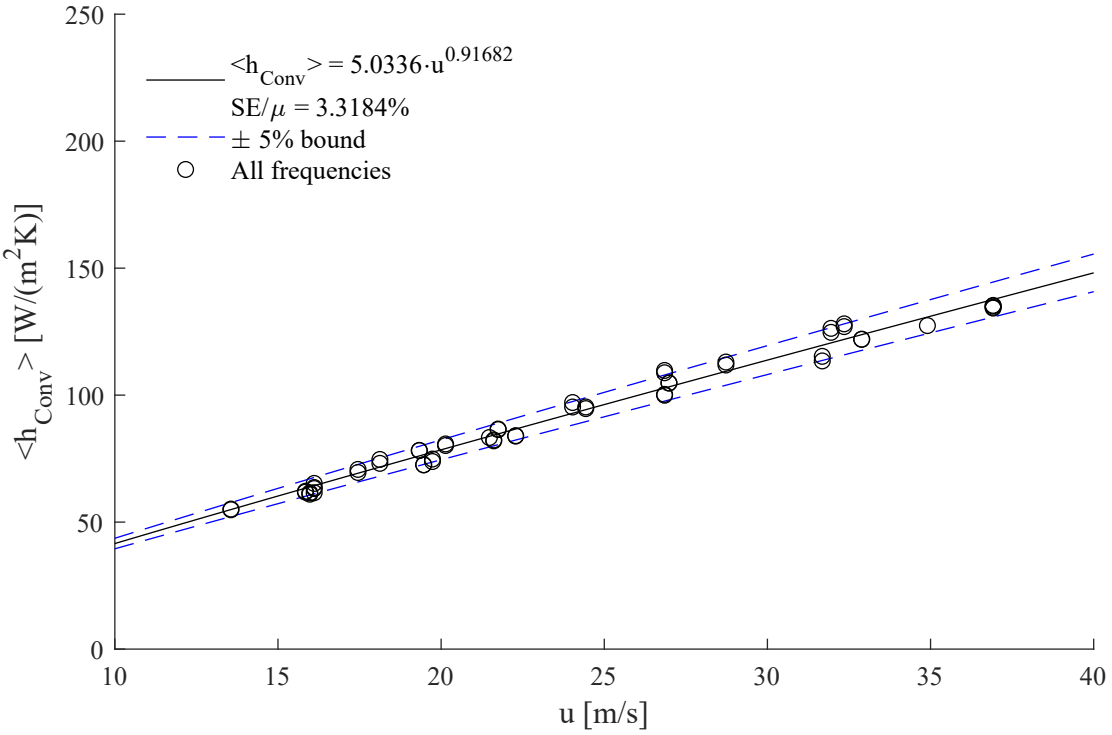

Figure B.3.: Mean convective heat transfer coefficient as a function of corrected particle velocity

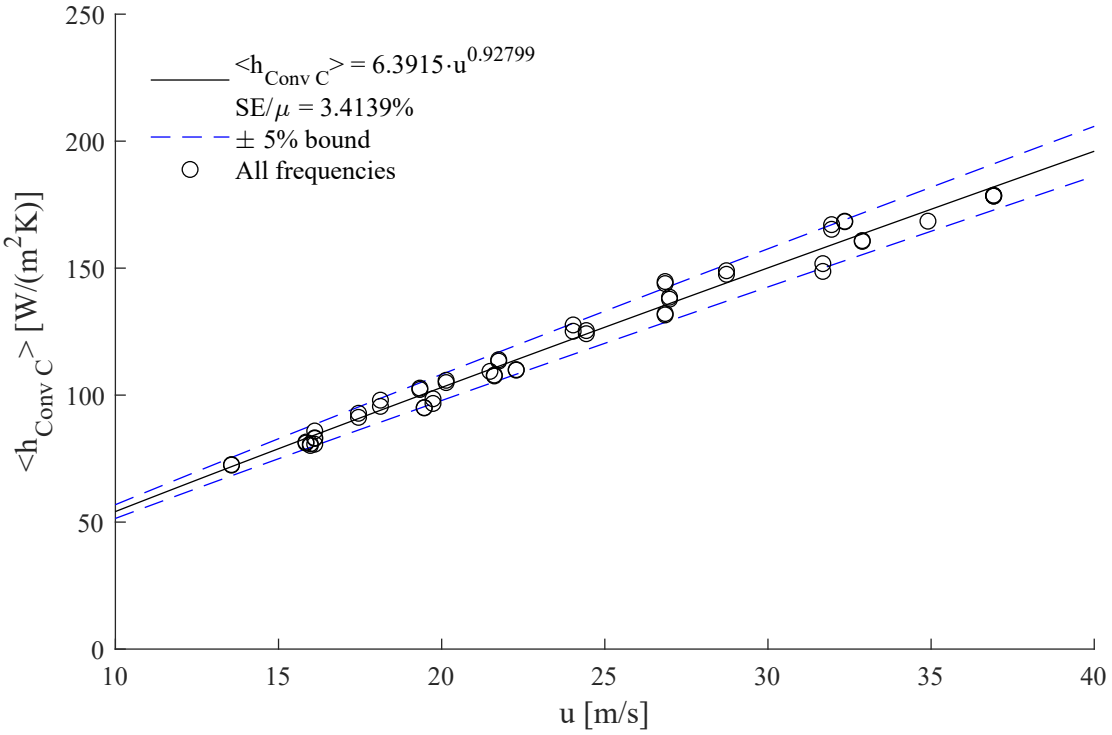

Figure B.4.: Mean corrected convective heat transfer coefficient as a function of corrected particle velocity

B.2. h as $g(f)$

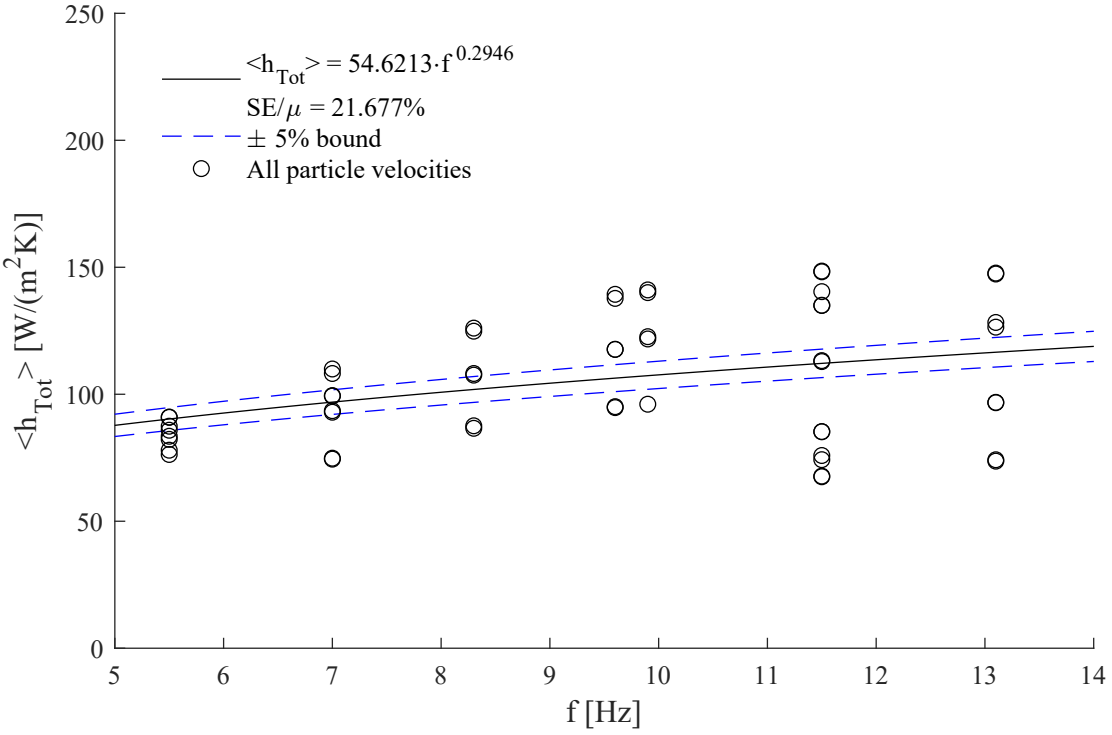

Figure B.5.: Mean total heat transfer coefficient as function of frequency

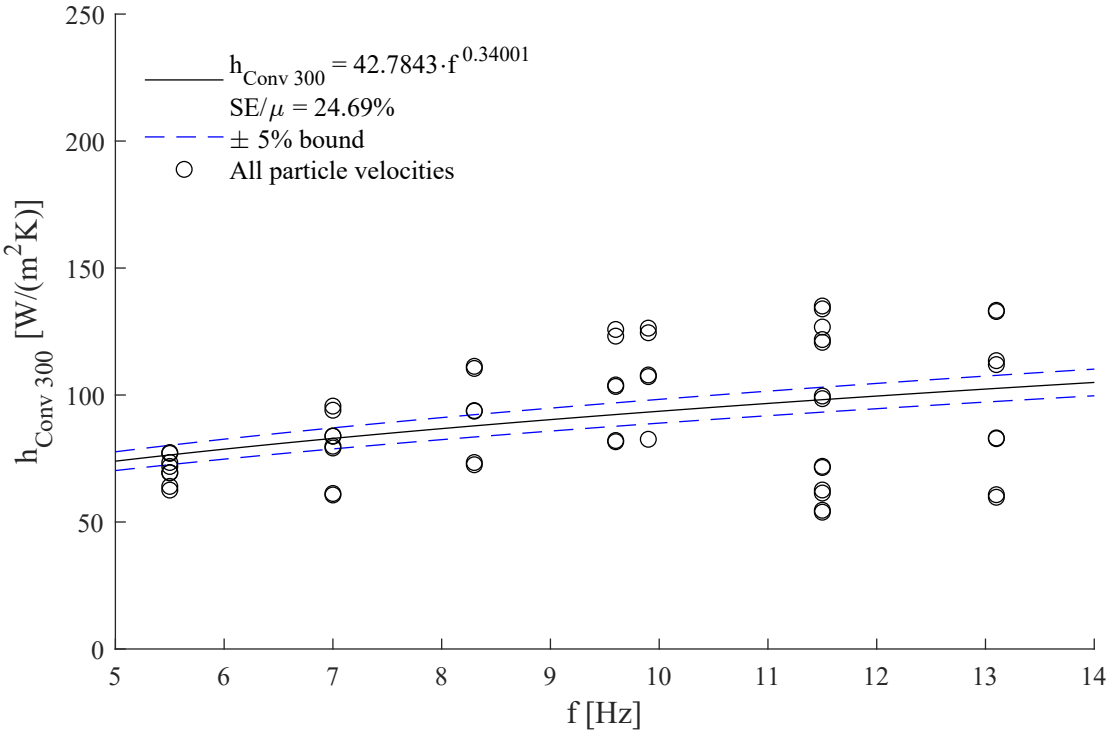

Figure B.6.: Convective heat transfer coefficient as function of frequency at 300 °*C*

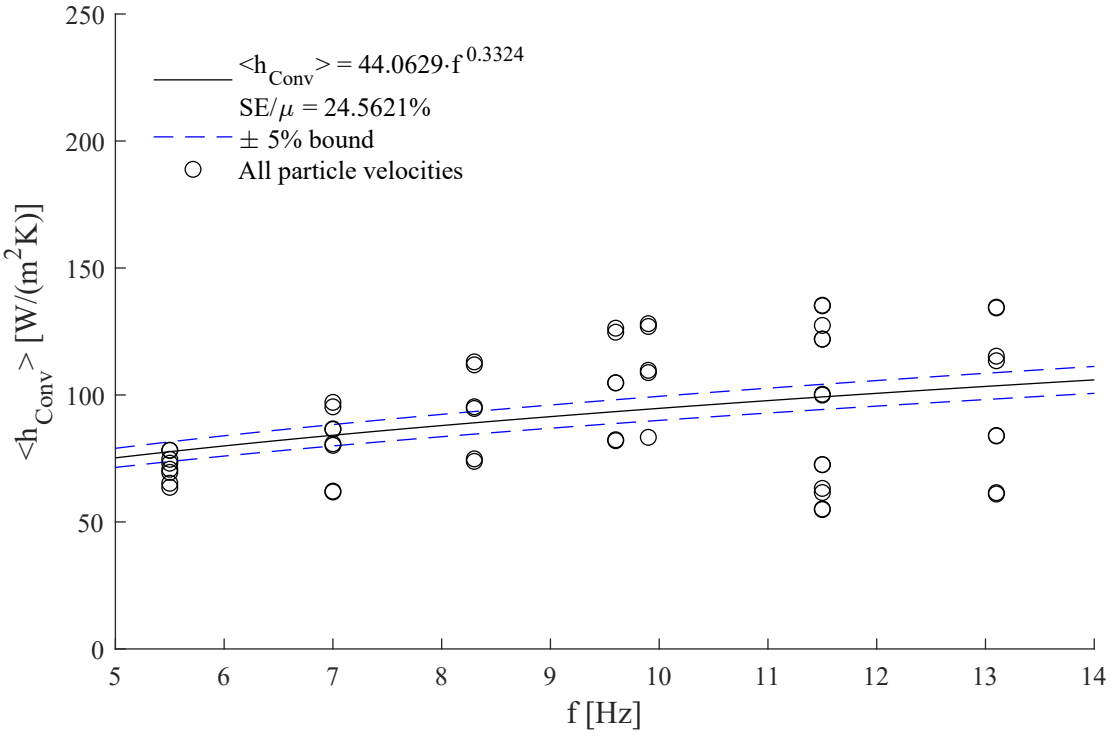

Figure B.7.: Mean convective heat transfer coefficient as function of frequency

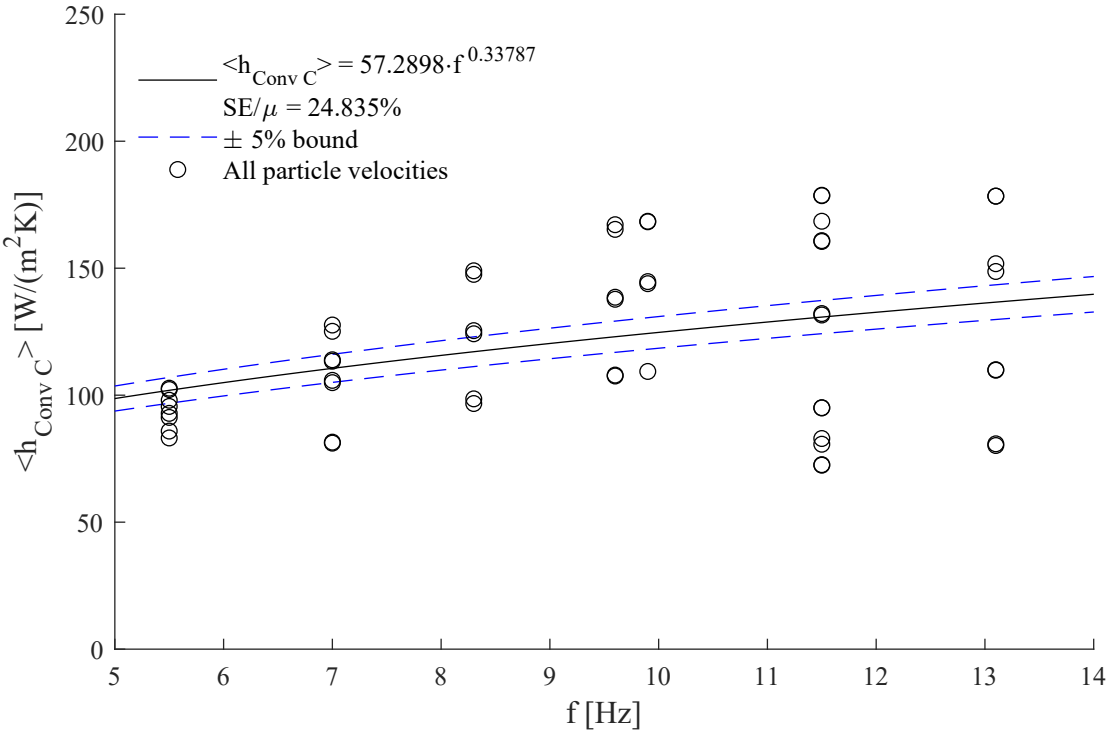

Figure B.8.: Mean corrected convective heat transfer coefficient as function of frequency

B.3. h as $g(\hat{u}_{ch},\ f)$

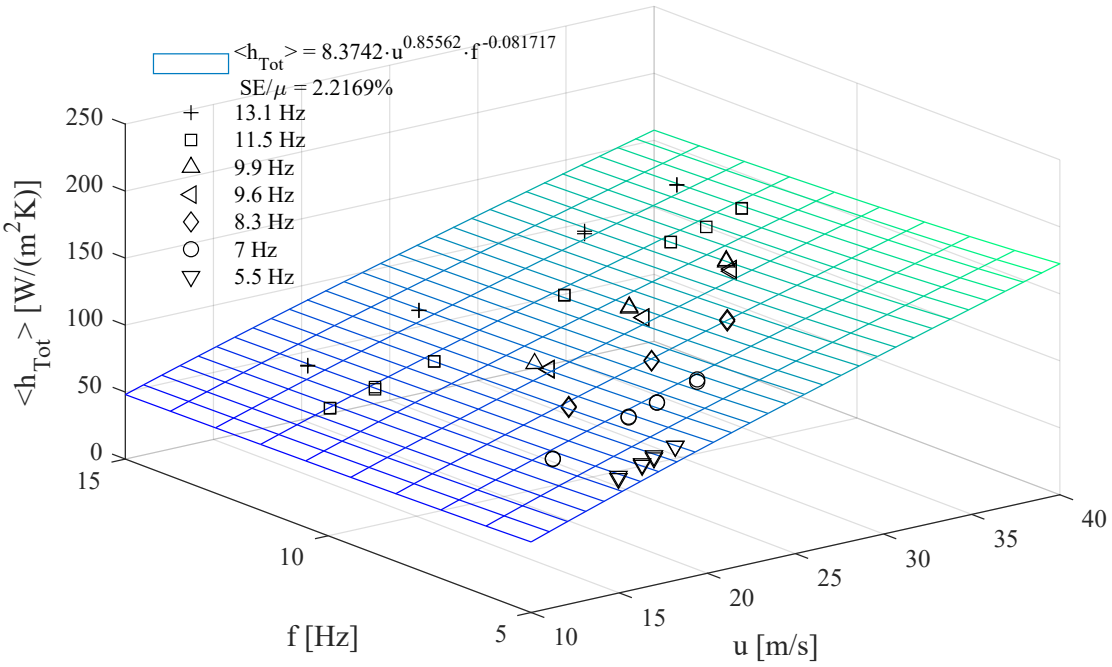

Figure B.9.: Mean total heat transfer coefficient as a function of corrected particle velocity and frequency

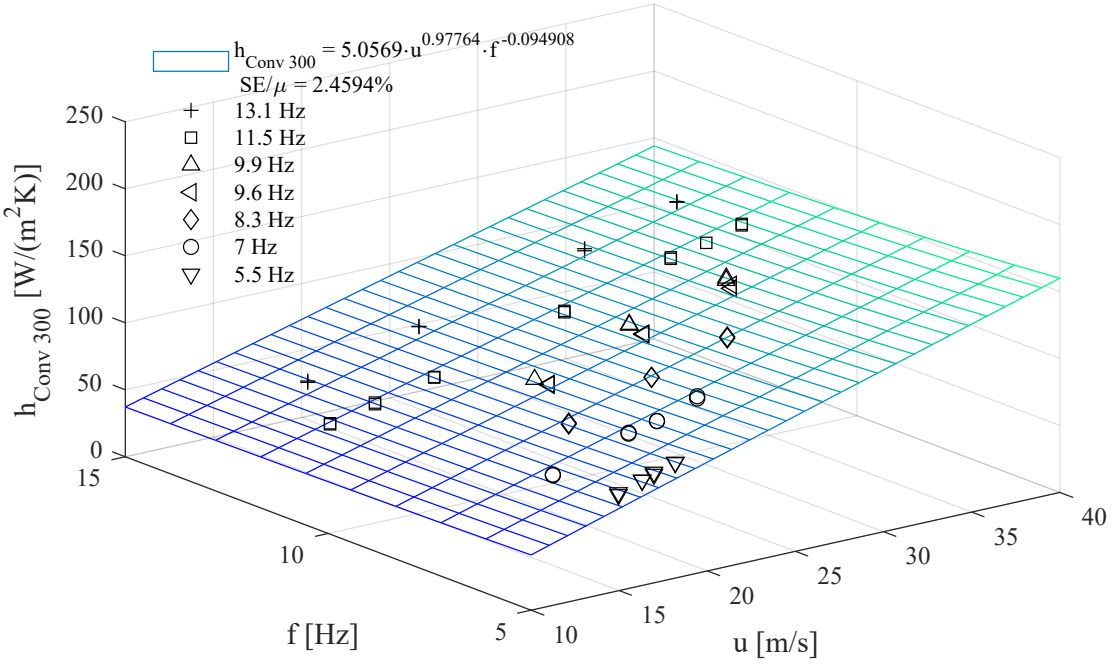

Figure B.10.: Convective heat transfer coefficient as a function of corrected particle velocity and frequency at 300 °C

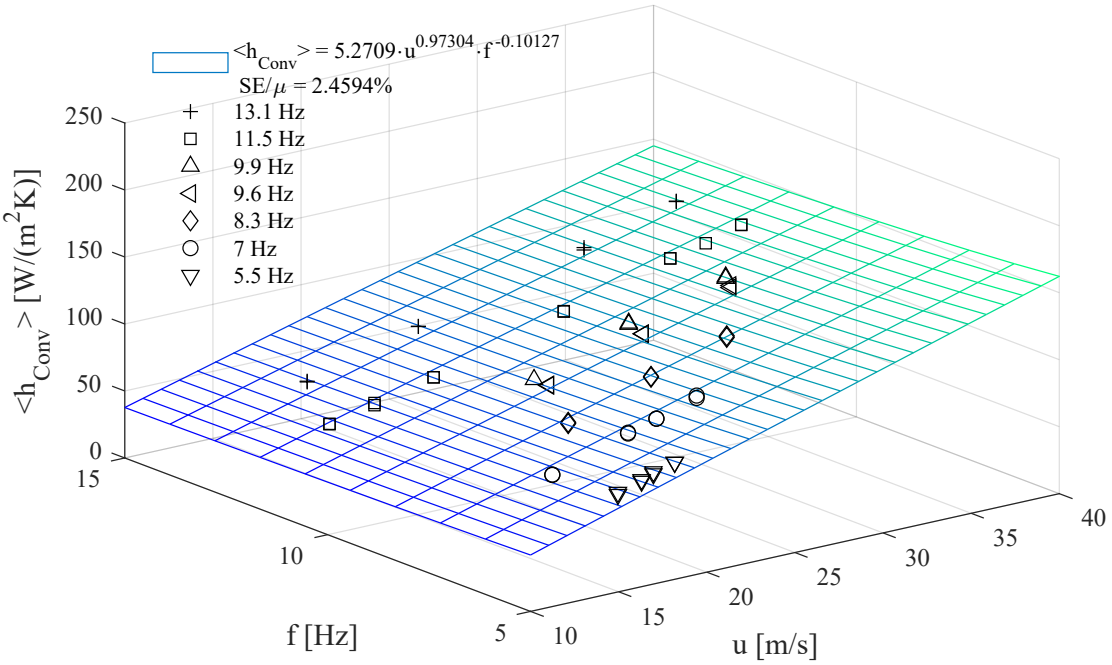

Figure B.11.: Mean convective heat transfer coefficient as a function of corrected particle velocity and frequency

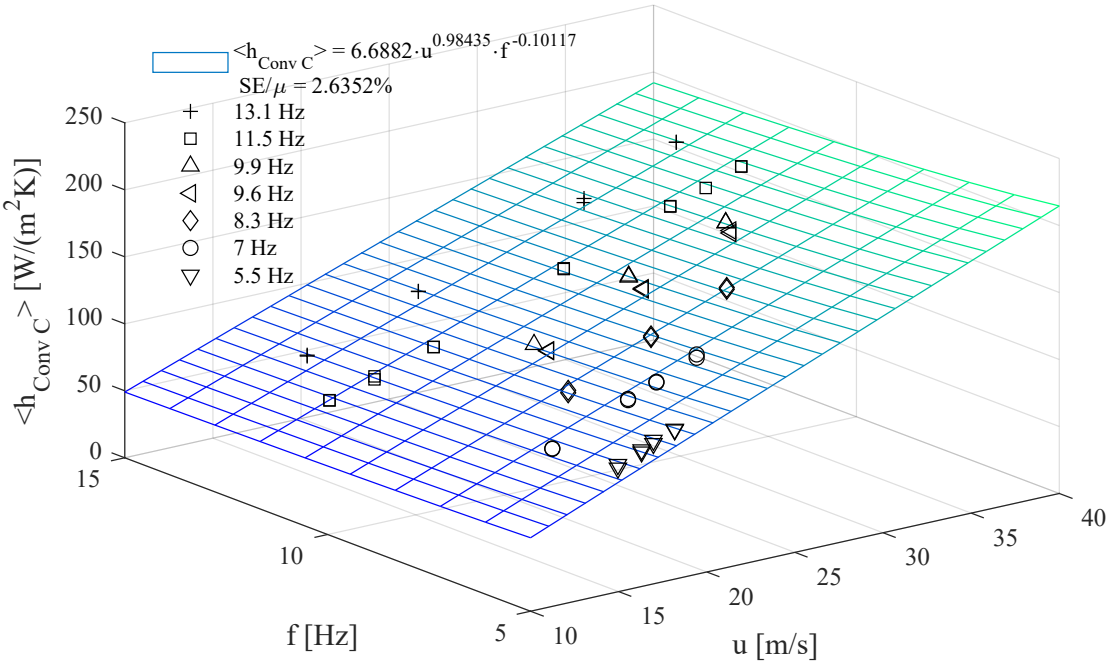

Figure B.12.: Mean corrected convective heat transfer coefficient as a function of corrected particle velocity and frequency